University of Alberta

Terahertz Spinplasmonic Devices

by

Corey Allan Baron

A thesis submitted to the Faculty of Graduate Studies and Research
in partial fulfillment of the requirements for the degree of

Master of Science

Department of Electrical and Computer Engineering

Fall 2009
Edmonton, Alberta

Examining Committee

Abdulhakem Elezzabi, Electrical and Computer Engineering

Vien Van, Electrical and Computer Engineering

Jan Jung, Physics

Dedication

To June, my inspiration.

Abstract

This thesis focuses on the study of the electromagnetic properties of active spinplasmonic artificial materials. Artificial materials are composites having a macroscopic electromagnetic response that arises due to electromagnetic and electronic interactions between subwavelength sized elements. They are of practical engineering interest due to the wide range of free parameters such as the size, shape, density, and orientation of the individual elements, among others, thus providing the means to produce highly customizable photonic components. The thesis work can be categorized into four major sections: the design and construction of an advanced terahertz system capable of probing the electromagnetic response of such materials, the development of a class of artificial materials that permits the active, spin-dependent tuning of the position dependent phase accumulation of terahertz radiation, the study of spintronic-plasmonic artificial materials, and the discovery of a loss reduction mechanism for terahertz pulses transmitted through dense ensembles of bimetallic particles.

Acknowledgments

I extend my heartfelt thanks to my supervisor, Dr. Abdulhakem Elezzabi, who over the last few years has provided me with the guidance and support that has helped me to grow as a researcher. His helpful suggestions and enthusiasm for physics has provided me with motivation and encouragement that helped to make this thesis possible.

I would like to thank Mehmet Egilmez for his expertise and for the fabrication of the samples tested in Chapter 4 and Chapter 5. Without his valuable input the work presented in Chapter 4 and Chapter 5 would not have been possible. I also extend thanks to Dr. Jung and Dr. Chow for their generosity in allowing the use of their laboratory equipment.

Thank you also to my peers, Michael Quong, Kenneth Chau, Vikram Kohli, Pouya Maraghechi, Cameron Straatsma, and Shawn Sederberg for their help and friendship.

I would like to thank my parents, for all their love and support.

Finally, I would like to thank my wife, June. Without her support and encouragement this thesis would not have been possible.

Table of Contents

List of Tables

List of Figures

List of Abbreviations

AES	auger electron spectroscopy
AMR	anisotropic magnetoresistance
AP	aperture
a.u.	arbitrary units
D	diode
EMA	effective medium approximation
EO	electro-optic
FDTD	finite-difference time-domain
FWHM	full-width-at-half-maximum
GMR	giant magnetoresistance
GUI	graphical user interface
L	lens
M	planar mirror
NLSV	non-local spin valve
OBJ	microscope objective
LP	linear polarizer
PC	photoconductive
PM	parabolic mirror
QWP	quarter wave plate
RF	radio-frequency
RKKY	Ruderman-Kittel-Kasuya-Yosida
SEM	scanning electron microscope
SI	semi-insulating
SNR	signal-to-noise ratio
TDS	time-domain spectroscopy
TE	transverse electric

THz	terahertz
TM	transverse magnetic
WP	wallaston prism
XPS	X-ray photoelectron spectroscopy

Chapter 1

Introduction

1.1 Motivation

An essential task in engineering research is to determine the proper material for an envisioned application. Whether it is the semiconductor material for an electrical engineer, the type of steel for a civil engineer, or the polarizer material for an optical engineer, researchers have a strong reliance on, and are often limited by, the intrinsic properties of materials. While the intrinsic properties are dictated by the atomic and molecular composition, a new branch of research in optics and photonics has focused on manipulating the sub-wavelength structure of materials to engineer their optical properties. The wide range of free parameters for *artificial materials* or metamaterials, such as the composition, shape, size, density, alignment, and arrangement of the engineered structural inclusions, allow for many degrees of freedom for design. In such cases, the optical properties of the artificial material are described by *effective* optical parameters (i.e. permittivity and permeability) that differ from the intrinsic optical parameters of the constituent materials. The study of metamaterials is an example of artificial material research where the effective permittivity and permeability are engineered by exploiting electronic and magnetic resonances in the constituent structures [1], permitting unique phenomena such as negative refraction [2], cloaking [3], near perfect absorption [4], subwavelength focusing [5], and negative phase and group velocities [6].

The field of plasmonics offers a unique platform for the creation artificial materials. For example, a plasmonic superlens exhibiting sub-wavelength resolution has been realized via the exploitation of the tendency of surface plasmon polaritons (SPPs) to perceive a negative index of refraction at visible frequencies [5]. Moreover, it has been proposed that localized plasmon resonances in nanoparticles in conjunction with metamaterials can be utilized to create optical nanocircuits that behave analogously to their electronic counterparts [7].

While literature regarding resonant plasmons at optical frequencies is in abundance [8], non-resonant plasmons at terahertz (THz) frequencies have received considerably less attention. Interestingly, the THz regime is attractive for electromagnetic investigations due to the unique capabilities of THz spectroscopic techniques. Unlike spectroscopy in the visible regime, in THz spectroscopy the time-domain electric field waveforms are directly measured. Moreover, in THz spectroscopy the polarization content of the measured radiation can be determined, and thus, the technique offers complete characterization of the magnitude, phase, and polarization characteristics of the radiation. The pulses typically generated and measured are temporally short ($\sim$ 1 ps) and are of high bandwidth ($\sim$ 1 THz), allowing the investigation of a large range of frequencies using a single measurement. These properties have allowed unique insight into many different phenomena, including the optical response of chiral media [9], carrier dynamics [10, 11], and intermolecular interactions [12], among many others.

Plasmons in the THz regime are more weakly confined compared to plasmons in the visible regime due to the considerably larger permittivities of metals at THz frequencies (a factor of $\sim 10^3$ larger [13, 14]), which reduces the penetration of the radiation into the metal. However, this difference between the two regimes also results in THz plasmons having comparatively low loss, which may be attractive for some applications. For example, it has been shown that THz pulses can be guided long distances by a metallic wire [15]. Also, by periodically perforating metallic films the effective permittivity can be modulated such that resonant terahertz surface plasmon polaritons can be excited (i.e. the so-called "designer plasmon") [16]. In contrast to the periodically engineered structures almost ubiquitously used in the creation of artificial materials, the ability of THz particle plasmons to near-field couple and coherently

transport THz radiation over large distances in random ensembles of particles introduces a new paradigm for controlling the propagation of radiation [17, 18]. Interestingly, this type of plasmonic transport introduces additional degrees of freedom that permit phenomena such as materials exhibiting an atypical effective refractive index that cannot be explained by effective medium theory [19].

While numerous passive plasmonic devices have been introduced, the active control of plasmonic devices has only recently begun to be addressed. In the visible regime, methods implemented to actively modulate the propagation of SPPs include utilizing nanoscale structural transformations [20] and ultrafast excitation of the metal supporting the SPP [21]. In the THz regime, active, spin-enabled modulation of the plasmonic enhanced propagation through metallic particles has been enabled via anisotropic magnetoresistance in ferromagnetic metallic particles [22, 23] and spin accumulation at a ferromagnetic-nonmagnetic interface [24].

This thesis explores active artificial materials in the context of plasmonic enhanced propagation of THz radiation through metallic media, and a THz spectroscopy system has been designed and built for studying such phenomena. Provided in this thesis are: (1) a recipe for creating active artificial materials that operate via photonic anisotropic magnetoresistance; (2) an investigation of the active modulation of THz transmission via giant magnetoresistance; and (3) the introduction of a new form of loss reduction for THz transmission through metallic particles. As such, the goal of this thesis work is to discover new and effective ways to control electromagnetic radiation, which is paramount for the development of light-based information technologies.

1.2 Scope of Thesis

In Chapter 2 a system capable of angular- and time-resolved, polarization sensitive detection of THz radiation with detection angles spanning 360° is presented. In a conventional THz spectroscopy system, the system detects the radiation transmitted along the incident beam axis. The realization of a pump-probe spectroscopy system capable of time- and polarization-resolved detection at arbitrary angles is nontrivial, however, since the sampling probe beam must retain its alignment, polarization, and timing for all detection angles. The performance of the off-axis system is demonstrated experimentally, with the results compared to predictions obtained from finite-difference time-domain simulations.

In Chapter 3 a class of active artificial materials composed of a random combination of dielectric and metallic microparticles is discussed. Both an active lens and active router are theoretically explored. In the former case the application of an external magnetic field results in a tunable focal length, while in the latter case an external magnetic field results in a tunable deflection angle of transmitted radiation. The active behaviour stems from an interplay between position dependent phase accumulation via the relative concentrations of the dielectric and metallic particles and actively adjustable phase accumulation via photonic anisotropic magnetoresistance. The theoretical discussion is supported by finite difference time domain calculations. Moreover, an active router is experimentally demonstrated, providing a proof of concept for more complex devices.

Anisotropic magnetoresistance and spin accumulation, which originate due to electron spin, can be observed in the plasmonic enhanced transmission of THz radiation through dense ensembles of metallic particles. In the same manner that the discoveries of anisotropic magnetoresistance and spin accu-

mulation led to the development of giant magnetoresistance electrical devices, Chapter 4 explores the possibility of observing modulation of plasmonic enhanced transmission of THz radiation via giant magnetoresistance. The experimental results suggest that observing such phenomena may require careful control of the particle surface conditions or large magnetic field strengths.

In Chapter 5, a modification of the plasmonic transmission of terahertz radiation through ensembles of bimetallic particles is introduced. When copper particles having a native oxide present on the surface are coated with a nano-layer of gold, it is shown that a film only several nanometers thick results in improved transmission of the high frequency components of the terahertz radiation. These experimental results introduce a regime of plasmonic transmission that has not been previously documented.

1.3 Theoretical Framework

This thesis explores artificial materials that operate via localized plasmonic oscillations in the THz regime. The active behaviour of the investigated artificial materials stems from resistivity modulation via electron spin-states in the metallic particles that support the localized plasmons. To equip the reader with the necessary theoretical knowledge, the relevant theoretical background in electromagnetics will first be discussed, along with details on modeling the optical constants of materials. While the thesis work involves localized plasmons in the THz regime, propagating surface plasmons are also discussed to elucidate the differences between the two types of plasmonic oscillations. In each case, the contrasting behaviour of plasmons in the visible and THz regimes is highlighted to provide the reader with an understanding of the distinct and dissimilar advantages of each regime. The physical underpinnings of electron-spin-based resistivity modulation are described via the solid state the-

ory of ferromagnetic metals and anisotropic magnetoresistance, spin-injection at a ferromagnetic-nonmagnetic interface, and giant magnetoresistance. A more detailed discussion of the relevant theoretical background can be found in texts on electromagnetics [25], plasmonics [26], solid state theory [27, 28], and magnetoresistance [29].

1.3.1 Electrodynamics in Matter

Classical electrodynamics theory describes the behaviour of electric and magnetic fields, and when present inside a material they induce a polarization, $\mathbf{P}$, and magnetization, $\mathbf{M}$, respectively. As such, the total electric field, $\mathbf{E}$, and total magnetic field, $\mathbf{B}$, in a material consist of the external fields that establish $\mathbf{P}$ and $\mathbf{M}$ combined with the fields induced by $\mathbf{P}$ and $\mathbf{M}$, respectively. The relationships between $\mathbf{E}$, $\mathbf{B}$, $\mathbf{P}$, and $\mathbf{M}$ are described by Maxwell's equations,

$$\nabla \times \mathbf{E} = -\frac{\partial \mathbf{B}}{\partial t} \tag{1.1a}$$

$$\frac{\nabla \times \mathbf{B}}{\mu_o} - \nabla \times \mathbf{M} = \mathbf{j}_f + \epsilon_o \frac{\partial \mathbf{E}}{\partial t} + \frac{\partial \mathbf{P}}{\partial t} \tag{1.1b}$$

$$\epsilon_o \nabla \cdot \mathbf{E} + \nabla \cdot \mathbf{P} = \rho_f \tag{1.1c}$$

$$\nabla \cdot \mathbf{B} = 0 \tag{1.1d}$$

where ρ_f is the free charge, $\mathbf{j}_f$ is the free current density, and ϵ_0 and μ_0 are the permittivity and permeability of free space, respectively. Accordingly, it is convenient to define a displacement field, $\mathbf{D}$, and magnetic flux density, $\mathbf{H}$, where

$$\mathbf{D} = \epsilon_0 \mathbf{E} + \mathbf{P} \tag{1.2a}$$

$$\mathbf{H} = \frac{\mathbf{B}}{\mu_0} + \mathbf{M}. \tag{1.2b}$$

Therefore, Maxwell's equations can be re-written as,

$$\nabla \times \mathbf{E} = -\frac{\partial \mathbf{B}}{\partial t} \tag{1.3a}$$

$$\nabla \times \mathbf{H} = \mathbf{j}_f + \frac{\partial \mathbf{D}}{\partial t} \tag{1.3b}$$

$$\nabla \cdot \mathbf{D} = \rho_f \tag{1.3c}$$

$$\nabla \cdot \mathbf{B} = 0 \tag{1.3d}$$

For a material where $\mathbf{P}$ and $\mathbf{M}$ do not depend on the orientation of the material (i.e. isotropic) or position in the material (i.e. homogeneous) and are proportional to $\mathbf{E}$ and $\mathbf{H}$, respectively (i.e. linear), the electromagnetic response can be written as

$$\mathbf{P} = \epsilon_o \tilde{\chi_e} \mathbf{E} \tag{1.4a}$$

$$\mathbf{M} = \chi_m \mathbf{H} \tag{1.4b}$$

where $\tilde{\chi_e}$ and χ_m are the electric and magnetic susceptibilities, respectively. Note that $\tilde{\chi_e}$ is, in general, a complex quantity which, as will be seen in the following discussion, allows one to model energy dissipation in the material. Materials that obey Equations (1.4a) and (1.4b) have $\mathbf{D}$ and $\mathbf{H}$ that obey

$$\mathbf{D} = \epsilon_o \tilde{\epsilon} \mathbf{E} \tag{1.5a}$$

$$\mathbf{H} = \mathbf{B}/(\mu_o \mu) \tag{1.5b}$$

where $\tilde{\epsilon} = 1 + \tilde{\chi_e}$ and $\mu = 1 + \chi_m$ are the relative permittivity and relative permeability, respectively. Furthermore, the free current density in a conductor is governed by Ohm's law:

$$\mathbf{j}_f = \sigma(\mathbf{E} + v \times \mathbf{B})$$

where σ is the conductivity and v is the velocity of the charge. Typically $v << c$ (i.e. non-relativistic), where c is the speed of light, and Ohm's law reduces to

$$\mathbf{j}_f = \sigma \mathbf{E}. \tag{1.6}$$

Notably, the above formalism provides the tools to describe electromagnetic waves in dielectrics and conductors. In a dielectric there is no free charge or free current, and one can apply the curl to Equations (1.3a) and (1.3b) to obtain

$$\nabla \times (\nabla \times \mathbf{E}) = \nabla(\nabla \cdot \mathbf{E}) - \nabla^2 \mathbf{E} = \nabla \times -\frac{\partial \mathbf{B}}{\partial t} \tag{1.7a}$$

$$\nabla \times (\nabla \times \mathbf{H}) = \nabla(\nabla \cdot \mathbf{H}) - \nabla^2 \mathbf{H} = \nabla \times -\frac{\partial \mathbf{D}}{\partial t} \tag{1.7b}$$

Invoking Equations (1.3c), (1.3d), (1.5a) and (1.5b) yields

$$\nabla^2 \mathbf{E} = \mu_o \mu \epsilon_o \tilde{\epsilon} \frac{\partial^2 \mathbf{E}}{\partial t^2} \tag{1.8a}$$

$$\nabla^2 \mathbf{B} = \mu_o \mu \epsilon_o \tilde{\epsilon} \frac{\partial^2 \mathbf{B}}{\partial t^2} \tag{1.8b}$$

which are simply wave equations. For simplicity in presenting an intuitive physical picture of electromagnetic wave propagation, the fields are assumed to have no spatial variation along the directions perpendicular to the direction of propagation. Therefore, the above equations admit plane-wave solutions given by

$$\mathbf{E} = \mathbf{E}_o e^{i(\tilde{\mathbf{k}} \cdot \mathbf{r} - \omega t + \phi_o)}, \mathbf{B} = \mathbf{B}_o e^{i(\tilde{\mathbf{k}} \cdot \mathbf{r} - \omega t + \phi_o)} \tag{1.9}$$

where $\mathbf{E}_o$ and $\mathbf{B}_o$ are the position-independent electric and magnetic field amplitudes, respectively, $\tilde{\mathbf{k}} = \sqrt{\mu_o \mu \epsilon_o \tilde{\epsilon}} \omega \hat{\mathbf{n}}$ is the wave vector, $\mathbf{r}$ is the position vector, ϕ_o is the phase of the plane wave at time $t = 0$ and position $\mathbf{r} = 0$, and

$\hat{\mathbf{n}}$ is a unit vector with direction perpendicular to $\mathbf{E}_o$ and $\mathbf{B}_o$, which coincides with the direction of the plane wave propagation. The wave vector magnitude is given by

$$\tilde{k} = \frac{\omega}{c}\sqrt{\mu\tilde{\epsilon}} = k + i\kappa \tag{1.10}$$

where $c = 1/\sqrt{\mu_o\epsilon_o}$ is the speed of light. $\tilde{k}$ is a complex quantity due to the assumption that $\tilde{\chi_e}$, and hence $\tilde{\epsilon}$, is complex. By inserting Equation (1.10) into Equation (1.9) and utilizing a coordinate system where the direction of $\tilde{\mathbf{k}}$ is along the positive z-axis, one obtains

$$\mathbf{E} = \mathbf{E}_o e^{-\kappa z} e^{i(kz-\omega t+\phi_o)}, \mathbf{B} = \mathbf{B}_o e^{-\kappa z} e^{i(kz-\omega t+\phi_o)}. \tag{1.11}$$

Here the physical interpretation of κ is revealed, where it is seen that electric and magnetic fields entering the material decay over a characteristic "skin depth" given by $\alpha = 1/\kappa$.

To describe the interaction of the electromagnetic fields with a metal, one must allow $\mathbf{j}_f \neq 0$. Therefore, by using a procedure similar to that used in the dielectric treatment above, one realizes the equations

$$\nabla^2\mathbf{E} = \mu_o\mu\epsilon_o\tilde{\epsilon}\frac{\partial^2\mathbf{E}}{\partial t^2} + \mu_o\mu\sigma\frac{\partial\mathbf{E}}{\partial t} \tag{1.12a}$$

$$\nabla^2\mathbf{B} = \mu_o\mu\epsilon_o\tilde{\epsilon}\frac{\partial^2\mathbf{B}}{\partial t^2} + \mu_o\mu\sigma\frac{\partial\mathbf{B}}{\partial t} \tag{1.12b}$$

Interestingly, the solution to these equations can still be plane waves described by Equation (1.9), except here $\tilde{k}^2 = \mu_o\mu\epsilon_o\tilde{\epsilon}\omega^2 + i\mu_o\mu\sigma\omega$. As such, σ provides a loss mechanism in the material. Accordingly, convention dictates to simply absorb the effects of σ into the complex permittivity, $\tilde{\epsilon}$, as will be seen in the next section.

It is important to mention the property of superposition for propagat-

ing electromagnetic waves. It can easily be seen through substitution that if $\{\mathbf{E}_1 = \mathbf{E}_{o,1}e^{i(\tilde{\mathbf{k}}\cdot\mathbf{r}-\omega_1 t+\phi_1)}, \mathbf{E}_2 = \mathbf{E}_{o,2}e^{i(\tilde{\mathbf{k}}\cdot\mathbf{r}-\omega_2 t+\phi_2)}, \ldots \mathbf{E}_j = \mathbf{E}_{o,j}e^{i(\tilde{\mathbf{k}}_j\cdot\mathbf{r}-\omega_j t+\phi_j)}\}$ are all linearly independent solutions to the wave equation [Equation (1.12)], then a linear combination of any $\mathbf{E}_j$ also solves the wave equation, where j is an integer. Therefore, the frequency content of any arbitrary electromagnetic signal can be physically understood as the summation of a series of monochromatic waves.

1.3.2 Modeling Permittivity and Conductivity

In Section 1.3.1 the parameters $\tilde{\epsilon}$ and σ were introduced, but their physical origin has yet to be discussed. As mentioned earlier, $\tilde{\epsilon}$ for a dielectric arises due to the polarization of atoms in the material. The atoms are polarized due to bound electrons being displaced from the nucleus of the atom via an electric field, which will be defined as $E = E_o e^{-i\omega t}$. Therefore, an electron under a driving electromagnetic force, $-eE_o e^{-i\omega t}$, will be considered, where $e = 1.6 \times 10^{-19}C$ and m^* are the charge and effective mass of the electron, respectively, and ω is the driving frequency. Since the electron is bound, any displacement will result in a restoring force that, for small amplitude oscillations, can be estimated using a simple harmonic oscillator model as $-m^*\omega_o^2 x$, where x is the position of the electron from equilibrium and ω_o is its natural oscillation frequency. Assuming a damping force of the electron motion given by $-m^*\nu dx/dt$, where ν is the damping rate, the equation of motion of the electron is given by

$$\frac{d^2x}{dt^2} + \nu\frac{dx}{dt} + \omega_0^2 x = \frac{-e}{m^*}E_o e^{-i\omega t} \tag{1.13}$$

In dielectric materials where the electrons are bound to the atom, ν can be attributed to reradiation by the displaced electrons [25]. At steady state, the electron oscillates at the driving frequency and has motion given by $x(t) = x_o e^{-i\omega t}$. Therefore, x_o can be determined by substitution of $x(t)$ into Equation (1.13), and the dipole moment is given by

$$p(t) = -ex(t) = \frac{e^2/m^*}{\omega_0^2 - \omega^2 - i\nu\omega} E_o e^{-i\omega t} \tag{1.14}$$

Within a molecule, there are numerous electrons which, depending on their situation in the molecule, generally have different ω_o and ν. The total polarization of the medium is the sum of the contributions from all electrons and, hence,

$$\mathbf{P} = \frac{N_m e^2}{m^*} \left(\sum_j \frac{f_j}{\omega_{0,j}^2 - \omega^2 - i\nu_j\omega} \right) \mathbf{E} \equiv \epsilon_o \tilde{\chi_e} \mathbf{E} \tag{1.15}$$

where N_m is the molecules per unit volume, and f_j (i.e. oscillator strength) is the number of electrons in each molecule with natural frequency $\omega_{0,j}$ and damping frequency ν_j. With $\tilde{\chi_e}$ defined by Equation (1.15), one can write the permittivity as

$$\epsilon(\omega) = 1 + \frac{N_m e^2}{\epsilon_o m^*} \left(\sum_j \frac{f_j}{\omega_{0,j}^2 - \omega^2 - i\nu_j\omega} \right) \tag{1.16}$$

which is known as the Drude-Lorentz model.

In a conductor, the valence electrons are not bound to the atoms and, as such, their response to electromagnetic fields is quite different. Since the conduction electron is not bound, there is no restoring force, and the primary mechanism responsible for the damping frequency, ν, is scattering of the conduction electrons from bound electrons, atoms, defects, etc. Therefore the

equation of motion is

$$\frac{d^2x}{dt^2} + \nu\frac{dx}{dt} = \frac{-e}{m^*}E_o e^{-i\omega t}. \tag{1.17}$$

At steady state, the electron will have motion given by $x(t) = x_o e^{-i\omega t}$ and, by substitution into Equation (1.17), one obtains

$$x(t) = \frac{-e}{m^*(-\omega^2 - i\nu\omega)}E_o e^{-i\omega t} \tag{1.18}$$

Associated with the electron motion is a free current density given by

$$j_f = -N_e e\frac{\partial x}{\partial t} = \frac{N_e e^2}{m^*(\nu - i\omega)}E_o e^{-i\omega t} \equiv \sigma E_o e^{-i\omega t} \tag{1.19}$$

where N_e is the conduction electron density. Therefore, Equation (1.19) gives the frequency dependent conductivity for the conduction electrons. Interestingly, by substituting Equation (1.19) into Equation (1.3b) and assuming the conduction electrons are primarily responsible for the electromagnetic response of the metal, one obtains

$$\begin{aligned}\nabla \times \mathbf{H} &= \frac{N_e e^2}{m^*(\nu - i\omega)}\mathbf{E} - i\omega\epsilon_o\mathbf{E} \\ &= -i\omega\left(\epsilon_o - \frac{N_e e^2}{m^*(\omega^2 + i\nu\omega)}\right)\mathbf{E} \\ &= \left(\epsilon_o - \frac{N_e e^2}{m^*(\omega^2 + i\nu\omega)}\right)\frac{\partial \mathbf{E}}{\partial t}\end{aligned} \tag{1.20}$$

As such, it is convenient to absorb the contribution from conductivity into the permittivity and write

$$\epsilon(\omega) = 1 - \frac{\omega_p^2}{\omega^2 + i\nu\omega} \tag{1.21}$$

where $\omega_p \equiv \sqrt{N_e e^2/\epsilon_o m^*}$ is the plasma frequency of the metal. Equation (1.21) is known as the Drude model. Notably, by comparing Equation (1.16)

to Equation (1.21), it is apparent that the Drude model is simply a special case of the Drude-Lorentz model, where there is only a single $\omega_{o,j}$ that is equal to zero, and f_j is the number of conduction electrons contributed by each molecule.

1.3.3 Surface Plasmon Polaritons

Governing Relations

Surface plasmon polaritons (SPPs) are electromagnetic oscillations that are confined to the interface between dielectric and metallic media. Currently there is active research into SPPs in both the visible and THz regimes. While the behaviour of the SPPs in these two regimes are distinct, the underlying physics is the same. As such, this section will describe the theoretical background that applies to both regimes, and then highlight the differences between them.

Since the SPPs are bound to an interface, we consider the geometry shown in Figure 1.1, where the interface is located at $z = 0$, the propagation of the

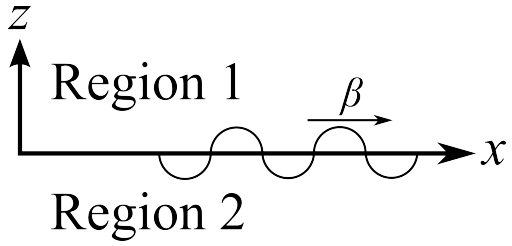

Figure 1.1: Schematic of the geometry for a surface plasmon polariton traveling in the positive x-direction with wave vector amplitude β and located at the interface between Region 1 and Region 2.

SPP's is along the x-direction, and there is no variation of $\mathbf{E}$ in the y-direction. The half space located at $z > 0$ is denoted as Region 1, while the half space at $z < 0$ is denoted as Region 2. With these assumptions one can write $\mathbf{E} = \mathbf{E}(z)e^{i\beta x - i\omega t}$ and $\mathbf{H} = \mathbf{H}(z)e^{i\beta x - i\omega t}$, where β is the wave vector amplitude

associated with the propagating SPP. To determine the behaviour of **E** and **H**, we utilize Maxwell's curl equations [Equations (1.3a) and (1.3b)] which, for the above assumptions, reduce to six equations given by:

$$\frac{\partial^2 H_y}{\partial z^2} + (k_o^2 \tilde{\epsilon}\tilde{\mu} - \beta^2) H_y = 0 \tag{1.22a}$$

$$E_x = -i \frac{1}{\omega \epsilon_o \tilde{\epsilon}} \frac{\partial H_y}{\partial z} \tag{1.22b}$$

$$E_z = -\frac{\beta}{\omega \epsilon_o \tilde{\epsilon}} H_y \tag{1.22c}$$

$$\frac{\partial^2 E_y}{\partial z^2} + (k_o^2 \tilde{\epsilon}\tilde{\mu} - \beta^2) E_y = 0 \tag{1.22d}$$

$$H_x = i \frac{1}{\omega \mu_o \tilde{\mu}} \frac{\partial E_y}{\partial z} \tag{1.22e}$$

$$H_z = \frac{\beta}{\omega \mu_o \tilde{\mu}} E_y \tag{1.22f}$$

Notably, the first three equations are independent of the last three, and the two independent sets of equations are identified as the transverse magnetic (TM) and transverse electric (TE) modes, respectively.

Let us first consider the TM mode. Since the SPP is confined to the interface, it can be written

$$Hy = \begin{cases} A_1 e^{i\beta x} e^{-\tilde{\kappa_1} z} e^{-i\omega t}, z > 0 \\ A_2 e^{i\beta x} e^{\tilde{\kappa_2} z} e^{-i\omega t}, z < 0 \end{cases} \tag{1.23}$$

where $\mathrm{Re}(\tilde{\kappa_1}) > 0$ and $\mathrm{Re}(\tilde{\kappa_2}) > 0$. Note that $\tilde{\kappa_1}$ and $\tilde{\kappa_2}$ are complex to maintain generality, and $\mathrm{Re}(\ldots)$ signifies the real part of a complex number. By inserting Equation (1.23) into Equation (1.22b) and enforcing continuity of E_y and H_x at $z = 0$, one finds that $A_1 = A_2$ and $-A_1 \tilde{\kappa_1} \tilde{\epsilon_2} = A_2 \tilde{\kappa_2} \tilde{\epsilon_1}$, respectively. Combining these results yields

$$\frac{\tilde{\kappa_1}}{\tilde{\kappa_2}} = -\frac{\tilde{\epsilon_1}}{\tilde{\epsilon_2}} \tag{1.24}$$

Since $\mathrm{Re}(\tilde{\kappa_1}) > 0$ and $\mathrm{Re}(\tilde{\kappa_2}) > 0$ for the electromagnetic wave to be bound to the interface, it can be deduced from Equation (1.24) that $\mathrm{Re}(\tilde{\epsilon_1})$ and $\mathrm{Re}(\tilde{\epsilon_2})$ must be of opposite sign. That is, for the wave to be confined to the interface, one of the regions must be an insulator while the other is a metal.[1] Furthermore, substituting Equation (1.23) into Equation (1.22a) yields the relations

$$\tilde{\kappa_1}^2 = \beta^2 - k_o^2 \tilde{\epsilon_1} \tag{1.25a}$$

$$\tilde{\kappa_2}^2 = \beta^2 - k_o^2 \tilde{\epsilon_2} \tag{1.25b}$$

For most naturally occurring nonmagnetic materials $\tilde{\mu} = 1$. Combining this assumption with Equation (1.24) yields an expression that, when solved for β, describes the well known dispersion relation of the SPP's and is given by

$$\beta = k_o \sqrt{\frac{\tilde{\epsilon_1}\tilde{\epsilon_2}}{\tilde{\epsilon_1} + \tilde{\epsilon_2}}} \tag{1.26}$$

Interestingly, the argument of the square root in Equation (1.26) has a similar form to that of parallel resistances, and describes the effective permittivity of the interface. As a final note, two important parameters in characterizing SPP's are the propagation length, L, and decay length, a, which are the characteristic distances it takes the intensity of the SPP fields to decay along x- and z-directions, respectively, and are given by

$$L = (2\mathrm{Im}[\beta])^{-1} \tag{1.27a}$$

$$a = (2\mathrm{Re}[\tilde{\kappa}])^{-1} \tag{1.27b}$$

[1] Note that this conclusion assumes $\mathrm{Im}(\tilde{\epsilon_1}) > 0$ and $\mathrm{Im}(\tilde{\epsilon_2}) > 0$, which is normally required for physical solutions since $\mathrm{Im}(\tilde{\epsilon}) < 0$ would indicate amplification of the fields. Perhaps by utilizing an amplifying medium, this requirement could be loosened.

Let us now consider the TE mode. By using the analogous procedure as for the TE mode, the following equations are realized,

$$\frac{\tilde{\kappa_1}}{\tilde{\kappa_2}} = -\frac{\tilde{\mu_1}}{\tilde{\mu_2}} \tag{1.28a}$$

$$\beta = k_o \sqrt{\frac{\tilde{\mu_1}\tilde{\mu_2}(\tilde{\epsilon_1}\tilde{\mu_2} - \tilde{\epsilon_2}\tilde{\mu_1})}{\tilde{\mu_2}^2 - \tilde{\mu_1}^2}} \tag{1.28b}$$

In most naturally occurring materials $\tilde{\mu} > 0$, which results in a contradiction in Equation (1.28a) since $\mathrm{Re}(\tilde{\kappa_1}) > 0$ and $\mathrm{Re}(\tilde{\kappa_2}) > 0$ for confinement. Therefore, *under normal circumstances*, it is impossible to excite a TE mode SPP. However, by utilizing a material with $\mathrm{Re}(\tilde{\mu}) < 0$, an SPP confined to the interface having a dispersion relation given by (1.28b) can be realized. Although such a situation is beyond the scope of this thesis, it is possible via the use of metamaterials [30].

SPP's in the Terahertz and Visible Regimes

While the dispersion relation for SPP's is given by Equation (1.26) for both the visible and THz regimes, the characteristics of the SPP's are dissimilar due to large differences between the permittivities of metals in the two regimes. As such, let us first consider visible SPP's on an interface between silver ($\tilde{\epsilon}_1$) and air ($\tilde{\epsilon}_2 = 1$), where data for $\tilde{\epsilon}_1$ is obtained from [14]. As shown in Figure 1.2 (a), a clear resonance is observed at a frequency denoted as the surface plasmon frequency, ω_{SP}, which occurs near the plasma frequency of the metal. The light line in air, $k_o = \omega/c$, is also shown. In the THz regime, the frequency of the radiation is much less than ω_p and no resonance is observed, as can be seen in Figure 1.2 (b). That is, $\beta \approx k_o$ and $\mathrm{Im}\beta << k_o$ due to the high permittivity of metals at THz frequencies precluding significant penetration of the radiation into the metal ($|\tilde{\epsilon_1}| \sim 10^5$ for $\omega/2\pi = 1$ THz). Here, data for $\tilde{\epsilon}_1$

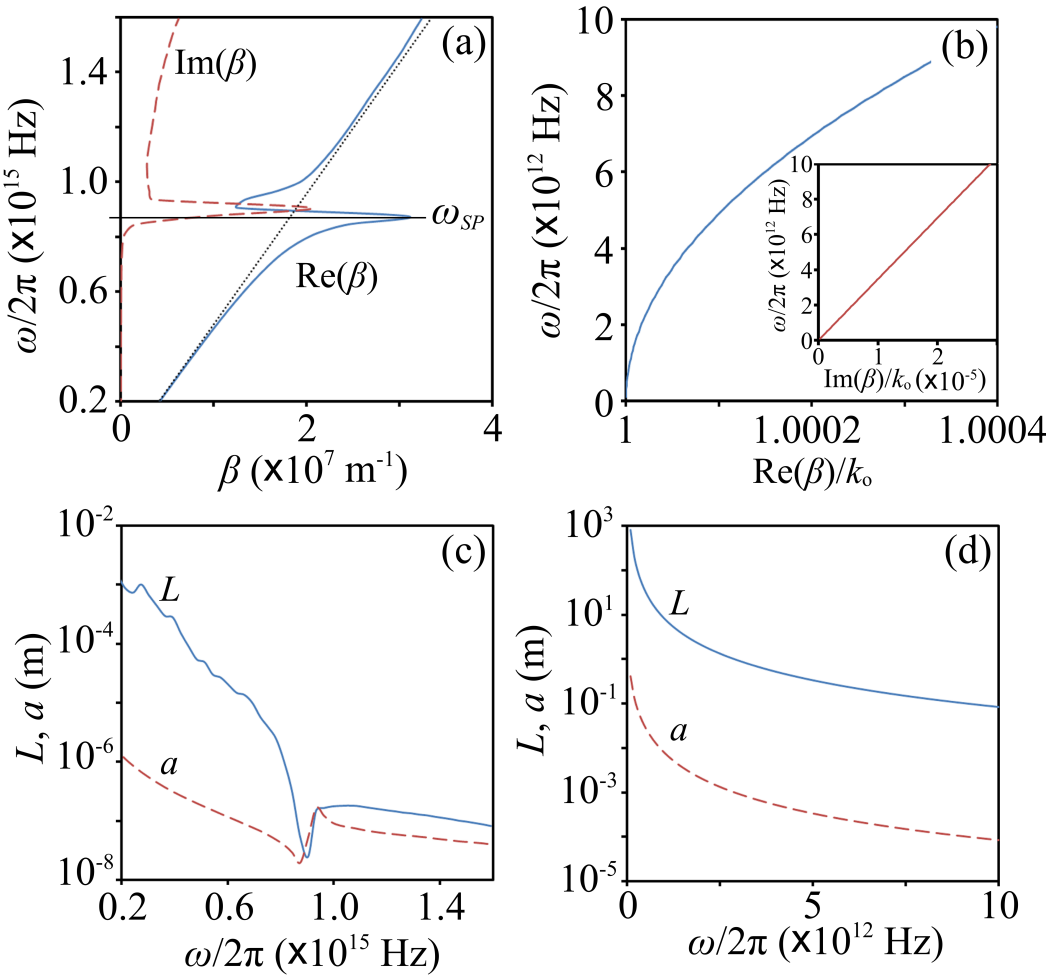

Figure 1.2: (a) Plot of the frequency dependence of Re(β) (solid), Im(β) (dashed), and the light line, k_o (dotted). Panel (b) depicts Re(β)/k_o and the inset of (b) depicts Im(β)/k_o. Panels (c) and (d) depict the frequency dependence of L and a for the visible and THz regimes, respectively.

is obtained using Drude model parameters from [13]. To directly compare the primary differences between these two regimes, the decay length in air (a) and propagation length (L) are depicted in Figure 1.2 (c) and (d) for the visible and THz regimes, respectively. At visible frequencies $a << \lambda_o$ (e.g. $a \approx 20$ nm for $\omega = \omega_{SP}$), and it is this localization of the radiation that motivates much SPP research. A major limitation of these highly confined SPP's, though, is that L is very short (e.g. $L \approx 50$ nm for $\omega = \omega_{SP}$). At THz frequencies, the scenario is quite different because, while L is relatively large (e.g. $L \sim 1$ m), the SPP is not well confined (e.g. $a \sim 1$ mm). In this regime, the SPP's are also known as Sommerfeld-Zenneck waves.

Due to the contrasting behaviours of SPP's in each regime the suitable applications for each are quite different. While the localization of light at visible frequencies shows promise in subwavelength electrical-optical devices [8], the large propagation lengths at THz frequencies may be suitable for wave-guiding [15]. Interestingly, it has been shown that by implementing a corrugated surface, a metal can be described by an effective medium that has a plasma frequency determined by the geometry [31]. By establishing an effective plasma frequency in the THz regime, so-called "designer plasmons" at THz frequencies can be realized [16].

1.3.4 Localized Surface Plasmons

Governing Relations

While SPP's are propagating electromagnetic waves coupled to the interface between a metal and dielectric material, localized surface plasmons are non-propagating. These plasmon modes arise when sub-wavelength sized metallic structures are coupled to an electromagnetic field. To formulate the theoretical background, the quasi-static approximation can be implemented if the

amplitude and phase of the electric and magnetic fields are uniform across the extent of the particle. While the external fields in the vicinity of the particle are approximately uniform for a particle diameter $d << \lambda_o$, the uniformity of the fields inside the particle is dependent on $\tilde{\epsilon}$. For the amplitude of the internal fields to be uniform, d must be much smaller than the skin depth, $1/\kappa$, and similarly, for the phase of the internal fields to be uniform, $d << 1/k$. By invoking the $\tilde{\epsilon}$-dependence of k and κ given by Equation (1.10), assuming $\mu = 1$, and defining a size parameter as $x = \pi\omega d/2c$, the quasi-static conditions can be written as

$$4x\mathrm{Im}\sqrt{\tilde{\epsilon}} << 1 \tag{1.29a}$$

$$4x\mathrm{Re}\sqrt{\tilde{\epsilon}} << 1 \tag{1.29b}$$

In the visible regime, Equations (1.29a) and (1.29b) are satisfied, and as such, at any instant in time the particle can be considered to be immersed in an electrostatic field. As such, the spatial distribution of the electric potential, Φ, can be determined via the Laplace equation, $\nabla^2\Phi = 0$. Let us consider a metallic sphere immersed in a static electric field, $\mathbf{E} = E_o\hat{\mathbf{z}}$, as shown in Figure 1.3. The dielectric medium surrounding the sphere has a permittivity ϵ_d while the sphere has a permittivity $\tilde{\epsilon}(\omega)$. For such an arrangement, the general solution to the Laplace equation can be shown to be [25]

$$\Phi(r,\theta) = \sum_{l=0}^{\infty}[A_l r^l + B_l r^{-(l+1)}]P_l(\cos\theta) \tag{1.30}$$

where $P_l(cos\theta)$ are Legendre Polynomials of order l, r is the distance from the origin, and θ is the angle subtended from the positive z-axis. The coefficients A_l and B_l can be determined by implementing boundary conditions, which are as follows: (1) the potential should be finite at $r = 0$; (2) the normal

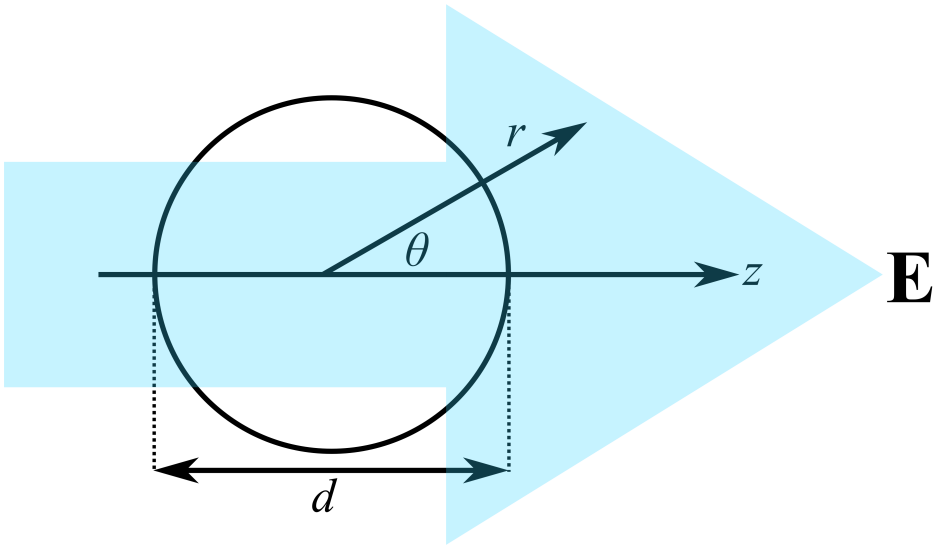

Figure 1.3: Schematic of a metallic sphere immersed in a static electric field **E**.

component electric displacement should be continuous at $r = d/2$; (3) the tangential component of the electric field should be continuous at $r = d/2$; and (4) $\Phi = -E_o z = -E_o r\cos\theta$ for $r >> d/2$. Enforcing the boundary conditions yields expressions for the potential inside (Φ_{in}) and outside (Φ_{out}) the sphere given by

$$\Phi_{in} = -\frac{3\epsilon_d}{\tilde{\epsilon} + 2\epsilon_d} E_o r\cos\theta \tag{1.31a}$$

$$\Phi_{out} = -E_o r\cos\theta + \frac{\tilde{\epsilon} - \epsilon_d}{\tilde{\epsilon} + 2\epsilon_d} E_o \left(\frac{d}{2}\right)^3 \frac{\cos\theta}{r^2} \tag{1.31b}$$

Interestingly, the potential outside the sphere is the superposition of the potential due to the applied field with that of a dipole, given that the potential of a dipole has the form [25]

$$\Phi = \frac{1}{4\pi\epsilon_o\epsilon_d}\frac{p\cos\theta}{r^2} \tag{1.32}$$

where p is the dipole moment. As such, polarizability of the sphere, α, is

obtained through the definition $p = \epsilon_o \epsilon_d \alpha E_o$ to be

$$\alpha = 4\pi \left(\frac{d}{2}\right)^3 \frac{\tilde{\epsilon} - \epsilon_d}{\tilde{\epsilon} + 2\epsilon_d} \tag{1.33}$$

Since the frequency dependence of Equation (1.33) is incorporated via the frequency dependence of $\tilde{\epsilon}(\omega)$, it describes the plasmonic response of a sub-wavelength particle in any frequency regime if Equations (1.29a) and (1.29b) are satisfied. At visible frequencies $\tilde{\epsilon} \sim -1 + i$ [14], and Equations (1.29a) and (1.29b) are satisfied for $d < 10$ nm. At THz frequencies $\tilde{\epsilon} \approx -10^4 + i10^4$ [13], and Equations (1.29a) and (1.29b) are satisfied for $d < 10^2$ nm. Since the wavelengths corresponding to THz frequencies are ~ 300 µm and the skin depth of metals in the THz regime are ~ 100 nm [32], when $d >> 100$ nm Equations (1.29a) and (1.29b) are not satisfied and the sub-wavelength particle behaves as though it is perfectly conducting. To study the localized plasmons in this unique regime, the same geometry as that shown in Figure 1.3 is considered for a perfectly conducting sphere. It should be noted that since it is assumed that there are no fields present in the particle, the quasi-static conditions described by Equations (1.29a) and (1.29b) are no longer applicable, and the only required quasi-static condition is $d << \lambda_o$. It can easily be shown that solving the Laplace equation for this geometry yields a potential given by [25]

$$\Phi_{in} = 0 \tag{1.34a}$$

$$\Phi_{out} = -E_o r \cos\theta + E_o \left(\frac{d}{2}\right)^3 \frac{\cos\theta}{r^2}. \tag{1.34b}$$

The field outside the sphere is a superposition of the applied electric field with that of a dipole, where the polarizability is given by the frequency independent

value

$$\alpha_{THz} = \frac{\pi d^3}{2}. \tag{1.35}$$

It is interesting to note that by taking the limit of Equation (1.33) as $\tilde{\epsilon}$ approaches infinity, an expression equivalent to that in Equation (1.35) is obtained. Therefore, the dipolar response for a subwavelength particle in the THz regime scales with the particle size in the same way as a subwavelength particle in the visible regime.

The discussion thus far has been rooted in electrostatics. Time varying fields can be described provided that the quasi-static approximation is applicable, and that the dipolar response of the particle occurs over time scales that are shorter than the time scales over which the electromagnetic fields vary. The characteristic time it takes for charge to dissipate to the surface of a conductor is on the order of the scattering time, τ_c [33], and for a good conductor like copper $\tau_c \sim 10^{-14}$ s [25]. These conditions are clearly satisfied for a subwavelength particle in the THz regime, where fields vary over time scales $\sim$ 1 ps. Therefore, when the particle is illuminated by a plane wave described by $\mathbf{E}(t) = \mathbf{E}_o e^{-i\omega t}$, an oscillating dipole moment given by

$$\mathbf{p}(t) = \epsilon_o \epsilon_d \alpha_{THz} \mathbf{E}_o e^{-i\omega t} \tag{1.36}$$

is induced in the particle [26], where α_{THz} is the polarizability given by Equation (1.35).

Localized Surface Plasmons in the Terahertz and Visible Regimes

It is evident that in Equation (1.33), if $\tilde{\epsilon} = -2\epsilon_d$, the polarizability will become extremely large. It turns out that this resonant response is observed in the visible regime and, to illustrate this, $|\alpha(\omega)|$ [Equation (1.33)] is depicted in

Figure 1.4 for an Ag particle in air using experimentally obtained data for $\tilde{\epsilon}(\omega)$ [14]. Note that $\tilde{\epsilon}(\omega)$ is not estimated using a Drude model fit, but in [14] it is obtained direct from reflection and transmission measurements. The frequency dependence of $|\alpha(\omega)|$ is dictated by $\tilde{\epsilon}$, and d only serves as a scaling factor. Clearly a resonant region exists (region "A" in Figure 1.4), and accordingly, at the resonant frequency the enhanced polarizability leads to high energy confinement. Note that the slight dip in the polarizability (region "B" in Figure 1.4) is due to the contribution of interband absorption to $\tilde{\epsilon}$ [14]. The resonant energy confinement manifests at a well defined frequency that can be tuned by varying the particle size, which shows promise for a number of applications including optical sensing and emission enhancement [26].

For localized surface plasmons at THz frequencies in particles with size much larger than the skin depth, α is a constant value that depends only on the size of the particles [Equation (1.35)], as portrayed in the inset of Figure 1.4. Clearly there is no resonance; however, the particles are indeed polarized as can be inferred from the finite, non-zero value of α.

Another important distinction between localized plasmons in the visible and THz regimes involves the roles of the displacement current, j_d, and free electron current, j_F. The behaviour of these two types of currents is elucidated by examining the wave equation for a metal under harmonic excitation:

$$\nabla^2 \mathbf{E} = \mu_o \mu \frac{\partial}{\partial t} (j_d + j_F) \tag{1.37a}$$

$$j_d = -i\epsilon\epsilon_o \omega \mathbf{E} \tag{1.37b}$$

$$j_F = \sigma \mathbf{E} \tag{1.37c}$$

In the visible regime, $|\mathrm{Re}(\tilde{\epsilon})| > |\mathrm{Im}(\tilde{\epsilon})|$ dictates that j_d is the dominant current term. However in the THz regime, where metals are often considered perfect

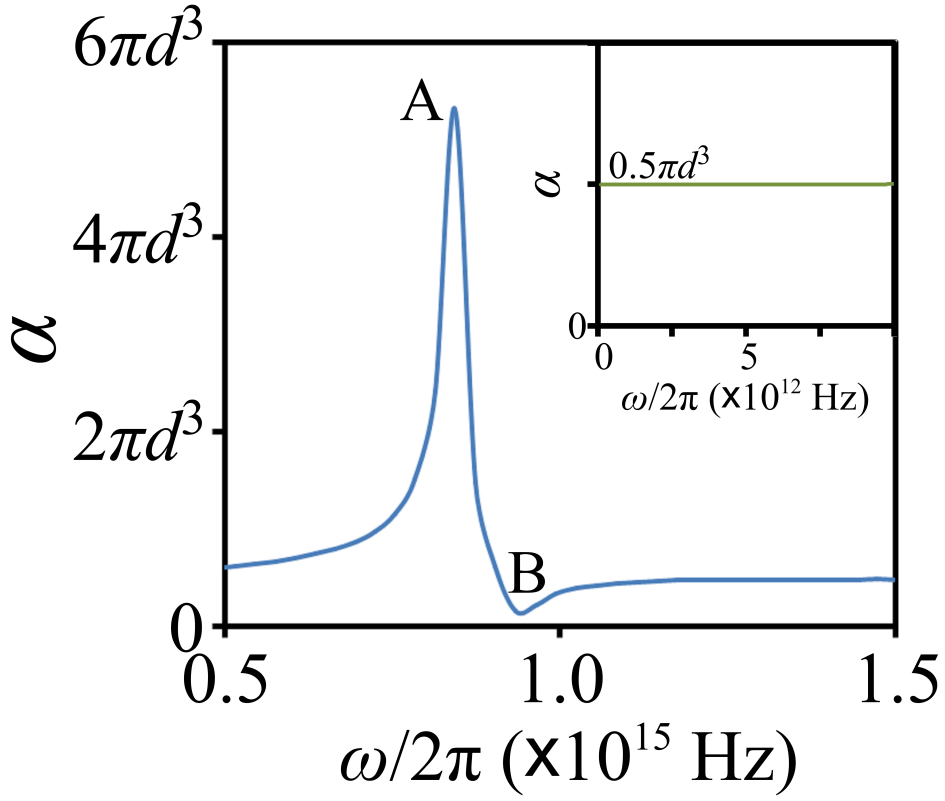

Figure 1.4: Plot of the frequency dependence of $|\alpha|$ for a subwavelength Ag sphere in the visible regime using experimental data for $\tilde{\epsilon}(\omega)$ [14]. The inset depicts $|\alpha|$ for a subwavelength Ag sphere in the THz regime.

conductors due to the large values of σ, the free current dominates and the transient response of a localized SPP is dictated primarily by the conduction electrons.

Interestingly, the THz localized plasmons have been shown to couple very efficiently in particles having diameters $\sim$ 100 µm, permitting the coherent transport of THz radiation across random ensembles of densely packed sub-wavelength metallic particles [17, 18]. It is noted that ballistic transport of photons through the collection of particles is precluded by the absence of straight line trajectories through the metallic particles. Rather, the dipolar fields associated with the excited plasmon induce a plasmonic response in neighboring particles, as shown in Figure 1.5. Since the free current dominates

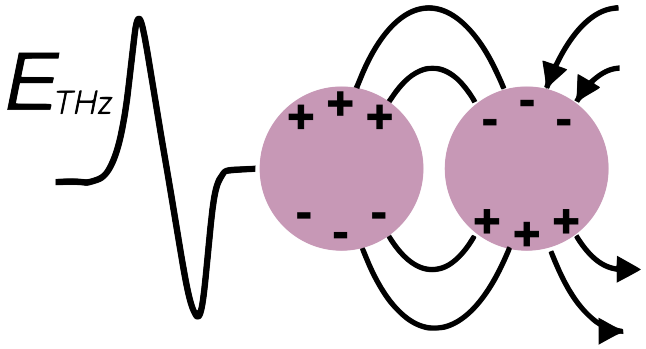

Figure 1.5: Illustration of the near-field coupling of localized plasmon modes.

the transient localized plasmon response in the THz regime, the characteristics of the THz radiation transmitted through dense ensembles of sub-wavelength metallic particles is largely governed by the conductivity of the metal. As can be seen from the Drude model [Equation (1.19)], the conductivity of metals decreases with increasing frequency, and this results in a frequency-dependent transmission that favors lower frequencies. It is important to note that this regime of transport cannot be explained by the effective medium approximation (EMA). The EMA states that a medium consisting of a mixture of subwavelength media can be described by an effective permittivity and con-

ductivity that are given by an average of the intrinsic permittivities and conductivities of the constituent materials [34]. The EMA formalism is developed under the quasi-static assumptions given by Equations (1.29a) and (1.29b). In the context of the coupling of localized plasmons in the THz regime, where the skin depth is several orders of magnitude smaller than the particle size (see above), these assumptions are not valid. While the EMA deals with the *internal* fields of each element, THz plasmonic transport is mediated by the near-field coupling of the *external* fields of each element.

1.3.5 Resistivity Modulation via Electron Spin-State

Ferromagnetic Metals

It has recently been shown that, in the context of plasmonic enhanced propagation through random metallic media, the properties of the transmission can be drastically altered by manipulating the intrinsic resistivity of a metal via the application of an external magnetic field [22–24]. The physical origins of this type of phenomenon will be be discussed by first looking at the microscopic properties of ferromagnetic metals.

In the absence of an external magnetic field, the ferromagnetic transition metals (Fe, Ni, and Co) have a spontaneous magnetic moment due to a tendency of the electron spins to align. The contrasting behaviour of the ferromagnetic transition metals and non-magnetic metals can be understood by examining their band structure. The magnetic response of a material is dictated by the outermost electron shells, which in the case of the ferromagnetic transition metals are the 3d and 4s electrons. Shown in Figure 1.6 are the density of states, $D(E)$, for a typical non-magnetic metal and ferromagnetic metal, where E is the energy. For the non-magnetic metal, the d band is full because it lies entirely below the Fermi energy, E_F. However, for the ferromag-

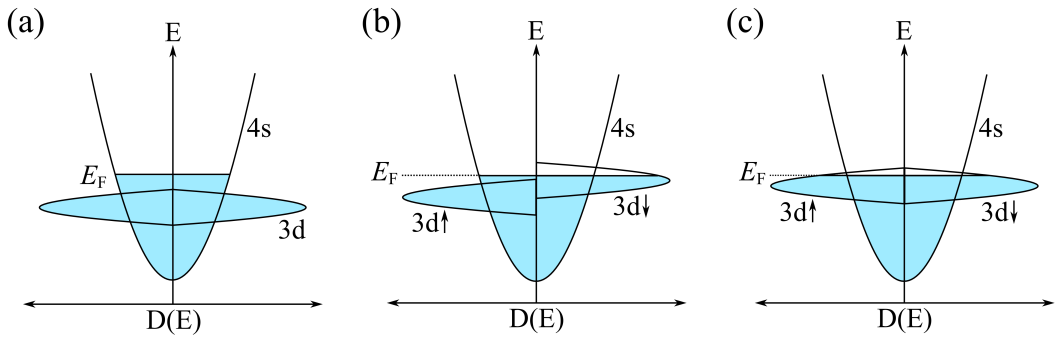

Figure 1.6: Density of states for a typical (a) non-magnetic metal (b) ferromagnetic metal below the Curie temperature, and (c) ferromagnetic metal above the Curie temperature. The shaded region represents filled states.

netic metal the 3d-band is split into two different sub-bands: one for spin-up electrons and one for spin-down electrons. The energy for the two sub-bands is different due to the quantum mechanical exchange interaction, which comes about due to the overlap of the charge distributions of neighboring atoms [27] (i.e. the neighboring electrons couple, and the preferred spin-orientation has less energy). The 3d sub-bands are only partially filled and, accordingly, the surplus of electrons in one spin-orientation results in a residual magnetization that exists even without the presence of an external magnetic field. At temperatures above the so-called "Curie temperature", the thermal motion of the electrons overcomes the effects of the exchange energy and the metal behaves paramagnetically, as illustrated by Figure 1.6 (c). A bulk piece of ferromagnetic material is composed of ferromagnetic domains that each have a saturated magnetization. The magnetization direction of neighboring domains are not necessarily parallel, and in the presence of an external magnetic field, **H**, a demagnetized bulk piece of ferromagnetic material is magnetized through two processes. At low magnetic field strengths the domains that favor the magnetic field direction increase in size while those aligned unfavorably decrease in size, which corresponds to region A of the grey curve in Figure 1.7. In strong field strengths the magnetization of entire domains rotate to lie par-

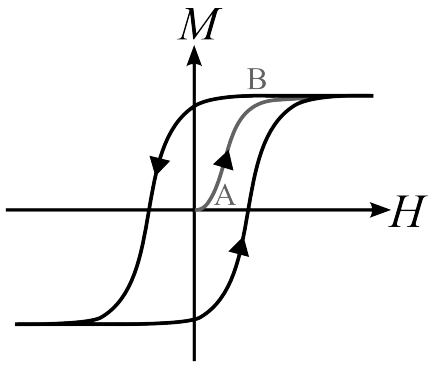

Figure 1.7: Magnetization curve for a ferromagnetic metal. The grey curve corresponds to the magnetization of a demagnetized ferromagnet (i.e. randomly oriented domains), and the black curve corresponds to a ferromagnet that has been magnetized.

allel to the field, which corresponds to region B of the grey curve in Figure 1.7. This process is irreversible, since it would require energy for the domains to revert to their initial disordered state after **H** is removed. Accordingly, after the initial magnetization of the ferromagnetic metal, the magnetization follows an approximately rectangular hysteresis curve for subsequent cycling of **H**, which corresponds to the black curve in Figure 1.7.

With a basic understanding of the physics of ferromagnetic materials established, it is now possible to discuss magnetoresistance. In ferromagnetic metals the resistivity, ρ, depends on the application of an external magnetic field, B, through the relation $\rho(B) = \rho_0 + \rho_{Lorentz}(B) + \rho_{AMR}(B)$, where ρ_0 is the background resistivity, $\rho_{Lorentz}(B)$ is the contribution from Lorentz force that is present in all metals, and $\rho_{AMR}(B)$ is the contribution from the anisotropic magnetoresistance phenomenon that is only observable in ferromagnetic metals. ρ_0 arises due to conduction electrons scattering from thermal phonons or impurities. At low temperatures the effect of phonons is precluded and the resistivity is dictated by scattering from impurity atoms and imperfections in the lattice. At higher temperatures (e.g. room temperature), the change in momentum of the conduction electrons when they scatter from phonons domi-

nantly dictates the resistivity. This behaviour is encapsulated by Matthiessen's rule, which states that the non-magnetic resistivity of a metal is given by $\rho_0 = \rho_i + \rho_T(T)$, where ρ_i is the resistivity caused by scattering from impurities/defects and $\rho_T(T)$ is the temperature-dependent resistivity caused by scattering from phonons [27].

$\rho_{Lorentz}(B)$ arises due to the magnetic induced force on the conduction electrons, $\mathbf{F}_B = e(\mathbf{v} \times \mathbf{B})$, where $\mathbf{B}$ is the magnetic field and $\mathbf{v}$ is the conduction electron velocity. To identify how this force results in a resistivity modulation, let us first consider the configuration where $\mathbf{B}$ is aligned perpendicular to the electric field, $\mathbf{E}_{current}$, that is driving the current. When $\mathbf{B}$ is turned on, $\mathbf{F}_B$ is initially perpendicular to $\mathbf{E}_{current}$. However, as the electron displacement curves slightly due to $\mathbf{F}_B$, the direction of $\mathbf{F}_B$ will shift such that a component will be antiparallel to $\mathbf{E}_{current}$, which manifests as an additional resistivity component. Conversely, when $\mathbf{B}$ is parallel to $\mathbf{E}_{current}$, $\mathbf{F}_B = 0$ and no additional resistivity is realized. It should be noted that if the radius of curvature of the conduction electrons (due to Lorentz force) is greater than the mean free path, the effect will be diminished by scattering.

Anisotropic magnetoresistance (AMR) can be explained via the 4s and 3d energy band characteristics. Since both the 3d and 4s bands are not completely filled, they both can contribute conduction electrons. However, the 3d band has a larger density of states over a much narrower energy range compared to the 4s electrons, which suggests that the 3d electrons are more confined near the atom nucleus compared to the 4s electrons. As such, scattering of 4s conduction electrons into empty 3d-states account for a significant portion of the resistance. Due to coupling between the electron spin state with the electron orbital motion (spin-orbit coupling), the energy of the d-states depends on the spin direction (i.e. magnetization direction or direction of $\mathbf{B}$). Here,

electron orbitals perpendicular to the spin direction are more energetically favored compared to orbitals parallel to the spin direction. For the ferromagnetic transition metals, this direction dependence manifests as a higher scattering cross-section for transitions into the d-band for conduction electrons moving parallel to **B** compared to when moving perpendicular to **B** [35]. Accordingly, the resistivity for the current density parallel to the magnetization direction, $\rho_{||}$, differs from the resistivity for current density perpendicular to the magnetization direction, $\rho_{\perp}$. The electric field, **E**, associated with the current, **j**, in a conductor is governed by Ohm's Law, $\mathbf{E} = \rho\mathbf{j}$, where ρ is the resistivity. In the case of AMR, where the resistivity depends on the current direction, Ohm's Law manifests as [35]

$$\mathbf{E}_{AMR} = \hat{\mathbf{u}}\rho_{\perp} |\mathbf{j}| \cos\xi + \hat{\mathbf{v}}\rho_{||} |\mathbf{j}| \sin\xi \tag{1.38}$$

where $\mathbf{E}_{AMR}$ is the electric field associated with the AMR contribution to the resistivity, ξ is the angle between the magnetization and the current direction, **j** is the current density, $\hat{\mathbf{u}}$ is a unit vector parallel to the magnetization direction, and $\hat{\mathbf{v}}$ is a unit vector perpendicular to the magnetization direction. It follows directly from Equation (1.38) that the amplitude of the electric field is given by

$$\begin{aligned} |\mathbf{E}_{AMR}| &= \sqrt{\rho_{\perp}^2 \cos^2\xi + \rho_{||}^2 \sin^2\xi}\, |\mathbf{j}| \\ &\equiv \rho_{AMR} |\mathbf{j}|\,, \end{aligned} \tag{1.39}$$

where ρ_{AMR} is the net resistivity due to AMR. By defining $\Delta\rho = \rho_{\perp} - \rho_{||}$, ρ_{AMR} can be written as

$$\rho_{AMR} = \sqrt{\rho_{\perp}^2 + 2\rho_{\perp}\Delta\rho\cos^2\xi + \Delta\rho^2\cos^2\xi} \tag{1.40}$$

In general $\Delta\rho << \{\rho_\perp, \rho_{||}\}$ [35], and therefore, the term that is second order in $\Delta\rho$ can be ignored. By implementing a binomial approximation one obtains

$$\rho_{AMR} = \rho_\perp + \Delta\rho \cos^2 \xi. \tag{1.41}$$

Spin Injection

Spin injection, which is performed by driving a current from a ferromagnetic metal into a non-magnetic metal, constitutes another form of electron-spin based resistivity modulation. After the spin-polarized electrons are injected into the metal, they will undergo spin-flip scattering events after a characteristic "spin relaxation time", τ_s. In light of this, the characteristic distance the electron will diffuse before spin-relaxation events occur (i.e. the spin diffusion length) is

$$\lambda_s = \sqrt{D\tau_s} \tag{1.42}$$

where D is the electron diffusion constant. In a simple model, any scattering event should have a small probability, a, of flipping the spin of an electron. Thus, for a scattering time of τ in the conductor, the spin-flip probability is

$$a = \tau/\tau_s \tag{1.43}$$

The next step in the development of the theory is to examine the effect of spin accumulation on the electric current passing from the ferromagnetic metal to the non-magnetic metal. Consider Figure 1.8 (a), which depicts a hybridized s-d band for an idealized ferromagnetic transition metal. Here, the Fermi surface is only in the $\downarrow$-spin sub-band, and the current passing from the ferromagnetic layer to the non-magnetic layer consists only of $\downarrow$-spin electrons. To account for the behavior of real ferromagnets, where the Fermi surface lies partly in the $\uparrow$-

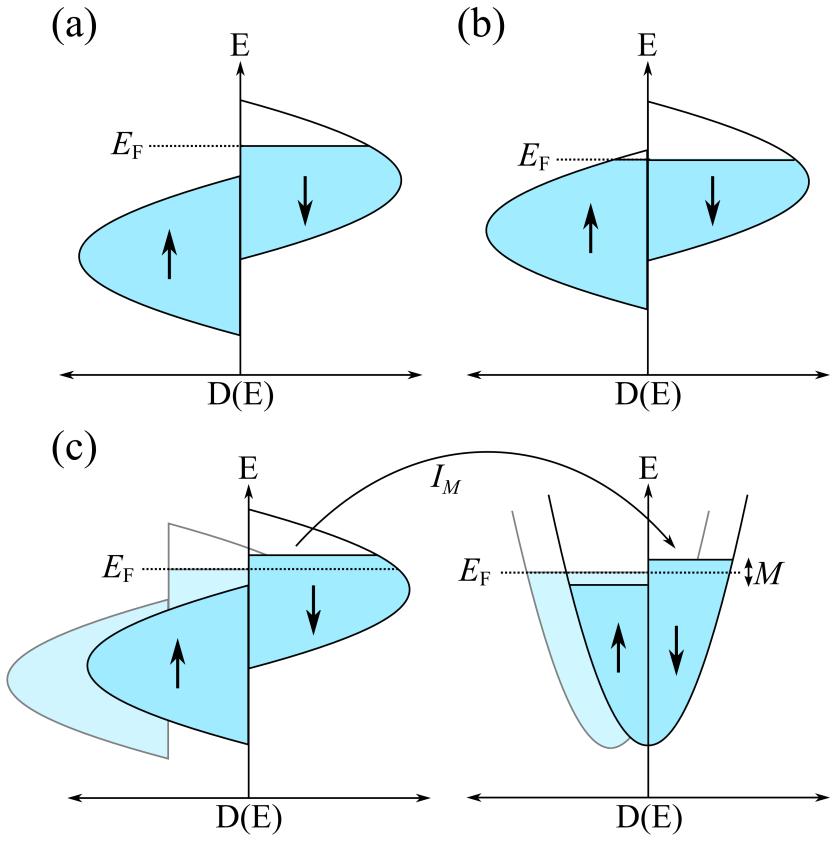

Figure 1.8: Band structure for hybridized s-d band for ferromagnetic metals with (a) a full sub-band and (b) a near full ↑-spin sub-band. Panel (c) depicts the change in band occupancy caused by an applied current through the ferromagnet and non-magnetic interface. The faded background images show the band structure before the current, I_M, is turned on, and the vertical shift in the overall band structure after the current is turned on is a result of the potential difference that is required to generate the current. The spin-polarized current generates a magnetization, M, in the ferromagnetic metal.

spin sub-band [Figure 1.8 (b)], an efficiency coefficient $\eta = (j_\downarrow - j_\uparrow)/(j_\downarrow + j_\uparrow) < 1$ is introduced, where $j_\uparrow$ and $j_\downarrow$ are the current densities of the $\uparrow$- and $\downarrow$-spin current channels, respectively. With the definition of the efficiency established, the corresponding injected magnetization current is

$$I_m = \frac{\eta \beta I_e}{e} \tag{1.44}$$

where I_e is the electric current, β is the Bohr magneton, $\eta\beta$ is the magnetization transported, and $e = 1.6 \times 10^{-19}$ C is the electron charge [36]. Thus, over a distance, $d < \lambda_s$, from the interface, and also considering that the random scattering of electron spins occurs at a rate of $1/\tau_s$, the spin-polarized current builds up a non-equilibrium magnetization,

$$M = \frac{I_m \tau_s}{Ad} \tag{1.45}$$

where A is the cross-sectional area. Accordingly, this increase of carriers in the $\downarrow$-spin band of the non-magnetic metal causes a decrease in the occupation of $\uparrow$-spin carriers such that charge neutrality is conserved [Figure 1.8 (c)]. This increase of $\downarrow$-spin sub-band occupation has the added effect of causing the chemical potential of the ferromagnet to rise and align with that of the non-magnetic metal to prevent the reverse flow of spins into the ferromagnet. Since the spin and charge are both associated with the same carrier, this thermodynamic force associated with M can alternatively be viewed as an interfacial impedance, Z_s, which stems from the non-equilibrium accumulation of spin in the non-magnetic metal, or, a "spin bottleneck" [36]. The change in chemical potential has been derived to be $eV_s = \eta\beta M/\chi$, where χ is the susceptibility [37, 38]. Finally, by using the above equations and a free electron

model for χ, the interface resistance can be written as

$$Z_s = \frac{V_s}{I_e} = \frac{\eta^2 \rho_P \lambda_s^2}{Ad}, d < \lambda_s \tag{1.46}$$

where ρ_P is the resistivity of the non-magnetic metal [9]. Additionally, for non-magnetic metal thicknesses greater than λ_s, the d-dependence of M can be written as $M \propto e^{-d/\lambda_s}$ due to the spin-relaxation processes that begin to dominate [36]. Thus, a valid approximation is that the interfacial impedance is entirely dominated by spin accumulation within λ_s (i.e. $d = \lambda_s$ in Equation (1.46)), and Z_s becomes

$$Z_s = \frac{\eta^2 \rho_P \lambda_s}{A}, d < \lambda_s \tag{1.47}$$

Giant Magnetoresistance

The basic geometry of a structure that can exhibit giant magnetoresistance (GMR) is shown in Figure 1.9, where a non-magnetic (N) metal is placed between two ferromagnetic (F) metals. For simplicity, it will be assumed that the same F metal is used on each side of the N metal. For the GMR effect to be observed, the thickness of the N-layer should be thinner than λ_s, which permits the assumption that the conduction electrons retain their initial spin-states after traveling through the N-layer. Here the current passing through the device is assumed to consist of two channels: one composed of $\uparrow$-spin electrons and the other composed of $\downarrow$-spin electrons. The resistance perceived by the current when the spin-orientation is parallel to the magnetization of the ferromagnetic layer is denoted as R_1 while the resistance when the spin-orientation is antiparallel to the magnetization of the ferromagnetic layer is denoted as R_2. As discussed earlier, the resistivity in a ferromagnetic metal

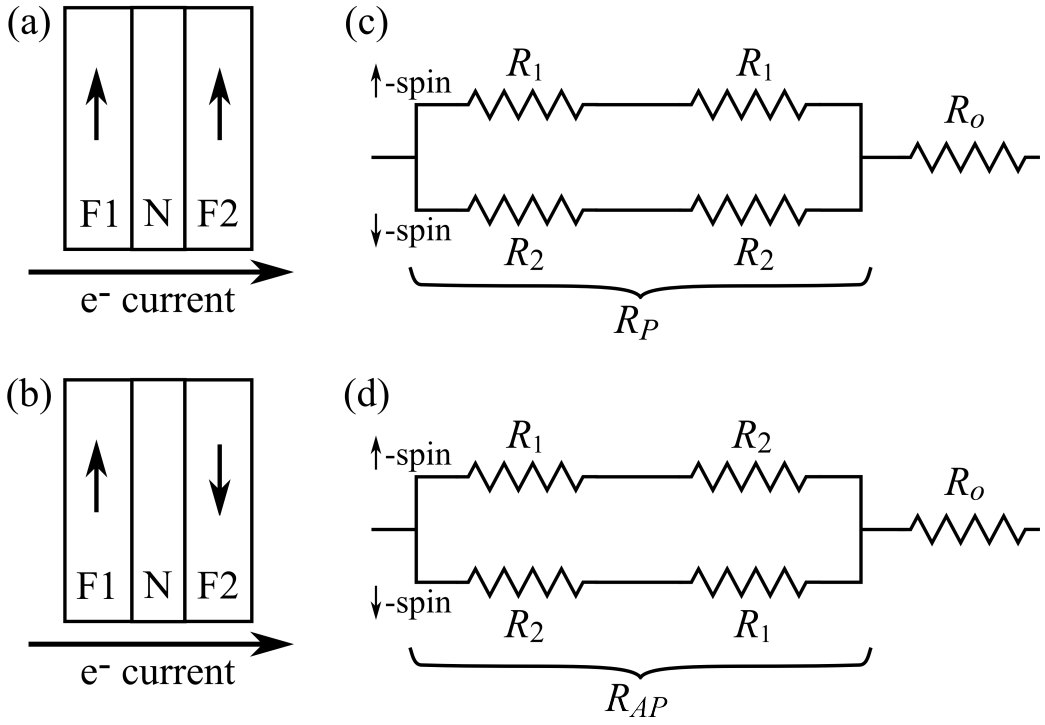

Figure 1.9: Schematic of a GMR structure consisting of ferromagnetic (F) and non-magnetic (N) layers, where the magnetizations of the two F layers are (a) parallel and (b) antiparallel. The resistance perceived by the ↑-spin and ↓-spin current channels is shown in panel (c) for the parallel configuration and panel (d) for the antiparallel configuration. R_1 and R_2 are the resistances when the spin-orientation is parallel and antiparallel to the magnetization of the ferromagnetic layer, respectively, and R_o represents the non-magnetic resistance.

is predominantly dictated by scattering of the 4s conduction electrons into the 3d states. However, as shown in Figure 1.6, the 3d sub-band consisting of electrons with spin-orientation parallel to the metal magnetization is full, precluding the scattering of 4s electrons into it. Therefore it can be written

$$R_1 < R_2. \tag{1.48}$$

The total resistance of the device depends on the relative magnetization directions of the F1 and F2. Let us first consider the configuration when the two magnetizations are parallel, as shown in Figure 1.9(a). Here, the ↑-spin electrons are parallel to the magnetization in both ferromagnetic metals, while the ↓-spin electrons are antiparallel in both. The resulting resistance for the two current channels are $R_\uparrow = 2R_1$ and $R_\downarrow = 2R_2$, as depicted in Figure 1.9(c). Thus, the net resistance is

$$\begin{aligned} R_P &= \frac{R_\uparrow R_\downarrow}{R_\uparrow + R_\downarrow} \\ &= \frac{2R_1 R_2}{R_1 + R_2} \end{aligned} \tag{1.49}$$

Note that any non-magnetic resistance, R_o, that does not depend on the magnetization of the ferromagnetic layers would simply manifest as an additional resistor connected to R_P in series, as shown in Figure 1.9(c). Now consider the antiparallel configuration, where the magnetizations of F1 and F2 are in opposite directions, as shown in Figure 1.9 (b). Here, the resistances for the ↑-spin and ↓-spin channels are $R_\uparrow = R_1 + R_2$ and $R_\downarrow = R_2 + R_1$, respectively, as depicted in Figure 1.9(d). As such, the net resistance is given by

$$R_{AP} = \frac{R_1 + R_2}{2} \tag{1.50}$$

For any situation where $R_1 \neq R_2$, it can be easily proven that $R_{AP} > R_P$.[2] Therefore, by controlling the relative spin states of the F layers, the resistance of the structure can be modulated.

There are three primary methods that can be used to control the relative orientations of the two F layers. The first method is to use an N layer thickness such that the two F layers couple antiferromagnetically via the so-called Ruderman-Kittel-Kasuya-Yosida (RKKY) interlayer exchange coupling. The basic principles behind RKKY coupling are as follows [27, 29]. In a ferromagnetic metal, the spin-orientations of the conduction electrons are magnetized in the vicinity of the magnetic ions. This magnetization has a damped oscillatory spatial dependence, and can induce a magnetization in a second magnetic ion. As such, the magnetic ions of the two F layers couple via the conduction electrons, and will align either parallel or antiparallel depending on the distance between the two layers. Also note that the thickness of the N layer must be less than the mean free path of the conduction electrons for significant coupling to occur. For a useful GMR device, the thickness must be chosen such that the layers couple antiferromagnetically, and thus, the F layers are antiparallel when there is no external magnetic field, B, applied. Applying a sufficiently strong B-field to the device causes the magnetization of both layers to align with the magnetic field, and thus be parallel. While this method typically yields high magnetoresistance, it is limited by the large B required to overcome the antiferromagnetic coupling.

A second approach to realize GMR is through exchange-biased spin-valves, which have the geometry shown in Figure 1.10(a). F is a ferromagnetic "free layer", N is a non-magnetic layer, PL is a ferromagnetic "pinned layer", and

[2]Comparing Equations (1.49) and (1.50) reveals that $R_{AP} > R_P$ if $R_1^2 + R_2^2 > 2R_1R_2$. Converting both sides of the latter relation to cylindrical coordinates then reveals that $R_1^2 + R_2^2 > 2R_1R_2$ for all $R_1 \neq R_2$.

AF is an antiferromagnetic layer. The magnetization of the PL layer is pinned along a fixed direction due to an exchange bias interaction between the PL layer and AF layer. Contrary to ferromagnetic materials, in an antiferromagnet the net spins of neighboring ions are ordered antiparallel to each other, and the net magnetic moment of the bulk material is zero. For typical field strengths (i.e. those used in spin valves), a small number of the spins align with the magnetic field and the magnetization curve is linear, as shown in Figure 1.10(b). Typically the magnetization of the antiferromagnetic layer is negligible compared to the magnetization of the ferromagnetic layers in spin valves. For extremely large magnetic field strengths, the magnetization of an antiferromagnet saturates as fewer spins are available to become aligned with the magnetic field. At the surface of an antiferromagnet there are ions that have uncompensated spins, and in contrast to the bulk of the antiferromagnet, the net surface magnetization is non-zero. Moreover, a portion of the uncompensated spins are coupled with spins in the bulk of the antiferromagnet, and are therefore pinned along a fixed direction. When in contact with a ferromagnetic layer, there is parallel coupling between these uncompensated interfacial spins and the ferromagnetic spins, and the magnetization of the ferromagnetic layer becomes pinned [39]. Reversal of the magnetization of the F layer requires additional energy to form a domain wall at the surface of the AF layer [40], which results in a shift of the magnetization curve by an amount denoted by H_B. As shown in Figure 1.10(c), for a large enough H_B, the magnetization of the PL will always revert back to a remanent magnetization after the external field, H, is removed. The N layer in the spin valve serves as a spacer layer to minimize the coupling between the PL and F layers, and the unpinned F layer (i.e. free layer) has the magnetization curve shown in Figure 1.10(d). Accordingly, as H is cycled the assymetric magnetoresistance curve

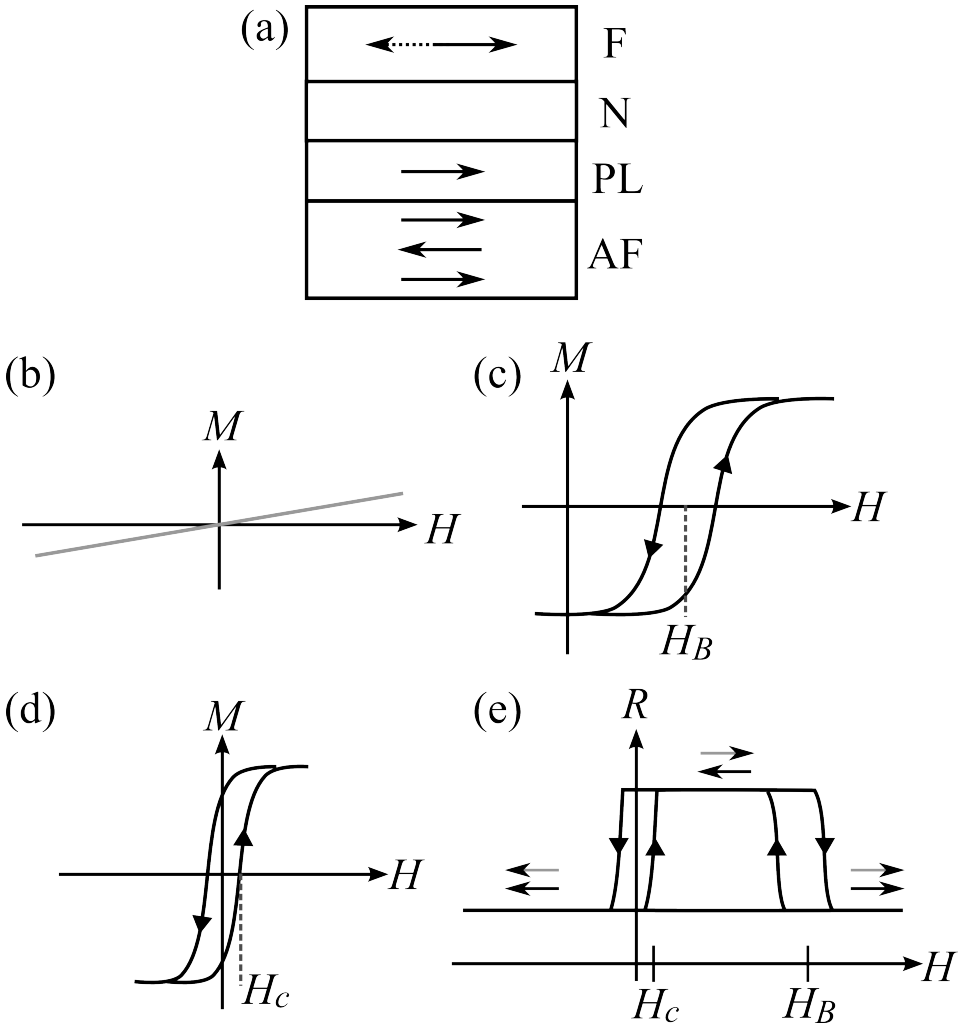

Figure 1.10: (a) Schematic of an exchange biased spin valve, which consists of an antiferromagnetic layer (AF), ferromagnetic pinned layer (PL), non-magnetic layer (N), and ferromagnetic free layer (F). Panel (b) depicts the magnetization curve of an antiferromagnet. Panel (c) depicts how an exchange bias at the AF/PL interface results in a shift of the PL magnetization curve by H_B. Panel (d) depicts the magnetization curve for the F layer and panel (e) depicts the magnetoresistance curve for the exchange biased spin valve, where the grey and black arrows represent the magnetization directions of the F and PL layers, respectively.

shown in Figure 1.10(e) is realized, where the parallel and antiparallel states correspond to low and high resistance of the device, respectively.

A further approach to implement GMR is pseudo spin valves, which do not make use of an antiferromagnetic layer, as shown in Figure 1.11(a). Here the two F layers (F1 and F2) are two dissimilar metals that have different coercivities given by H_{c1} and H_{c2} ($H_{c1} < H_{c2}$), as can be discerned from the magnetization curves for F1 and F2 depicted in Figures 1.11(b) and 1.11(c), respectively. When $H_{c1} < H < H_{c2}$, only the F1 layer is magnetized, and increasing the field such that $H > \{H_{c2}, H_{c1}\}$ results in both the F1 and F2 layers being magnetized. Contrary to exchange biased spin valves, this device architecture yields a symmetric magnetoresistance curve, as shown in Figure 1.11(d).

The ability to actively control the resistance via the application of an external magnetic field makes spin valves attractive for electronics applications. The most common use of spin valves is in hard drive read heads, where they are used to detect the magnetization of the bits on the hard drive disk. A generalized depiction of a read head is depicted in Figure 1.12(a). Here, the magnetic field of the bit, H_{bit}, dictates the magnetization of the sensor layer, which is the free layer in an exchange biased spin valve or the layer with lower coercivity in a pseudo spin valve. The device is designed such that H_{bit} is not large enough to influence the magnetization of the reference layer, and thus, the magnetization direction of the bit dictates whether the spin valve is in a high or low resistance state. A current, I_{read}, passing through the spin valve is modulated by the magnetoresistance, and can therefore transport the bit information to other areas of a device. Another application of spin valves is magnetic memory, as depicted in Figure 1.12(b). This device is similar to the read head, except a stationary write line is used to control the magnetization

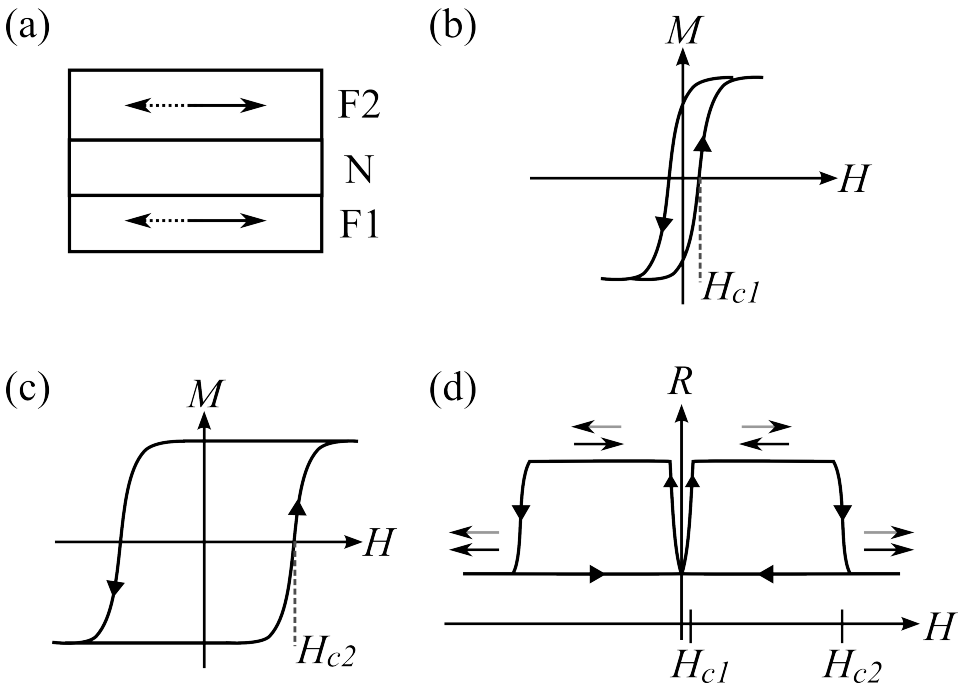

Figure 1.11: (a) Schematic of an pseudo spin valve, which consists of two ferromagnetic layers (F1 and F2) with different coercivities and a non-magnetic layer (N). Panels (b) and (c) depict the magnetization curves for the F1 and F2 layers, respectively. Panel (d) depicts the magnetoresistance curve for the pseudo spin valve, where the grey and black arrows represent the magnetization directions of the F1 and F2 layers, respectively.

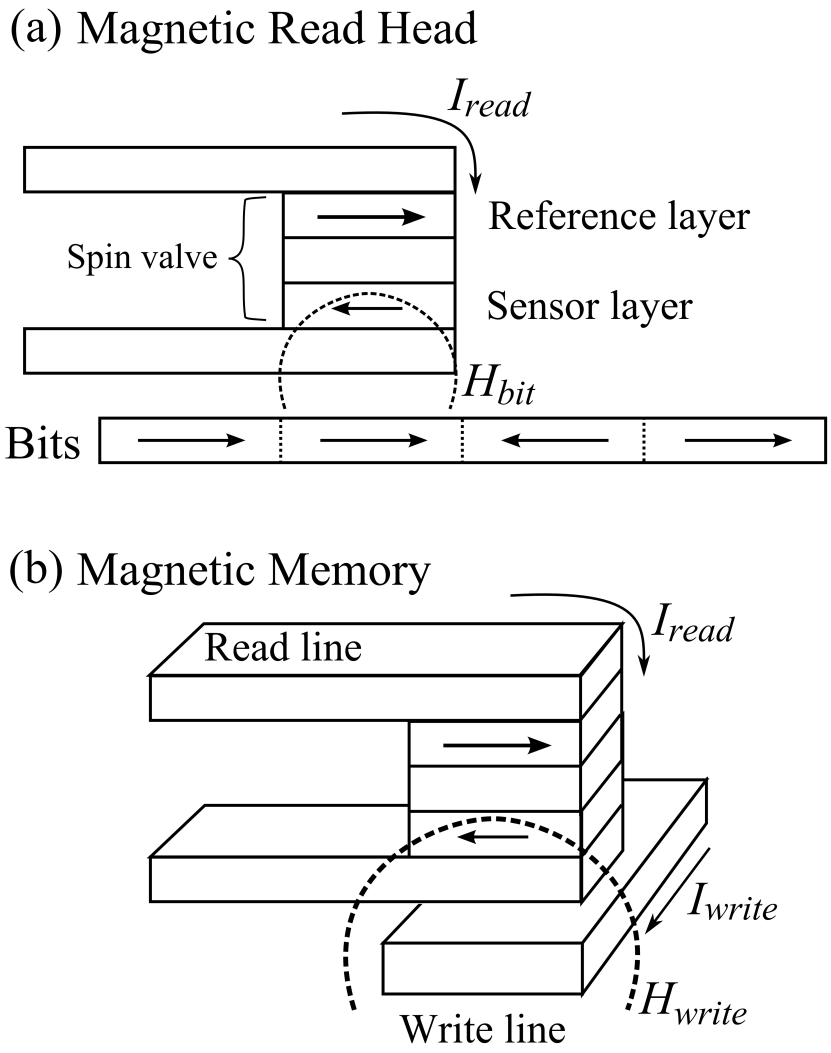

Figure 1.12: (a) Schematic of a magnetic read head, where a current, I_{read}, passing through the spin valve is used to probe the state of bits in a magnetic storage medium. H_{bit} is the magnetic field corresponding to a bit. Panel (b) depicts a magnetic memory cell, where the state of the spin valve is controlled by the magnetic field, H_{write}, generated by a current, I_{write}, passed through a write line.

of the sensor layer rather than bits in a magnetic storage medium. By reversing the direction of the current in the write line, I_{write}, the polarity of the associated magnetic field, H_{write}, is reversed. Accordingly, the spin valve is set to either a low or high resistance state by controlling the current direction in the write line, and the state is probed using I_{read}.

For the spin valves discussed thus far (i.e. GMR based spin valves) the current passes through the entire device, as shown in Figure 1.13(a), and the magnetic dependent operation originates from local spin-scattering of conduction electrons. A class of spin valves that operate under a different physical basis are non-local spin valves (NLSV's) [36, 41–43], which have the geometry shown in Figure 1.13(b), where it can be seen that they consist of a non-magnetic channel (N) connecting two ferromagnetic regions (F_1 and F_2). Contrary to GMR based spin valves where the non-magnetic layer is several nanometers thick, the non-magnetic portion of NLSV's is more akin to a wire, which can be as long as $\sim 10^2$ nm. NLSV's function due to spin-accumulation at the ferromagnetic/non-magnetic interfaces, and the principles of its operation can be deduced from the band structures of the layers, which are shown in the lower half of Figure 1.13(b). In a NLSV, a current is passed through F_1 and N, and the voltage, V, between F_2 and N depends on the relative magnetizations of F_1 and F_2. When the current is passed from F_1 to N, a non-equilibrium magnetization is built up due spin accumulation, as discussed in the previous Section [Equation (1.45)]. While the current only flows in one direction away from N, the spins diffuse in both directions [41], and F_2 serves as a detector to probe the spin accumulation. When the magnetization of F_2 is parallel to the magnetization of F_1, the Fermi level in F_2 aligns with the upper Fermi level in N and the voltage is high. In the antiparallel configuration, the Fermi level in F_2 aligns with the lower Fermi level in N and the

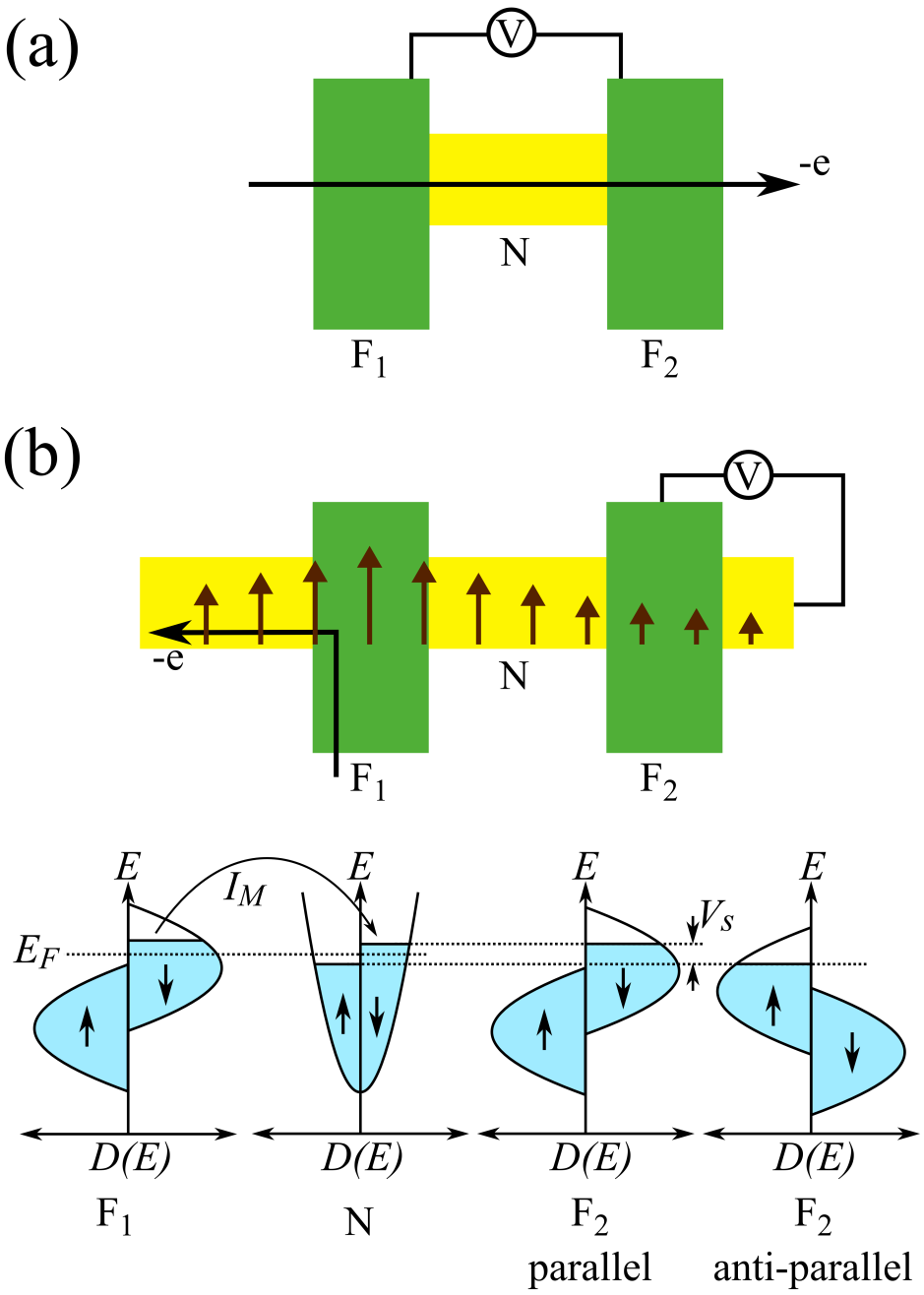

Figure 1.13: (a) Simplified schematic of a GMR based spin valve, where the current is passed through the entire device and the voltage across the device is probed. The upper portion of (b) depicts a non-local spin valve (NLSV), where the current passes through only one ferromagnetic layer (F1), and the voltage between the non-magnetic channel (N) and the other ferromagnetic layer (F2) is probed. The lower portion of (b) depicts the band structure characteristics of the different regions of the NLSV. I_m is the magnetization current injected from F1 to N, and V_s is the difference between the Fermi levels in F2 for the parallel and antiparallel states.

voltage is low. Since the resistance is given by $R = V/I_{probe}$, where I_{probe} is the current passed through F_2, it is apparent that the parallel configuration leads to a high resistance state while the antiparallel configuration leads to a high resistance state. Interestingly, this behaviour is opposite to that observed in GRM based spin valves.

1.4 Chapter 1 References

[1] N. Engheta and R. W. Ziolkowski, *Metamaterials: Physics and Engineering Explorations*. New York: IEEE and Wiley, 2006.

[2] R. A. Shelby, D. R. Smith, and S. Shultz, "Experimental verification of negative refraction," *Science*, vol. 292, pp. 77–79, 2001.

[3] D. Schurig, J. J. Mock, B. J. Justice, S. A. Cummer, J. B. Pendry, A. F. Starr, and D. R. Smith, "Metamaterial electromagnetic cloak at microwave frequencies," *Science*, vol. 314, pp. 977–980, 2006.

[4] N. I. Landy, S. Sajuyigbe, J. J. Mock, D. R. Smith, and W. J. Padilla, "Perfect metamaterial absorber," *Phys. Rev. Lett.*, vol. 100, no. 207402, 2008.

[5] I. I. Smolyaninov, Y. J. Hung, and C. C. Davis, "Magnifying superlens in the visible frequency range," *Science*, vol. 315, pp. 1699–1701, 2007.

[6] G. Dolling, C. Enkrich, M. Wegener, C. M. Soukoulis, and S. Linden, "Simultaneous negative phase and group velocity of light in a metamaterial," *Science*, vol. 312, pp. 892–894, 2006.

[7] N. Engheta, "Circuits with light at nanoscales: Optical nanocircuits inspired by metamaterials," *Science*, vol. 317, pp. 1698–1702, 2009.

[8] S. A. Maier and H. A. Atwater, "Plasmonics: Localization and guiding of electromagnetic energy in metal/dielectric structures," *J. Appl. Phys.*, vol. 98, no. 011101, 2005.

[9] K. J. Chau, M. C. Quong, and A. Y. Elezzabi, "Terahertz time-domain investigation of axial optical activity from a sub-wavelength helix," *Opt. Express*, vol. 15, pp. 3557–3567, 2007.

[10] M. van Exter and D. Grischkowsky, "Carrier dynamics of electrons and holes in moderately doped silicon," *Phys. Rev. B*, vol. 41, pp. 12 140–12 149, 1990.

[11] E. Knoesel, M. Bonn, Shan, and T. F. Heinz, "Charge transport and carrier dynamics in liquids probed by thz time-domain spectroscopy," *Phys. Rev. Lett.*, vol. 86, pp. 340–343, 2001.

[12] K. L. Nguyen, T. Friscic, G. M. Day, L. F. Gladden, and W. Jones, "Terahertz time-domain spectroscopy and the quantitative monitoring of mechanochemical cocrystal formation," *Nat. Mater.*, vol. 6, pp. 206–209, 2007.

[13] M. A. Ordal, "Optical properties of fourteen metals in the infrared and far infrared: Al, Co, Cu, Au, Fe, Pb, Mo, Ni, Pd, Pt, Ag, Ti, V, and W." *Appl. Opt.*, vol. 24, pp. 4493–4499, 1985.

[14] P. B. Johnson and R. W. Christy, "Optical constants of noble metals," *Phys. Rev. B*, vol. 6, pp. 4370–4379, 1972.

[15] K. Wang and D. M. Mittleman, "Metal wires for terahertz wave guiding," *Nature*, vol. 432, pp. 376–379, 2004.

[16] W. Zhu, A. Agrawal, and A. Nahata, "Planar plasmonic terahertz guided-wave devices," *Opt. Express*, vol. 16, pp. 6216–6226, 2008.

[17] K. J. Chau, G. D. Dice, and A. Y. Elezzabi, "Coherent plasmonic en-

hanced terahertz transmission through random metallic media," *Phys. Rev. Lett.*, vol. 94, no. 173904, 2005.

[18] K. J. Chau and A. Y. Elezzabi, "Terahertz transmission through ensembles of subwavelength-size metallic particles," *Phys. Rev. B*, vol. 72, no. 075110, 2005.

[19] A. Y. Elezzabi, K. J. Chau, C. A. Baron, and P. Maraghechi, "A plasmonic random composite with atypical refractive index," *Opt. Express*, vol. 17, pp. 1016–1022, 2009.

[20] A. V. Krasavin and N. I. Zheludev, "Active plasmonics: Controlling signals in auga waveguide using nanoscale structural transformations," *Appl. Phys. Lett.*, vol. 84, pp. 1416–1418, 2004.

[21] K. F. MacDonald, Z. L. Samson, M. I. Stockman, and N. I. Zheludev, "Ultrafast active plasmonics," *Nat. Photonics*, vol. 3, pp. 55–58, 2009.

[22] K. J. Chau and A. Y. Elezzabi, "Photonic anisotropic magnetoresistance in dense co particle ensembles," *Phys. Rev. Lett.*, vol. 96, no. 033903, 2006.

[23] K. J. Chau, C. A. Baron, and A. Y. Elezzabi, "Isotropic photonic magnetoresistance," *Appl. Phys. Lett.*, vol. 90, no. 121122, 2007.

[24] K. J. Chau, M. Johnson, and A. Y. Elezzabi, "Electron-spin-dependent terahertz light transport in spintronic-plasmonic media," *Phys. Rev. Lett.*, vol. 98, no. 133901, 2007.

[25] D. J. Griffiths, *Introduction to Electrodynamics*, 3rd ed. New Jersey: Prentice Hall, 1999.

[26] S. A. Maier, *Plasmonics: Fundamentals and Applications*, 1st ed. New York: Springer, 2007.

[27] C. Kittel, *Introduction to Solid State Physics*, 8th ed. Wiley, 2005.

[28] N. W. Ashcroft and N. D. Mermin, *Solid State Physics*. Philadelphia: Saunders College, 1976.

[29] E. Hirota, H. Sakakima, and K. Inomata, *Giant Magneto-Resistance Devices*. Berlin Heidelberg: Springer-Verlag, 2002.

[30] J. N. Gollub, D. R. Smith, D. C. Vier, T. Perram, and J. J. Mock, "Experimental characterization of magnetic surface plasmons on metamaterials with negative permeability," *Phys. Rev. B*, vol. 71, no. 195402, 2005.

[31] J. B. Pendry, L. Martin-Moreno, and F. J. Garcia-Vidal, "Mimicking surface plasmons with structured surfaces," *Science*, vol. 305, pp. 847–848, 2004.

[32] K. J. Chau, K. M. Rieckmann, and A. Y. Elezzabi, "Subsurface probing of terahertz particle plasmons," *Appl. Phys. Lett.*, vol. 90, no. 131114, 2007.

[33] N. Ashby, "Relaxation of charge imbalances in conductors," *Am. J. Phys.*, vol. 43, pp. 553–555, 1975.

[34] D. A. G. Bruggeman, "Berechnung verschiedener physickalischer konstanten von heterogenen substanzen. i. dielektrizitatskonstanten und leitfahigkeiten der mischkorper aus isotropen substanzen," *Annalen der Physik*, vol. 24, pp. 636–664, 1935.

[35] T. R. McGuire and R. I. Potter, "Anisotropic magnetoresistance in ferromagnetic 3d alloys," *IEEE Trans. Magn.*, vol. 11, pp. 1018–1038, 1975.

[36] M. Johnson, "Spin polarization of gold films via transported," *J. Appl. Phys.*, vol. 75, pp. 6714–6719, 1994.

[37] M. Johnson and R. H. Silsbee, "Interfacial charge-spin coupling: Injection and detection of spin magnetization in metals," *Phys. Rev. Lett.*, vol. 55, pp. 1790–1793, 1985.

[38] ——, "Spin-injection experiment," *Phys. Rev. B*, vol. 37, pp. 5326–5335, 1988.

[39] A. Scholl, F. Nolting, J. Stohr, T. Regan, J. Luning, J. W. Seo, J.-P. Locquet, J. Fompeyrine, S. Anders, H. Ohldag, and H. A. Padmore, "Exploring the microscopic origin of exchange bias with photoelectron emission microscopy," *J. Appl. Phys.*, vol. 89, pp. 7266–7268, 2001.

[40] A. Scholl, M. Liberati, E. Arenholz, H. Ohldag, and J. Stohr, "Creation of an antiferromagnetic exchange spring," *Phys. Rev. Lett.*, vol. 92, no. 247201, 2004.

[41] Y. Ji, A. Hoffmann, J. S. Jiang, J. E. Pearson, and S. D. Bader, "Nonlocal spin injection in lateral spin valves," *J. Phys. D Appl. Phys.*, vol. 40, pp. 1280–1284, 2007.

[42] T. Kimura and Y. Otani, "Large spin accumulation in a permalloy-silver lateral spin valve," *Phys. Rev. Lett.*, vol. 99, no. 196604, 2007.

[43] J. Ku, J. Chang, S. Han, J. G. Ha, and J. Eom, "Spin injection in NiFe/Au/NiFe spin valves," *J. Magn. Magn. Mater.*, vol. 304, pp. e273–e275, 2006.

Chapter 2

Experimental Setup

2.1 Motivation

Over the past decade, terahertz time-domain spectroscopy (THz-TDS) has become a standard technique for investigations into the interactions between electromagnetic radiation and matter [1]. The appeal of THz-TDS stems from several favorable attributes, including the ability to temporally map a THz electric field waveform with sub-picosecond resolution, the large bandwidth of THz pulses, and the ease to create structures with feature sizes comparable to or smaller than the wavelength (300 µm at 1 THz). Accordingly, THz-TDS has been implemented in numerous applications, including optical parameter measurements [2, 3], plasmonics [4, 5], and metamaterials [6, 7]. Moreover, THz-TDS detection techniques are sensitive to the polarization and, with proper implementation, permit the complete characterization of the polarization state of the measured THz signals without the need of additional optical components [8, 9]. As such, THz-TDS has been implemented to study various polarization dependent phenomena, such as chirality [10] and birefringence [11]. In addition to the aforementioned academic interest in THz-TDS, the technology is finding application in next generation imaging modalities due to the large penetration depth of THz radiation and the ability to use commonly available optical components to direct it [12].

A simplified schematic highlighting the sample interaction portion of an on-axis THz-TDS system is portrayed in Fig. 2.1, where a set of parabolic

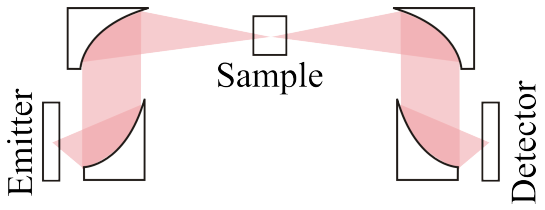

Figure 2.1: Schematic of a typical THz-TDS system, where 4 parabolic mirrors control the propagation of the radiation.

mirrors collimate then refocuses the radiation onto the sample, and a second set of parabolic mirrors focus the radiation onto the detector for measurement. Since a portion of the THz artificial materials investigated in this thesis have angular dependent operation, such a static configuration is not desirable. Rather, a THz-TDS system capable of detecting radiation scattered in arbitrary directions is desired. The realization of this goal is non-trivial, though, as evidenced by the small number of reported systems demonstrating such capabilities. Perhaps the most straight forward solution is to mount the components located after the radiation interacts with the sample on an arm that can be rotated, as demonstrated in [13] and [14]. The limitation of such an approach is that the parabolic mirrors used to direct the THz radiation require a significant amount of space, precluding access to the detection positions where the parabolic mirrors would obstruct each other. Moreover, the detection modality utilized in [13] and [14] is photoconductive (PC) detection as opposed to electro-optic (EO) detection. The latter detection scheme has several advantages over the former, which will be discussed in the following section. As such, before the completion of the work presented in this thesis, no THz-TDS system providing access to the full range of positions around the sample had been revealed. Accordingly, this chapter introduces a new THz-TDS system with such capabilities and provides experimental results that verify its functionality.[1]

2.2 Generation and Detection of Terahertz Pulses

The realization of a THz-TDS system involves the combination of three primary building blocks: THz generation, interaction with the sample, and mea-

[1] The results of this Chapter have been published in *Measurement Science and Technology*, "A 360° angularly ranging time-domain terahertz spectroscopy system," vol. 19, 065602, 2008.

surement of the scattered or transmitted THz radiation. For THz radiation generation, the most widely implemented method is the excitation of a PC emitter with ultrashort optical "pump" pulses [1]. A typical PC-emitter consists of a pair coplanar transmission lines fabricated on a semi-insulating (SI) GaAs, as shown in Figure 2.2(a). A DC bias, V_B, is applied to the transmission lines, which establishes an electric field, E_B, between them. Due to the high dark resistivity of SI-GaAs ($\sim 10^7 \Omega$ cm [15]), current does not flow and the bias is maintained at its nominal value. When the pump pulse is incident on the PC gap, electrons and holes are liberated from the valence band into the conduction band and are quickly accelerated by E_B. Thus, this burst of electron acceleration results in the emission of THz radiation. Using a typical pump fluence and DC bias, a dual lobe THz pulse akin to the one depicted in Figure 2.2(a) and having a typical duration $\sim$ 1 ps is generated. The bandwidth for such pulses is typically $\sim$ 1 THz. The initial positive lobe results from the initial acceleration of the electrons and holes. However, the space-charge distribution that results from the movement of the electrons and holes leads to the creation of an associated electric field, E_{charge}, that is in the opposite polarity to E_B, which reduces the photo-induced current. The deceleration of electrons and holes associated with this is the mechanism responsible for the negative lobe in the THz pulse [16]. At low pump pulse powers and low E_B the THz emission strength scales with the pump power and V_B; however, the possible emission strengths are limited by saturation for high pump pulse powers [17] and the breakdown of the semiconductor via avalanche across the photoconductive gap with extremely high biasing fields.

In order to measure the THz radiation, femtosecond "probe" pulses are utilized to sample the electric field strength of the THz pulses. Since the duration of the probe pulses ($\sim 10-20$ fs) are three orders of magnitude shorter

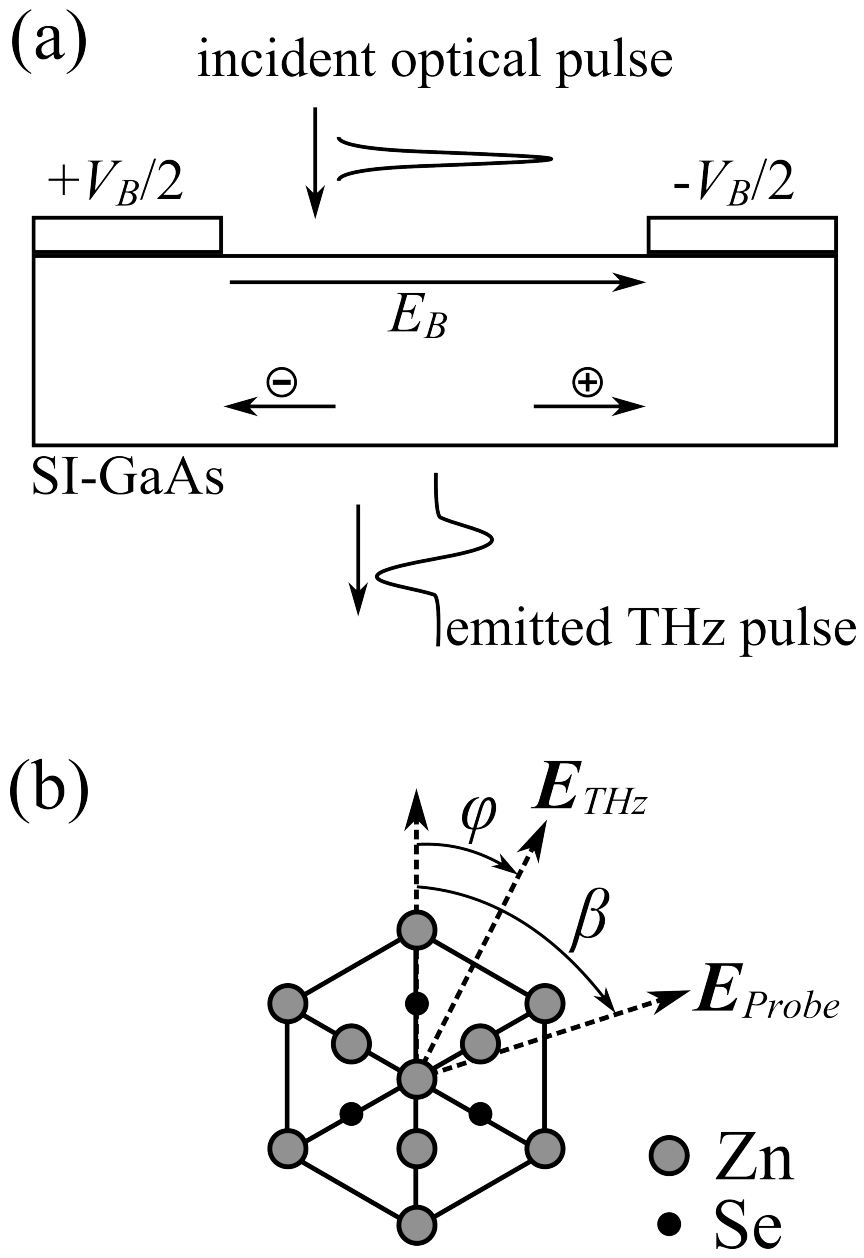

Figure 2.2: (a) An illustration of the generation of freely propagating THz pulses via the illumination of a PC gap with above band gap radiation. The ultrashort optical pulse excites electrons and holes into the conduction band, which are accelerated by the bias electric field, E_B, and radiate THz electric field into the far-field. Panel (b) depicts the coordinate geometry for EO detection, where the polarizations of the THz and probe pulses are at angles of φ and β with respect to the azimuthal orientation of the $\langle 111 \rangle$ ZnSe EO crystal. The propagation direction of the THz and probe pulses are perpendicular to the page.

than the THz pulses, they provide effectively instantaneous measurements of the THz electric field. As such, the entire THz pulse is characterized by using a delay line to vary the position of the probe pulses relative to the THz pulses. There are two methods that are commonly used to implement the sampling: PC detection and EO detection. PC detection is essentially the inverse of PC emission. Here, the PC gap is not externally biased; rather, the THz electric field serves as the bias field. As such, when photo-carriers are excited into the conduction band by the probe pulse, they are accelerated by the THz electric field. The corresponding current, which is proportional to the THz electric field strength, is then measured using a low-noise current amplifier. PC semiconductor materials having very short carrier lifetimes are typically utilized to maximize the temporal resolution.

In EO detection, the THz pulse and optical probe pulse co-propagate in an EO crystal. Here, the THz electric field modulates the index ellipsoid of the EO crystal via the Pockels effect. This THz induced birefringence results in a polarization rotation of the probe pulse polarization. To measure this, a quarter-wave plate converts the probe pulse to a circular polarization, and a Wollaston prism converts the probe pulse into two separate, orthogonally polarized signals. Finally, balanced diode detectors measure the difference in intensity, ΔP, between the two orthogonally polarized pulses, where the differential intensity is proportional to the THz electric field. Because this technique is non-resonant, the temporal resolution is limited only by the length of the probe pulse ($\sim$ 10 fs). Since the non-linear response of materials is highly dependent on the orientation of the electromagnetic fields with the crystal axes, ΔP is dependent on the probe pulse polarization and THz electric field polarization relative to the EO crystal orientation. EO crystals that are commonly utilized for THz detection are ZnTe and ZnSe due to reasonably

high nonlinear EO coefficients and low velocity mismatch between the THz pulse and optical probe pulse. For the work presented in this thesis, a $\langle 111 \rangle$ ZnSe crystal is utilized, which has ΔP given by [18]

$$\Delta P \propto E_{THz} \sin(2\beta + \varphi) \tag{2.1}$$

where E_{THz} is the amplitude of the THz electric field, β is the polarization angle of the probe pulse with respect to the azimuthal EO crystal orientation, and φ is the polarization angle of the THz electric field with respect to the azimuthal EO crystal orientation [Figure 2.2(b)]. Typically the probe pulse polarization is aligned parallel to the THz electric field polarization, yielding a $\sin(3\varphi)$ dependence in Equation (2.1). As such, perpendicular polarization states of the THz radiation can be measured by re-orienting the EO crystal by 30°. This ease of polarization sensitivity constitutes an advantage of EO detection over PC detection. In PC detection the perpendicular polarization can be measured by rotating the PC gap by 90°; however, this is technically challenging due to the sensitive alignment requirements of PC detection.

2.3 System Specifications

Design schematics of the THz-TDS system implemented in the thesis work are depicted in Figure 2.3. To prevent the detection components from interfering with the generation of THz pulses for detection angles spanning 360°, the detection portion of the system is positioned on a rotatable platform 152 mm directly above the generation portion. A periscope mirror arrangement directs the THz radiation scattered from the sample to the upper platform. Since the sample is positioned on the axis of rotation of the upper platform, the detection portion of the system is free to rotate around the sample without compromising

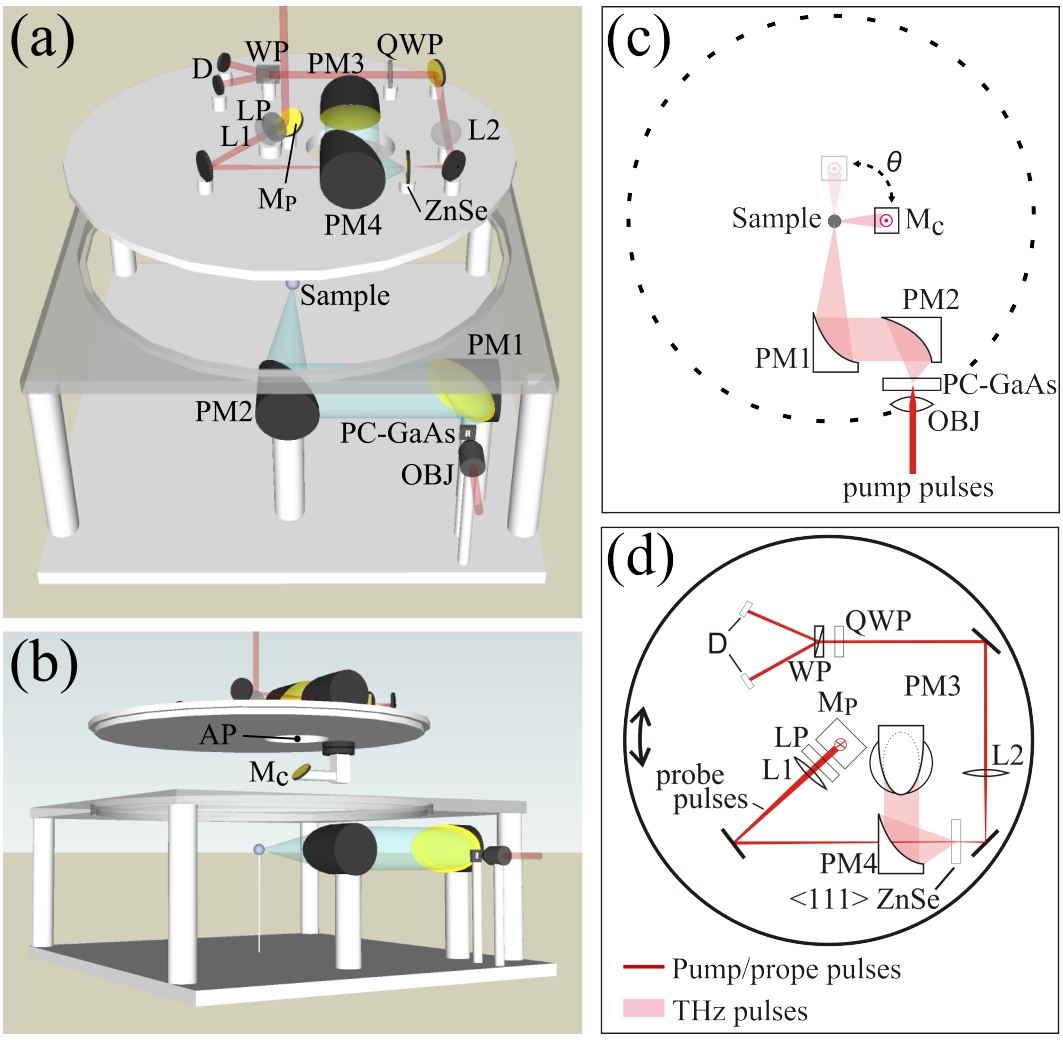

Figure 2.3: (a) A three-dimensional representation of the THz spectroscopy system. Panel (b) depicts the location of the mirror, M_C, which directs the scattered THz radiation to the detection optics, and the location of an optional aperture, AP, which can be adjusted to vary the angular resolution of the system. A 2D representation of the THz spectroscopy system is shown in panels (c) and (d). The platform depicted in panel (b) is located 152 mm above the platform depicted in panel (a). PC-GaAs is a semi-insulated GaAs photoconductive switch, M_C and M_P are planar mirrors, PM1PM4 are parabolic mirrors, OBJ is a microscope objective, L1 and L2 are biconvex lenses, LP is a linear polarizer, QWP is a quarter-wave plate, WP is a Wollaston prism and D are balanced diode detectors. The upper platform is free to be rotated to any angle, θ, from the on-axis detection position.

neither temporal synchronization nor spatial alignment of the THz pulses. The rotatable platform is constructed from a 13 mm thick, 381 mm diameter aluminum circular plate that is mounted on a 406 mm wide square support structure using complimentary L-shaped bevels [Figure 2.3(a,b)]. A thin layer of Teflon is located between the platform and support structure to permit smooth rotation, and the well-fitting bevels result in negligible translational movement.

THz electromagnetic pulses are generated by focusing 12 fs, 800 nm pump pulses from a Ti:sapphire laser onto a semi-insulated GaAs photoconductive switch (PC-GaAs) using a 10:1 objective (OBJ) with a numerical aperture of 0.30. The emitted THz radiation has a linear polarization direction that can be adjusted via rotation of the photoconductive switch and, for the experimental realization utilized here, the polarization is aligned parallel to the lower platform. A parabolic mirror (PM1; Janos Technology part A8037-295) having a diameter and focal length of 50 mm collimates the THz radiation emitted from the PC-GaAs THz source and directs it towards 50 mm diameter parabolic mirror (PM2; Janos Technology part A8037-206) having a focal length of 152 mm. The focal length of PM1 is relatively short to maximize its acceptance angle which, in turn, enhances the total pulse energy. PM2 focuses the THz pulses onto the sample, which is positioned on the axis of rotation of the upper platform so that radiation that is scattered from the sample at any angle will travel the same distance before reaching the subsequent mirror, M_C. M_C is a planar, 25.4 mm diameter mirror that collects the THz radiation scattered from or transmitted through the sample. Since it is attached to the rotatable platform, it can be positioned to any angle, θ, around the sample, where $\theta = 0^\circ$ corresponds to on-axis detection, as shown in Figure 2.3(c). To ensure that alignment is maintained for all detection angles, all of the subse-

quent optical components must rotate with M_C and, as such, are located on the rotatable platform.

While M_C can effectively collect the radiation scattered to most angles, it is clear from Figure 2.3(c) that for the measurement of back-scattered radiation (i.e. $\theta = 180°$), M_C would block the incident radiation. As such, in this situation M_C is replaced with a beam splitter which allows a portion of the incident radiation to pass through. However, this type of configuration results in the loss of at least 75% of the signal strength compared to when M_C is used. The interchanging of M_C and the beam splitter is performed by mounting each onto top plates of a switchable magnetic kinematic base (Thorlabs part# SB1), and having a bottom plate that remains fixed on the underside of the rotatable platform. The top and bottom plates are fastened together magnetically, and allow for exact replacement of either element.

Since mirror PM2 focuses the THz radiation onto the sample, the radiation is diverging after leaving M_C and, accordingly, is collimated once again by PM3, a 152 mm focal length parabolic mirror identical to PM2. A 76 mm diameter hole followed by a variable aperture (AP) allows the radiation collected by M_C to pass through the rotatable platform and reach PM3. M_C is located 52 mm from the sample and 100 mm below PM3, and AP is located 66 mm below PM3. AP is present to grant control over the angular resolution of the system since it limits the solid angle subtended by the diverging THz radiation propagates away from the sample. AP diameters ranging from 3 mm to 23 mm correspond to angular resolutions ranging from 2° to 15°, and complete removal of AP causes the solid angle to be constrained by PM3,[2] yielding an angular resolution of 19°. It is critical to note that improving the angular resolution via AP results in a concomitant decrease in the amplitude

[2]The solid angle is not constrained by M_C due to the relatively small transverse size of the THz beam at its location, which can be inferred through ray tracing.

of measured signals, and the trade-off between resolution and signal strength must be considered. After being collimated by PM3, the THz radiation is focused onto a 1 mm thick ⟨111⟩ ZnSe EO crystal by a 50 mm focal length parabolic mirror, PM4.

To electro-optically sample the THz radiation, 12 fs duration, 800 nm probe pulses must be aligned to co-propagate with the THz pulse in the EO crystal which, given that the EO crystal moves with the rotatable platform, is non-trivial. To ensure that the optical path length (i.e. temporal synchronization of the probe pulses with the THz pulses in the EO crystal) and the spatial alignment of the probe pulses are consistent for all θ, they are directed to the rotatable platform from above along the platform's axis of rotation. A planar mirror, M_P, directs the probe pulses such that they propagate parallel to the rotatable platform. To avoid rotation of the polarization of the probe pulse when rotating the platform to various θ, the probe pulses are circularly polarized using a quarter-wave plate before contact with M_P. Immediately after contact with M_P, the probe pulses pass through a linear polarizer, LP, to extract a linear polarization. Such precautions are required due to the dependence of the EO response on the probe polarization [Equation (2.1)]. Therefore, by using this prescribed configuration, the optical path length, alignment, and polarization of the probe pulses are consistent relative to the optics located on the rotatable platform for any θ. To accommodate co-propagation of the probe pulses with the THz pulses in the EO crystal, the probe pulses are focused by lens L1 through a small, 1.5 mm hole that passes through PM4 such that the focal point lies inside the EO crystal. The hole in PM4 has an area that represents less than 1% of the total area of PM4 and, thus, any THz signal loss resulting from the hole is negligible. The focal length of L1 is chosen to be relatively large (250 mm) to minimize the transverse size of the probe

pulses as they pass through the hole in PM4. After passing through the EO crystal, the probe pulse is collimated by a 100 mm focal length lens (L2) then converted to a circular polarization by a quarter-wave plate (QWP). A Wollaston prism (WP) converts the probe pulse into two separate, orthogonally polarized signals, and balanced diode detectors (D) measure the difference in intensity between them. Since the probe pulse only samples a single 12 fs wide portion of the THz pulse, a delay line is used to systematically vary the relative temporal positions between the THz pulse and probe pulse and, thus, retrieve the electric field profile of the entire THz pulse.

While the sample and THz focal spot are ideally both located at the axis of rotation of the upper platform to ensure that the temporal locations of THz pulses are consistent for any θ, it is possible to correct for an off-center THz focal spot with the knowledge of the focal spot position. To accurately determine the focal spot position with respect to the axis of rotation, a sample that scatters THz radiation symmetrically to positive and negative θ can be placed in the center of the THz focal spot, as shown in Figure 2.4. Here, the

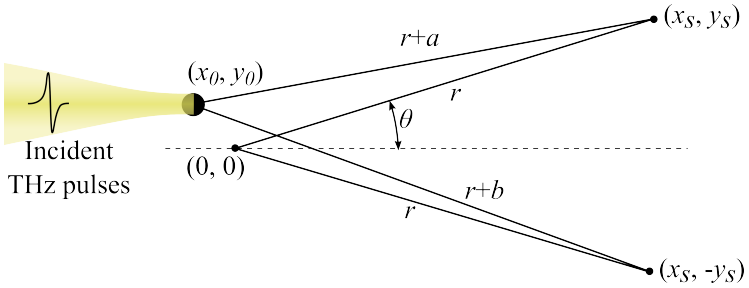

Figure 2.4: Schematic of a sample that is positioned slightly away from the axis of rotation of the rotatable platform. The sample is indicated by the black circle, the origin $(0, 0)$ is set at the axis of rotation, the sample is located at (x_0, y_0) and two symmetric detector locations are located at (x_s, y_s) and $(x_s, -y_s)$.

THz focal spot and sample are positioned at (x_0, y_0) while the axis of rotation of the platform is located at $(0, 0)$. The difference in arrival times, Δt, between

THz pulses measured at symmetric detector locations (x_s, y_s) and $(x_s, -y_s)$ is given by

$$\begin{aligned}\Delta t &= c(a-b) \\ &= c\left(\sqrt{(x_s-x_0)^2+(y_s-y_0)^2}-\sqrt{(x_s-x_0)^2+(-y_s-y_0)^2}\right)\end{aligned} \tag{2.2}$$

where the sample-to-P_{pos} and sample-to-P_{neg} distances are $r+a$ and $r+b$, respectively, c is the speed of light, and r is the distance from the axis of rotation to any detector location. x_0 and y_0 are the only unknown parameters in Equation (2.2) and, therefore, by determining Δt for two sets of symmetric detector locations the exact position of the THz focus can be determined.

Now consider the effect of an off-center sample on the amplitude of the measured THz pulses. Here, the sample is considered to be a point-source scatterer and, accordingly, the radiation propagating away from the sample is assumed spherical until collimation by PM3. For two different sample to PM3 distances, d_1 and d_2, the electric field amplitudes at PM3 (E_1 and E_2, respectively, for the two distances) fulfill the relation [19]

$$\frac{d_1}{d_2} = \frac{E_1}{E_2}. \tag{2.3}$$

Since the sample-to-PM3 distance is nominally 152 mm, even a 1 mm deviation of the sample from the axis of rotation of the rotatable platform results in less than a 1% change in the electric field amplitude. As such, even crude alignment of the sample with the axis of rotation of the rotatable platform permits the measurement of reliable THz electric field amplitudes.

To verify the off-axis detection functionality of the system, a sample that is symmetric about the incident THz pulse axis is used. As such, observing whether THz pulses measured at $\pm\theta$ are similar provides an indication of the

consistency of measurements at various θ. Accordingly, a spherical sample can be used as a sample to verify the system functionality. In order to observe the expected scattering pattern from such a sample, a two-dimensional finite-difference time-domain (FDTD) simulation is performed [20]. In the calculation, a dual-cycle 3 ps long THz pulse traveling in the positive z-direction is focused onto a 1.5 mm diameter perfectly metallic sample. The spot size of the incident pulse at the focus is 1.1 mm. As shown in Figure 2.5, the electric field distribution 110 ps after the pulse makes contact with the sample is characterized by a symmetric scattering pattern. It is apparent that the scattered radiation is predominantly traveling towards the $+z$ (on-axis) and $-z$ (back-scattered) directions.

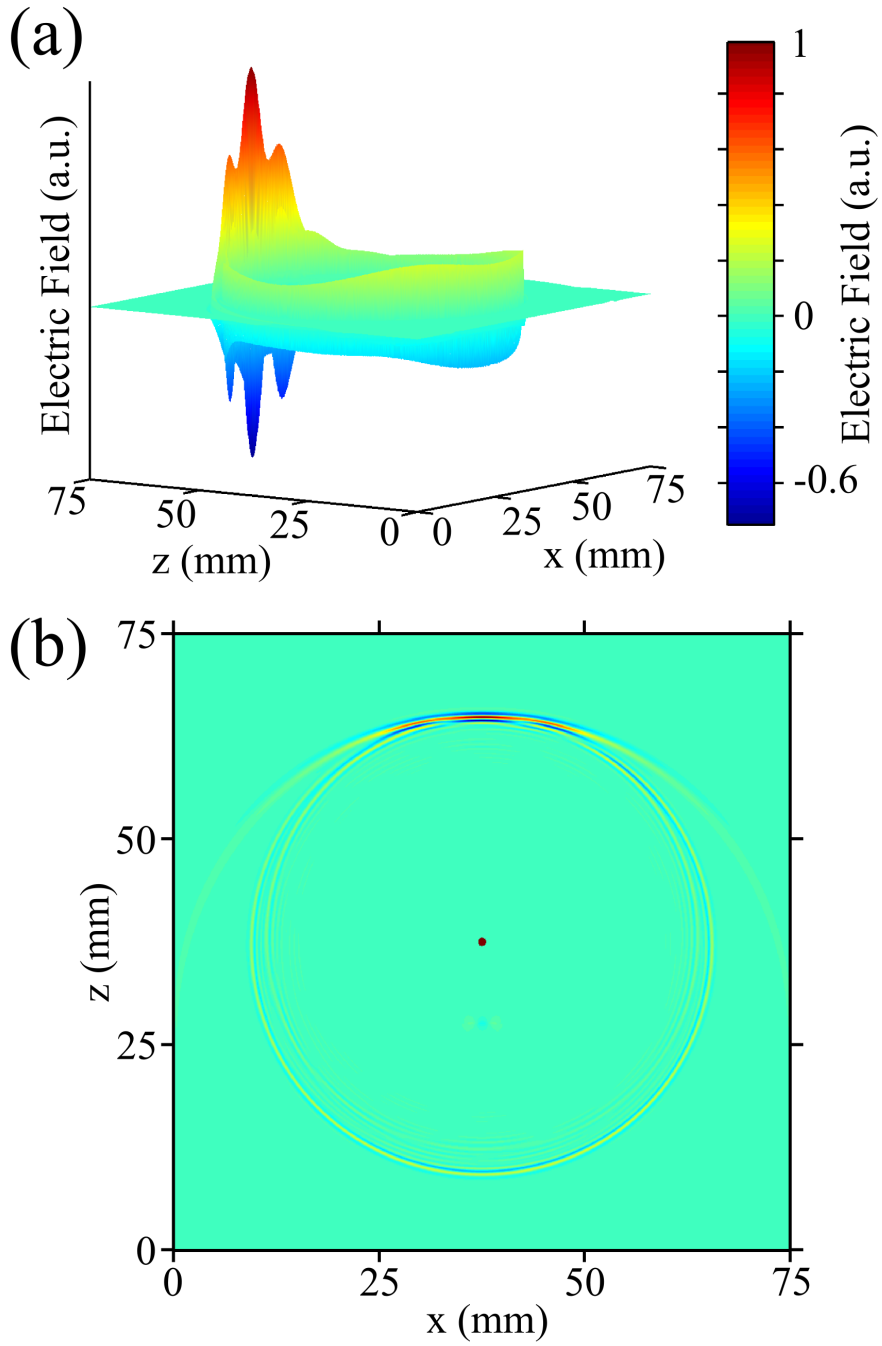

Figure 2.5: Simulation of the electric field pattern 110 ps after the excitation of a 1.5 mm diameter circular metal sample using a 3 ps long THz pulse that is traveling in the $+z$ direction, and focused near the sample. The circle in the center of the plot shown in (b) is the sample.

2.4 Experimental Verification

The time-domain electric field of the THz pulses that travel through free space and are measured at $\theta = 0^\circ$ is shown in Figure 2.6(a). The signal to noise ratio (SNR) is 39 dB, where the calculation of SNR is performed using the average power of the three dominant lobes of the THz pulse. The portion of the waveform prior to the arrival of the pulse is used for the noise in the calculation. The power spectrum of the free space THz pulse, with a bandwidth of 0.32 THz and a center frequency of 0.38 THz, is depicted in Figure 2.6(b). Note that the measured bandwidth may be slightly reduced due to temporal broadening of the THz pulse due to a group velocity mismatch between the probe and THz pulses in the ZnSe EO crystal. The temporal walk-off is 1 ps/mm for single-crystal ZnSe [21] and, if required, the temporal broadening of the THz pulse could be mitigated at the expense of SNR by using a thinner EO crystal. The THz focal spot profile at the sample location is evaluated by measuring the electric field amplitude of the dominant lobe of the transmitted THz pulse while a knife-edge is moved transversely across the THz focal spot. Figure 2.6(c) depicts the intensity of the THz radiation along the THz electric field polarization direction at the focal spot, where a full-width-half-maximum of 1.1 mm is discernible.

As mentioned earlier, when AP is not in place the angular resolution is dictated by PM3. Since PM2 and PM3 are positioned symmetrically about the sample location, when no sample is present the solid angle of the diverging THz radiation that propagates towards PM3 is equal to the angular resolution. Therefore, the angular resolution (without AP in place) is experimentally validated by measuring the THz radiation at various θ, where it is observed that the peak-to-peak electric field strength of the measured waveforms are half the value at $\theta = 0$ when $\theta = 9^\circ \pm 1^\circ$ and $\theta = -9^\circ \pm 1^\circ$, which agrees with

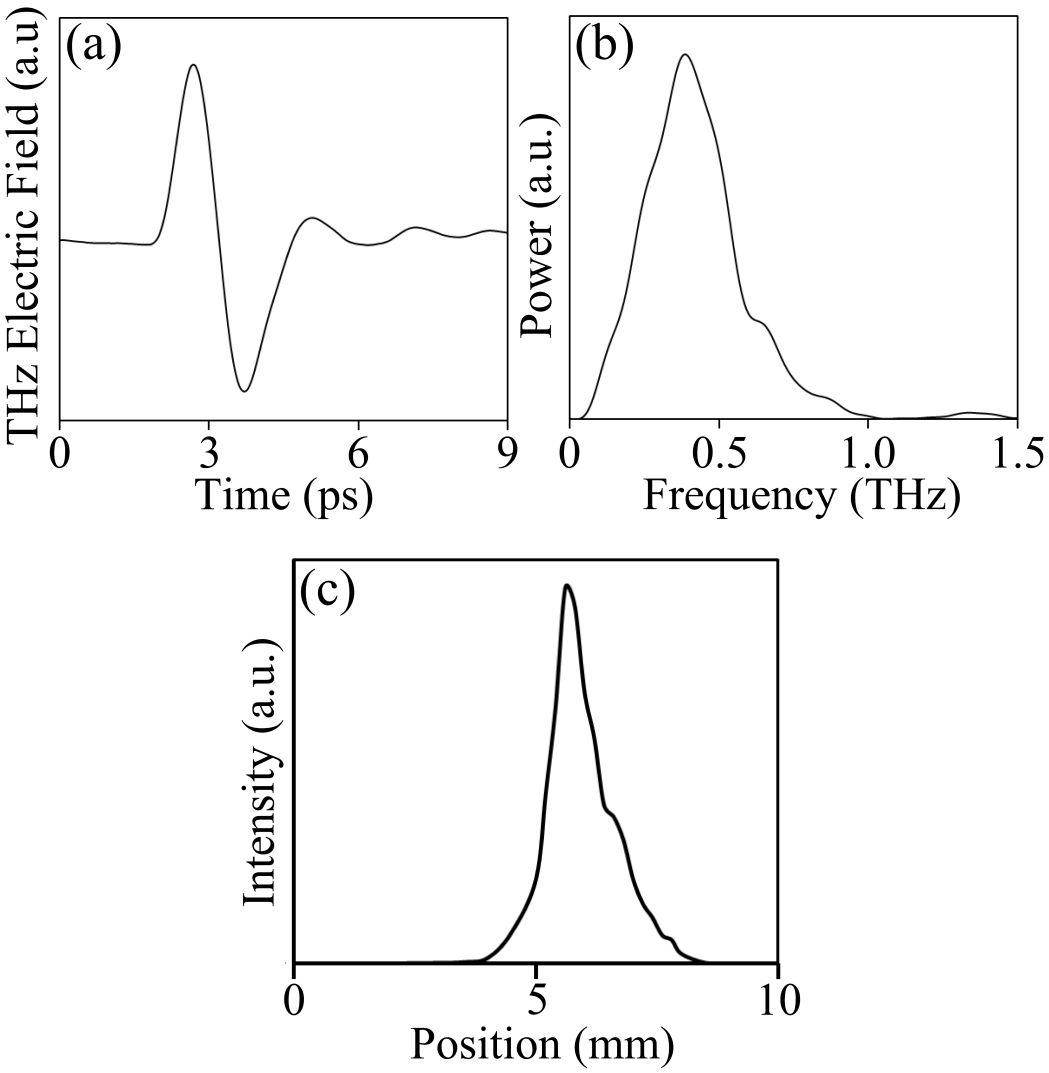

Figure 2.6: (a) Experimentally obtained electric field of the free space THz pulse measured at $\theta = 0°$. Panel (b) depicts the power spectra of the pulse, and panel (c) depicts the intensity, I, of the THz radiation at the focal spot of PM2.

the predicted resolution of 19°. When AP is in place, there exists a trade-off between angular resolution and the amplitude of the detected signals, which is experimentally characterized by measuring the free-space THz pulses at $\theta = 0°$ for AP diameters ranging from 3 mm to 23 mm. To compare the signals for various AP diameters, the time-averaged energy flux, P, is calculated, where

$$P = \frac{\langle E(t) \rangle^2}{\langle E_0(t) \rangle^2}, \tag{2.4}$$

$\langle \ldots \rangle$ denotes temporal averaging, $E(t)$ is the time dependent electric field of the detected THz pulses, and $E_0(t)$ is the electric field when AP is not in place. As shown in Figure 2.7, the energy of the detected THz pulses decreases by 2.5 orders of magnitude when the diameter of AP is decreased from 23 mm to 3 mm, which corresponds to an angular resolution decrease from 15° to 2°. When the diameter of AP is less than 3 mm, the detected THz signals become comparable in amplitude to the noise level. As such, a lower bound of the angular resolution is 2°; however, if one could increase the SNR by other means (e.g. more powerful emitter) it could be possible to overcome this limit.

Analogous to the FDTD calculations, a 1.5 mm diameter steel ball bearing is used as a sample to experimentally verify the off-axis detection functionality of the THz system. The sphere is adhered to a thin plastic sheet that is transparent to THz radiation. As observed in the FDTD calculations, this type of sample scatters the THz radiation in all directions and, accordingly, the signals measured are low in amplitude. Therefore AP is not implemented in an effort to maximize SNR of the measured signals. The time-dependent electric field of the THz pulses measured at $\theta = \pm 150°$ and $\theta = \pm 20°$ are portrayed in Figure 2.8(a) and (b), respectively. Here it can be seen that the THz pulses measured at symmetric θ are very similar, which was also observed

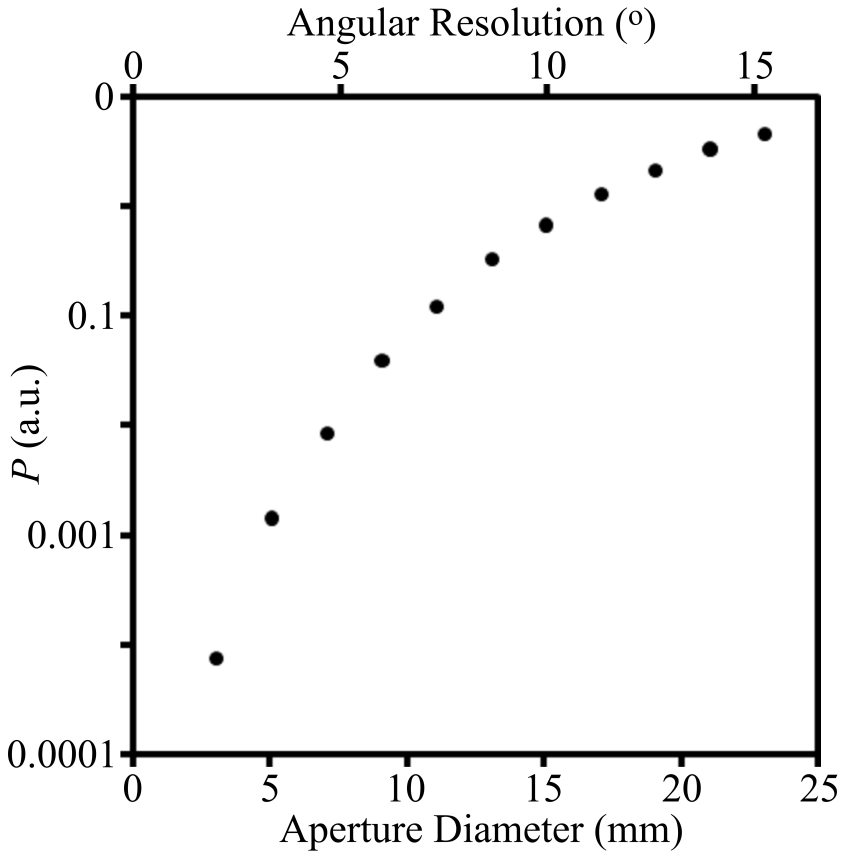

Figure 2.7: Time-averaged energy flux, P, of the on-axis THz pulses measured as the size of the aperture, AP, is decreased from 23 mm to 3 mm. The angular resolutions corresponding to the aperture sizes are also shown.

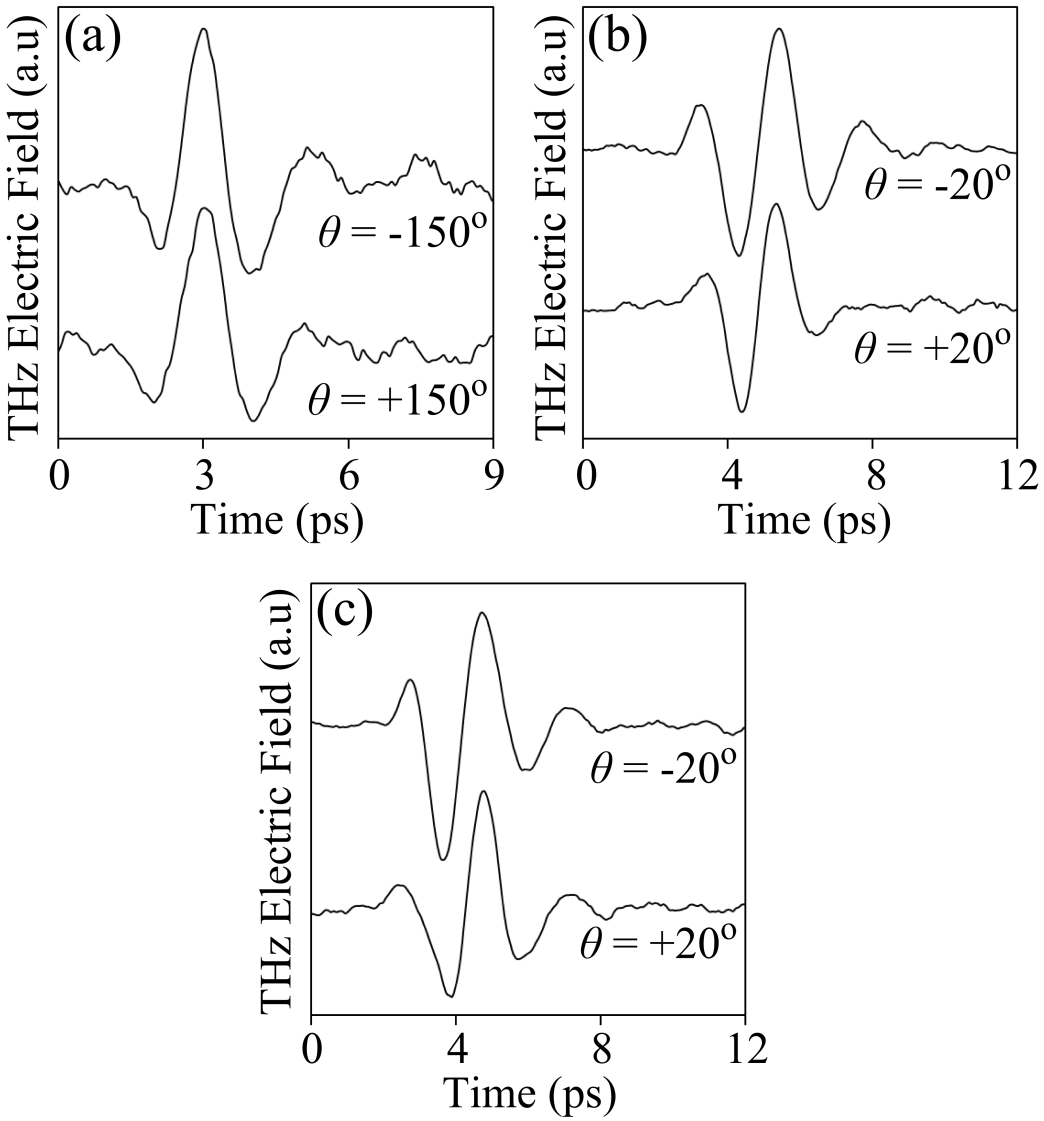

Figure 2.8: Experimental THz electric field measured at detection angles of (a) $\theta = \pm 150°$ and (b) $\theta = \pm 20°$, when THz pulses are focused on to a 1.5 mm spherical sample. After the sample is shifted by 150 µm from the center of the THz focal spot, the THz pulses shown in panel (c) are measured at $\theta = \pm 20°$. The zero times in panels (a) to (c) are not referenced to each other.

for the other angles of detection. It should be noted that while Equation (2.2) was utilized to correct the temporal locations of the pulses detected at symmetric θ, an average time difference of 141 fs is observed between the time-corrected pulses detected at symmetric θ ranging from $\pm 10^\circ$ to $\pm 160^\circ$ in 10° increments. The detection locations $\theta = \pm 90^\circ$ and $\theta = \pm 100^\circ$ were not used in the average due to high noise levels. This uncertainty in arrival times of the pulses likely stems from slight translational movement of the rotating platform, and corresponds to a ± 42 µm uncertainty in the sample to M_C distance.

The sensitivity of the measurements of THz pulses on the sample placement relative to the THz focal spot is investigated by shifting the sample by 150 µm in the direction transverse to the propagation direction. The THz pulses measured at $\theta = \pm 20^\circ$ are depicted in Figure 2.8(c), where it is evident that the pulses become more dissimilar. This is most evident in the lobe located at 4 ps. To quantitatively characterize the degree of symmetry between THz pulses detected at symmetric θ, an symmetry parameter Δ is defined as

$$\Delta = \frac{\langle |E_{+\theta}(t) - E_{-\theta}(t)| \rangle - \langle |E_{\text{noise}}(t)| \rangle}{\max(E_{+\theta}(t), E_{-\theta}(t))} \times 100\% \tag{2.5}$$

where $E_{+\theta}(t)$ and $E_{-\theta}(t)$ are the time-dependent electric field amplitudes for positive and negative θ, respectively, and $E_{\text{noise}}(t)$ is the amplitude of the noise. Accordingly, Δ represents the average difference between the signals. Without the subtraction of $\langle |E_{\text{noise}}(t)| \rangle$, signals having low SNR would have a high Δ even if the signals at symmetric θ agreed within error. For the pulses depicted in Figure 2.8(a) ($\theta = \pm 150^\circ$) and Figure 2.8(b) ($\theta = \pm 20^\circ$), Δ is 4.4% and 8.7%, respectively. After the 150 µm shift in the sample, $\Delta = 11.0\%$ for the THz pulses shown in Figure 2.8(c) ($\theta = \pm 20^\circ$). Considering that the distance the sample was shifted is significanly smaller than the wavelength of

the incident THz pulses (150 µm compared to 800 µm), this system is capable of resolving a subwavelength change in the sample conditions. As such, this THz-TDS system may be useful for studying position-dependent scattering phenomena.

To gain insight into the scattering pattern of the sphere, P is calculated for various θ using Equation (2.4), as shown in Figure 2.9(a). Only positive θ are shown due to the symmetry of the sample, and P for $\theta = 90°$ and $\theta = 100°$ are not included since the signal amplitude is less than the noise level. For $\theta > 160°$, mirror M_C blocks a portion of the incident THz radiation, precluding the calculation of P. To observe the back-scattered pulse, M_C is replaced with a beam splitter and the THz pulse shown in Figure 2.9(b) is measured for $\theta = 180°$. Notably, the value of P for the pulse measured at $\theta = 180°$ is not included in Figure 2.9(a) since the beam splitter is of finite thickness, which results in a slight transverse shift of the incident radiation. As illustrated by the THz pulses shown in 2.8(b) and 2.8(c), the measured THz pulses are sensitive to even extremely small variations in the relative positions of the incident radiation and sample. As such, the change in position of the incident radiation induced by the beam splitter precludes the ability to quantitatively compare the signals measured with the beam splitter in place to those measured with M_C in place. For other samples, though, comparison may be possible provided that the measured THz pulses do not exhibit high sensitivity to sample position. Moreover, this concern could be mediated by implementing a pellicle beam splitter. Nevertheless, it can be observed from Figure 2.9(a) that the THz radiation is predominantly scattered towards $\theta = 0°$ and $\theta = 180°$, with a minimum of radiation scattered in the perpendicular direction towards $\theta = 90°$

One of the advantages of THz-TDS is the ability to easily extract the

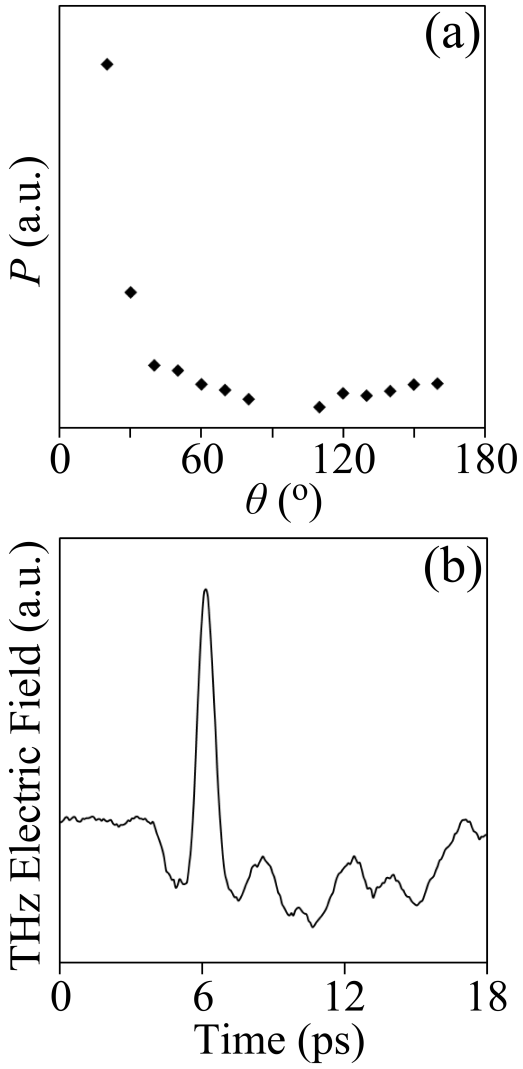

Figure 2.9: (a) The time-averaged energy flux, P, of THz pulses measured at $\theta = 20°$ to 160°. Panel (b) portrays the THz electric field measured at $\theta = 180°$.

polarization information of the measured pulses. With the implementation of EO detection, the electric field strength at various polarization angles is accessed by varying the angle the EO crystal with respect to the THz and probe pulse polarizations, as discussed earlier. For a EO crystal angular position of φ, the THz polarization parallel to that of the THz radiation incident on the sample is accessed by setting $\varphi = m60°$, where n is any integer. The perpendicular polarization is accessed by setting $\varphi = m60° + 30°$. Accordingly, the time-resolved polarization content of the THz pulse measured at $\theta = 0°$ when no sample is in place is depicted in Figure 2.10(a). The polarization content for $\theta = 20°$, and $\theta = 150°$ when the sample is in place are depicted in Figure 2.10(b) and (c), respectively. Here, it is evident that all three pulses are linearly polarized.

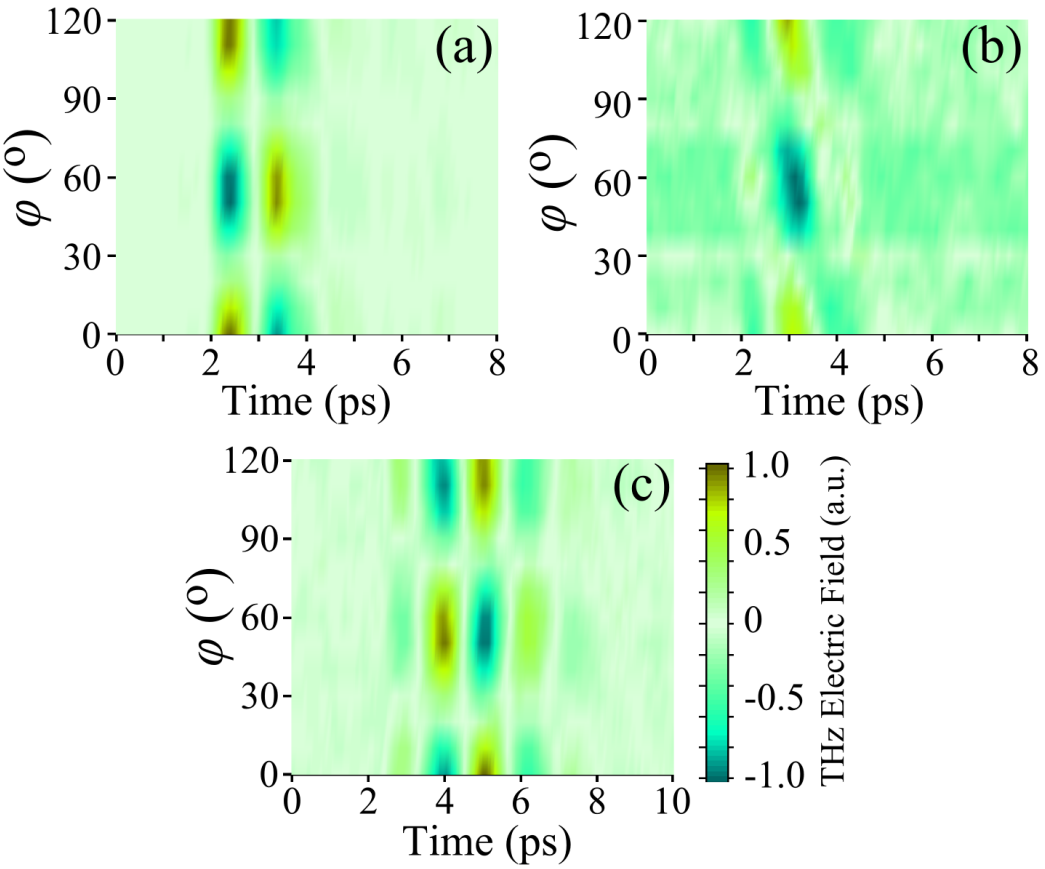

Figure 2.10: Experimental electric field of the free space THz electric field measured as the angle of the ⟨111⟩ ZnSe crystal, φ, is varied from 0° to 120°, at an angle of detection of $\theta = 0°$. When the spherical sample is in place, the THz electric fields depicted in (b) and (c) are measured at $\theta = 20°$ and $\theta = 150°$, respectively. The zero times in the four panels are not referenced to each other, and the color bar corresponds to all three panels.

2.5 Conclusion

THz-TDS provides a powerful platform for electromagnetic investigations due to the ability to measure picosecond long electromagnetic pulses with resolutions on the order of tens of femtoseconds while also extracting the time-dependent polarization information. While conventional THz-TDS systems are static and only measure the radiation scattered or transmitted at a fixed angle, the work presented here introduces a system capable of THz detection at any angle 360° around a sample. The performance of the system is demonstrated experimentally, and the results are qualitatively comparable to predictions obtained from FDTD calculations.

2.6 Chapter 2 References

[1] D. Mittleman, *Sensing with Terahertz Radiation*. Heidelberg: Springer, 2002.

[2] D. Grischkowsky, S. Keiding, M. van Exter, and C. Fattinger, "Far-infrared time-domain spectroscopy with terahertz beams of dielectrics and semiconductors," *J. Opt. Soc. Am. B*, vol. 7, pp. 2006–2015, 1990.

[3] J. E. Pedersen and S. R. Keiding, "Thz time-domain spectroscopy of nonpolar liquids," *IEEE J. Quantum Electron.*, vol. 28, pp. 2518–2522, 1992.

[4] K. Wang and D. M. Mittleman, "Metal wires for terahertz wave guiding," *Nature*, vol. 432, pp. 376–379, 2004.

[5] K. J. Chau, G. D. Dice, and A. Y. Elezzabi, "Coherent plasmonic enhanced terahertz transmission through random metallic media," *Phys. Rev. Lett.*, vol. 94, no. 173904, 2005.

[6] T. J. Yen, W. J. Padilla, N. Fang, D. C. Vier, D. R. Smith, J. B. Pendry, D. N. Basov, and X. Zhang, "Terahertz magnetic response from artificial materials," *Science*, vol. 303, pp. 1494–1496, 2004.

[7] H. Chen, W. J. Padilla, J. M. O. Zide, A. C. Gossard, A. J. Taylor, and R. D. Averitt, "Active terahertz metamaterial devices," *Nature*, vol. 444, pp. 597–600, 2006.

[8] Q. Wu, M. Litz, and X. C. Zhang, "Broadband detection capability of znte electro-optic field detectors," *Appl. Phys. Lett.*, vol. 68, pp. 2924–2926, 1996.

[9] E. Castro-Camus, J. Lloyd-Hughes, M. B. Johnston, M. D. Fraser, H. H. Tan, and C. Jagadish, "Polarization-sensitive terahertz detection by multicontact photoconductive receivers," *Appl. Phys. Lett.*, vol. 86, no. 254102, 2005.

[10] K. J. Chau, M. C. Quong, and A. Y. Elezzabi, "Terahertz time-domain investigation of axial optical activity from a sub-wavelength helix," *Opt. Express*, vol. 15, pp. 3557–3567, 2007.

[11] M. Cho, J. Kim, H. Park, Y. Han, K. Moon, E. Jung, and H. Han, "Highly birefringent terahertz polarization maintaining plastic photonic crystal fibers," *Opt. Express*, vol. 16, pp. 7–12, 2008.

[12] K. Kawase, Y. Ogawa, Y. Watanabe, and H. Inoue, "Non-destructive terahertz imaging of illicit drugs using spectral fingerprints," *Opt. Express*, vol. 11, pp. 2549–2554, 2003.

[13] J. L. Johnson, D. M. Mittleman, and J. van Rudd, "Cross-polarized angular emission patterns from lens-coupled terahertz antennas," *J. Opt. Soc. Am. B: Opt.*, vol. 18, pp. 1524–1533, 2001.

[14] M. T. Reitne, D. Grischkowsky, and R. A. Cheville, "Properties of surface waves determined via bistatic terahertz impulse ranging," *Appl. Phys. Lett.*, vol. 78, pp. 1146–1148, 2001.

[15] G. Zhao, R. N. Schouten, N. van der Valk, W. T. Wenckebach, and P. C. M. Planken, "Design and performance of a thz emission and detection setup based on a semi-insulating gaas emitter," *Rev. Sci. Instrum.*, vol. 73, pp. 1715–1719, 2002.

[16] A. J. Taylor, G. Rodriguez, and D. Some, "Ultrafast field dynamics in large-aperture photoconductors," *Opt. Lett.*, vol. 22, pp. 715–717, 1997.

[17] G. Rodriguez and A. J. Taylor, "Screening of the bias field in terahertz generation from photoconductors," *Opt. Lett.*, vol. 21, pp. 1046–1048, 1996.

[18] K. J. Chau, "Terahertz electromagnetic wave interaction with mesoscopic media," Ph.D. dissertation, University of Alberta, 2008.

[19] D. J. Griffiths, *Introduction to Electrodynamics*, 3rd ed. New Jersey: Prentice Hall, 1999.

[20] A. Taflove, *Computational Electrodynamics*. Boston: Artech House, 1995.

[21] J. F. Holzman, "Terahertz waveform generation," Ph.D. dissertation, University of Alberta, 2003.

Chapter 3

Active Terahertz Spin-Plasmonic Artificial Materials

3.1 Background

With the advent of modern methods to control electronic signals, information technologies have flourished over the last several decades. The information processing capacity of processors, measured in transistor counts, has steadily doubled approximately every two years since the 1950's, which embodies the famous Moore's Law. However, as the size of electronic components is nearing a fundamental minimum, the speed and capacity is approaching a maximum. Accordingly, researchers are turning their attention to the possibility of photonic-based circuits to exploit the high information speeds possible with light. In light of this, *active* control over the propagation of radiation and photonic switching mechanisms will become essential as future information technologies transfer from electrical based systems to photonics based systems.

In this chapter a class of active plasmonic THz devices is introduced, where by varying the design parameters various modes of operation can be realized. The transmission of THz radiation through the devices is mediated by the near-field coupling of non-resonant particle plasmons [1, 2] in dense ensembles of subwavelength ferromagnetic particles. By inserting a small number of subwavelength dielectric particles ($< 35\%$ by volume), the phase accumulation of THz radiation in the device can be spatially modulated. Moreover, by expoiting AMR in the ferromagnetic particles, the spatial dependence of the phase accumulation can be *actively* controlled with the application of an external magnetic field. To demonstrate the versatility of this class of THz devices, the recipes for two modes of operation are modelled, with support from finite-difference time-domain (FDTD) calculations. First considered is an active plasmonic directional router, capable of actively adjusting the propagation direction of THz beams, and the second mode of operation considered is an active plasmonic THz lens, capable of focusing THz radiation with a tune-

able focal length. The possible devices are not limited to these two examples and may include, for instance, active diffraction gratings or active wave plates. However, the two examples discussed in detail in this Chapter provide a clear representation of the flexibility and capabilities of this class of active plasmonic devices. Moreover, a directional router is developed and experimentally characterized, verifying the theoretical predictions.[1]

The active plasmonic devices consist of mixtures of ferromagnetic and dielectric particles. The metal to dielectric volume fraction, f_m, is defined to characterize the relative amounts of the two species, and is given by

$$f_m = \frac{V_m}{V_m + V_d}, \tag{3.1}$$

where V_m and V_d are the total volumes of the metallic and dielectric particles, respectively. When the ferromagnetic particles are Co and the dielectric particles are sapphire, it has been shown that there are three distinct regimes of transport through the ensemble of particles [3]. For $f_m < 0.10$ the ensemble consists primarily of dielectric particles, and the transport of THz radiation through the particle ensemble is governed by ballistic small-angle forward scattering of photons through the sapphire particles. Alternatively, when $f_m > 0.67$ the ensemble consists primarily of metallic particles and transport is governed by the near-field plasmonic coupling between the Co particles. For $0.10 < f_m < 0.67$ the transport is mediated by a combination of the two phenomena, which manifests as a regime of atypic effective refractive index that cannot be explained by effective medium theory [3]. The regime of interest for the active plasmonic devices to be introduced here is $f_m > 0.67$, where

[1]The results of this Chapter have been published in *Applied Physics Letters*, "A magnetically active terahertz plasmonic artificial material," **94**, 071115 (2009) and *Optics Express*, "Active plasmonic devices via electron spin," **17**, 7117-7129 (2009).

the effective refractive index, n, is related to f_m through the relation [3]

$$n = -Cf_m \tag{3.2}$$

where C is a positive constant of proportionality. This behaviour occurs because f_m is decreased by removing dielectric particles, which decreases the optical distance between the ferromagnetic particles. Accordingly, the particle plasmons couple more effectively and the propagation speed is enhanced, corresponding to a decrease in n. It it important to note that the effective absorption of the ensemble of particles is constant for $f_m > 0.67$. By controlling the spatial dependence of f_m, the position-dependent effective refractive index of the ensemble of particles (i.e. position dependent phase accumulation of the THz radiation) can be controlled. Fortunately, since the absorption does not depend on f_m, there are no position dependent losses.

3.2 Active THz Directional Router

With the ability to control the effective refractive index of the artificial material, a multitude of device implementations are possible. Perhaps the simplest device possible is a directional router, which induces a change in the propagation direction of transmitted radiation. This operation can be realized if the effective index of refraction varies across the device such that the device behaves like a prism, as shown in Figure 3.1.

The required spatial dependence of the refractive index, $n_o(x)$, and expected deflection angle, Θ, for a directional router is determined from first principles by considering the optical path length (OPL) of rays sharing a common wavefront that pass through the device, as depicted in Figure 3.2(a). For any ray transmitted through the directional router at position x, the OPL

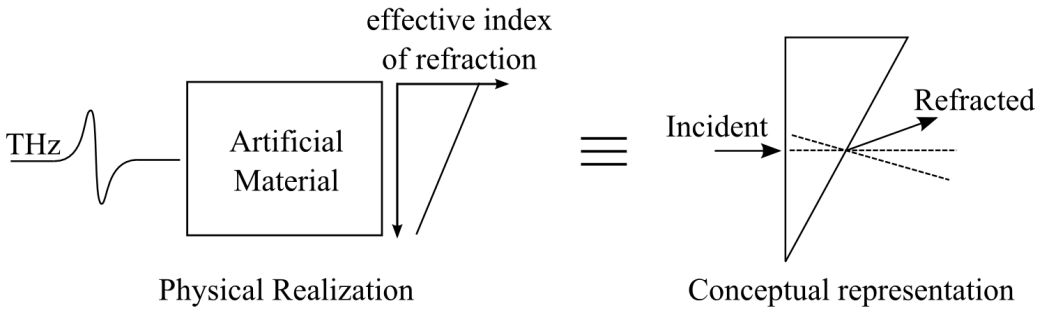

Figure 3.1: Depiction of a THz pulse incident on an artificial material having a spatially varying effective refractive index, where the material behaves like a prism and refracts the radiation.

from the start of the device to the wavefront depicted in Figure 3.2(a) is given by $OPL = n_o(x)d + x\sin\Theta$, where d is the thickness of the device. Since the OPL for any two rays along the wavefront must be equal for coherent transmission, one can write

$$n_o(0)d = n_o(x)d + x\sin\Theta. \tag{3.3}$$

where it has been assumed that the medium surrounding the device is air. Equation (3.3) is satisfied if $(n_o(x) - n_o(0)) << (n_o(x) + n_o(0))/2$, which allows the slight curvature of the rays in the sample to be ignored. Therefore, the refractive index profile for a directional router is given by

$$n_o(x) = -x\frac{\sin\Theta}{d} + n_o(0). \tag{3.4}$$

By considering Equation (3.2), it is evident that the effective refractive index profile given by Equation (3.4) can be realized by specifying an f_m that linearly varies from $f_m = 0.67$ at position $x = 0$ to $f_m = 1$ at position $x = w$. To account for imperfections of the effective refractive index profile, a figure of merit, $0 \leq Q_1 \leq 1$, is defined and, as such, the expected deflection angle is

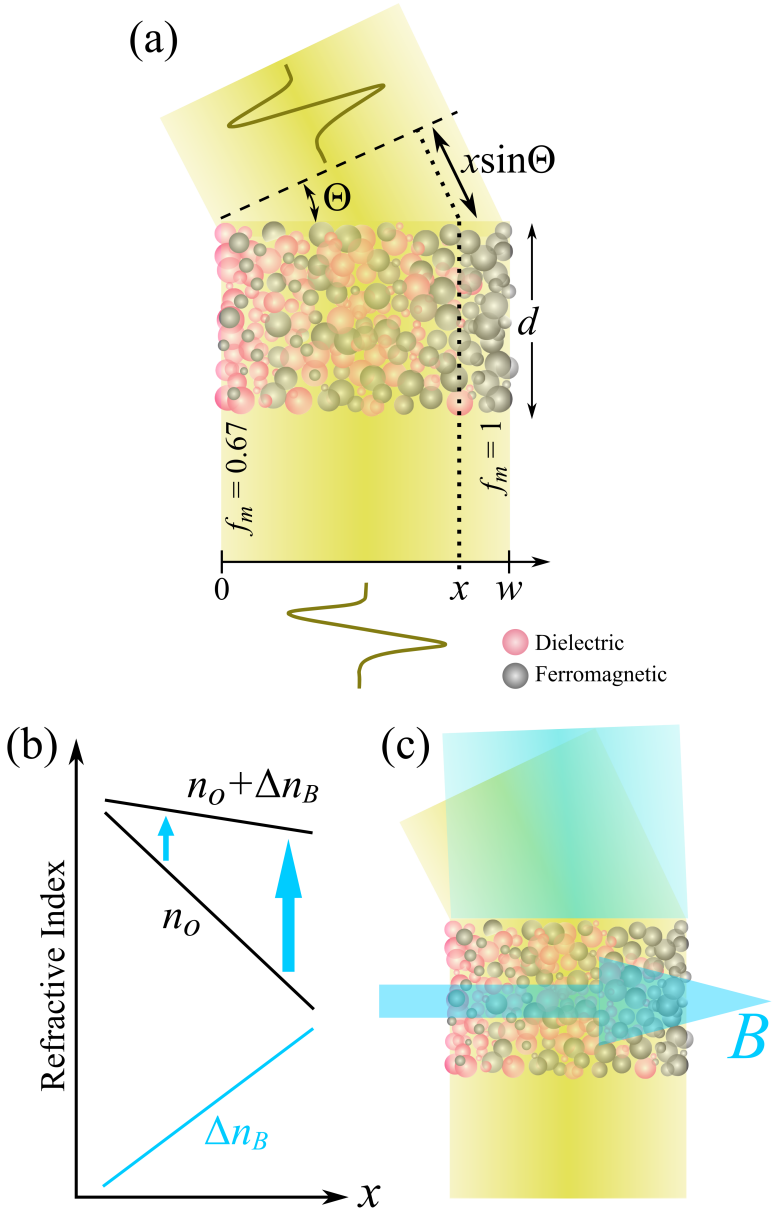

Figure 3.2: (a) Schematic diagram illustrating the deflection of THz radiation by a device consisting of a collection of dielectric and ferromagnetic subwavelength particles having a linearly varying f_m. Panel (b) depicts how the application of B results in a position-dependent effective refractive index increase by Δn_B and, therefore, the overall effective index becomes $n_o + \Delta n_B$. As shown in panel (c), this corresponds to a reduction of the THz deflection compared prior the application of B.

given by

$$\sin\Theta = Q_1 \left(\frac{n_{0.67} - n_1}{w} \right) d, \tag{3.5}$$

where $n_{0.67}$ and n_1 are the indices of refraction for $f_m = 0.67$ and $f_m = 1$, respectively.

The active behaviour of the directional router is formulated by considering the effect of applying an external magnetic field, B, to the device. As discussed in Chapter 1, in a ferromagnetic metal the resistivity, ρ, depends on B through the relation $\rho(B) = \rho_0 + \rho_{Lorentz}(B) + \rho_{AMR}(B)$, where ρ_0 is the background resistivity, $\rho_{Lorentz}(B)$ is the contribution from Lorentz force that is present in all metals, and $\rho_{AMR}(B)$ is the contribution from AMR that is only present in ferromagnetic metals due to spin-orbit interaction [4]. In the context of THz transmission mediated by the near-field coupling of particle plasmonic oscillations, AMR results in a B-dependent delay, $\Delta\tau_B$, of the arrival times of the transmitted THz pulses [5]. As discussed in Chapter 1, the transient response of the localized THz plasmons is primarily dictated by the current densities exited within the particle skin depth. Applying B increases the resistivity along the magnetic field direction, which inhibits the plasmonic current and manifests as $\Delta\tau_B$. Moreover, since the plasmonic oscillations are dipolar, the current direction is primarily along the electric field polarization direction of the THz radiation, as shown in Figure 3.3. Therefore, $\Delta\tau_B$ is

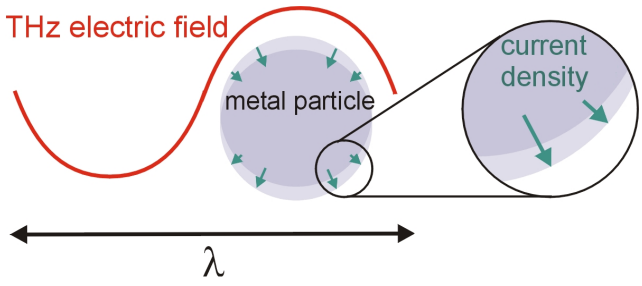

Figure 3.3: Illustration of the plasmonic current density induced by the THz electric field in subwavelength metallic particles.

maximum for a THz electric field polarization parallel to **B** and, to maximize the active response of the artificial materials to be introduced here, such an orientation will be assumed.

Since $\Delta\tau_B$ scales linearly with thickness of the ensemble of particles [5], it is a cumulative effect that depends on the number of ferromagnetic particles traversed by the radiation and can be expressed as

$$\Delta\tau_B = \frac{K_1(B)N_m}{d}, \tag{3.6}$$

where N_m is the number of ferromagnetic particles in the sample and $K_1(B)$ is a B-dependent delay per unit of linear ferromagnetic particle density in the direction of propagation of the THz radiation. Since $\Delta\tau_B$ is a function of N_m, it is meaningful to re-write Equation (3.1) as a function of N_m. If it is assumed that the packing fraction of the particles, $f_P = (V_m + V_d)/V_{Cell}$, is constant for all f_m, Equation (3.1) can be expressed as

$$f_m = \frac{\langle V_m \rangle N_m}{V_{Cell} f_P} \tag{3.7}$$

where $\langle V_m \rangle$ is the average volume of a single Co particle and V_{Cell} is the volume of the cell that contains the particles. Note that the assumption that f_P remains constant for all f_m is valid if the ferromagnetic and dielectric particles of similar size. Then, Equations (3.6) and (3.7) can be combined to yield

$$\Delta\tau_B = \frac{K_1(B)V_{Cell}f_P}{\langle V_m \rangle d} f_m. \tag{3.8}$$

Accordingly, application of B results in an increase of the effective index of

refraction of the ensemble of particles, Δn_B, given by

$$\begin{aligned}\Delta n_B &= \frac{c\Delta\tau_B}{d} \\ &= \frac{cK_1(B)V_{Cell}f_P}{\langle V_m\rangle d^2} f_m \end{aligned} \tag{3.9}$$

where c is the speed of light. Interestingly, since both $n \propto f_m$ [Equation (3.2)] and $\Delta n_B \propto f_m$ [Equation (3.9)], the application of B does not change the functional form of the spatial dependence of the effective index of refraction for any spatial variation of f_m. Thus, for this example of a directional router $\Delta n_B(x)$ is a linear function of x. Notably, the slope of $\Delta n_B(x)$ is opposite of $n_o(x)$ since the former is positively proportional to f_m while the latter is negatively proportional to f_m. As shown in Figure 3.2(b), the application of B (which causes $\Delta n_B \neq 0$) results in a net decrease in the effective index gradient. In turn, this results in a B-dependent deflection angle given by

$$\begin{aligned}\Theta(B) &= \sin^{-1}\left(Q_1 d\left[\frac{n_{0.67}-n_1}{w} - \frac{0.33cK_1(B)V_{Cell}f_P}{w\langle V_m\rangle d^2}\right]\right) \\ &= \sin^{-1}\left(Q_1 d\left[\frac{n_{0.67}-n_1-K_2(B)}{w}\right]\right), \end{aligned} \tag{3.10}$$

where $K_2(B)$ is a dimensionless parameter that results in a reduction of Θ as B is increased, as depicted in Figure 3.2(c). For exceedingly large B-values where $K_2(B) > n_{0.67} - n_1$, it would be possible for the deflection to be in the opposite direction. Notably, $K_2(B)$ is an intrinsic parameter that does not depend on f_m and, accordingly, describes the B-dependence of the phase accumulation for any device where f_m is position dependent.

3.3 Active THz Lens

To illustrate that various modes of operation can be realized by defining other spatial variations of f_m, the requirements for an active plasmonic lens will be described. Similarly to the treatment used for the directional router, the required spatial dependence of the effective refractive index is determined by evaluating the optical path length of rays that travel through the device, as shown in Figure 3.4(a). In order to focus the radius, the OPL in the center of the device must be longer than at the edges. Therefore, the effective index is set to $n_{0.67}$ in the center and n_1 at the edges, and the spatial dependence can be calculated by combining these boundary conditions with the assumption that the wavefronts are cylindrical upon exiting the device. It can be surmised from Figure 3.4(a) that any ray that passes through the device at a position x will have an optical path length from the beginning of the device to the cylindrical wavefront given by $OPL = dn_o(x) + \sqrt{x^2 + F^2} - F$, where x is the transverse distance from the center of the device, $n_o(x)$ is the effective refractive index (without the application of B), and F is the focal length. Since the OPL for any value of x will be equal to the OPL for $x = 0$, it can be written

$$n_o(x) = n_{0.67} - \frac{\sqrt{x^2 + F^2} - F}{d}, \tag{3.11}$$

By substituting in the boundary condition at $x = w/2$, the following formula for F is produced

$$\sqrt{(w/2)^2 + F^2} - F = Q_2 d(n_{0.67} - n_1) \tag{3.12}$$

where $0 \leq Q_2 \leq 1$ is a figure of merit defined to account for imperfections of the effective refractive index spatial profile. For the case $F >> w$, a parabolic

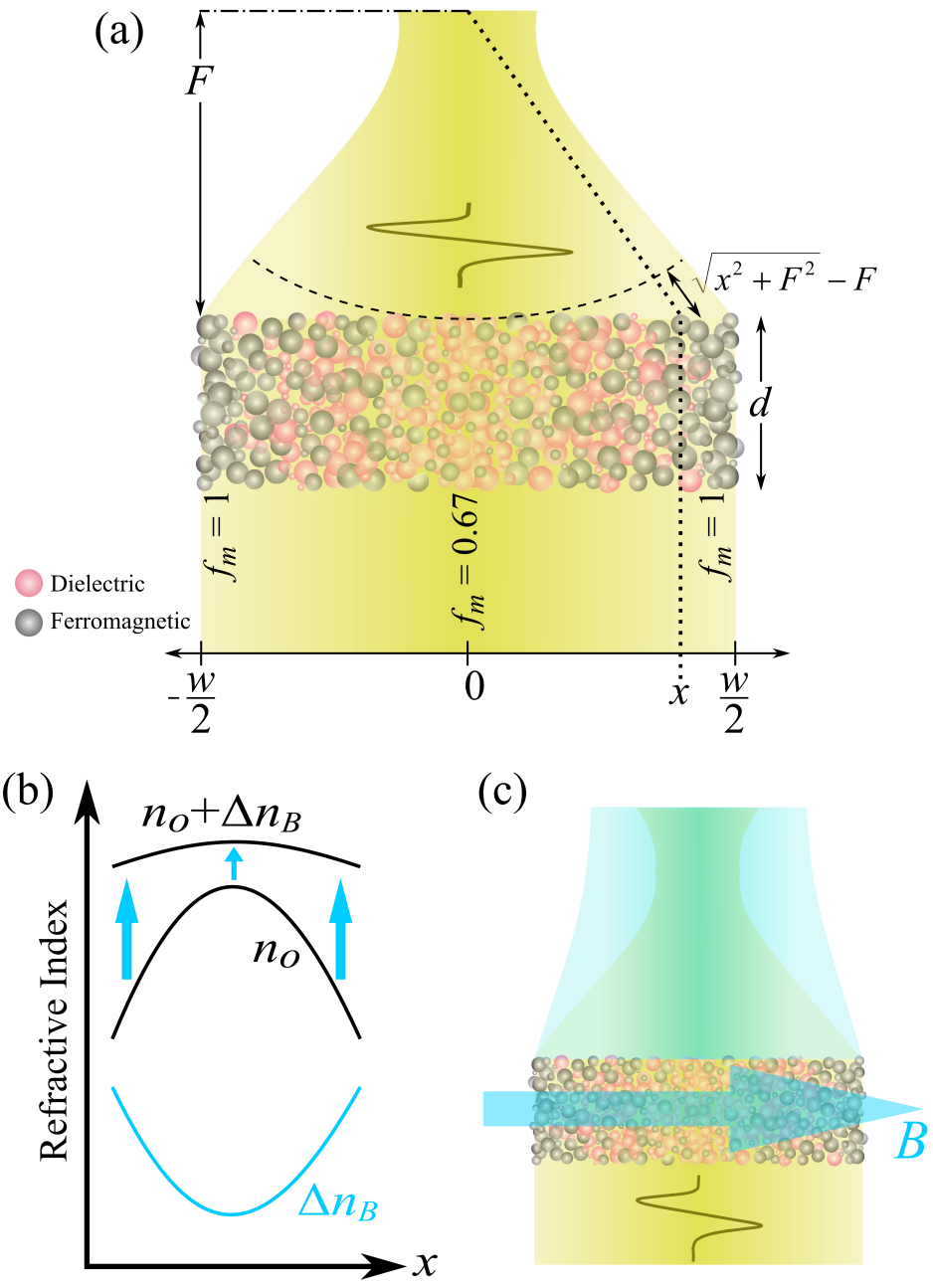

Figure 3.4: (a) Schematic diagram illustrating the focusing of THz radiation by a device consisting of a collection of dielectric and ferromagnetic subwavelength particles having a non-linearly varying f_m. Panel (b) depicts how the application of B results in a position-dependent effective refractive index increase by Δn_B and, therefore, the overall effective index becomes $n_o + \Delta n_B$. As shown in panel (c), this corresponds to an increase of the THz focal length compared to prior to the application of B.

spatial dependence of the index refraction and focal length given by

$$n(x) = n_{0.67} - \frac{x^2}{2Fd} \tag{3.13}$$

$$F = \frac{w^2}{8Q_2 d(n_{0.67} - n_1)} \tag{3.14}$$

are realized, respectively. By invoking Equation (3.9), it can be shown that the application of B results in a $\Delta n_B(x)$ that is a parabolic function of x having concavity opposite to that of $n_o(x)$, as illustrated in Figure 3.4(b). Thus, the B-dependent focal length is given by

$$F(B) = \frac{w^2}{8Q_2 d(n_{0.67} - n_1 - K_2(B))}. \tag{3.15}$$

It is evident that as K_2 increases to $K_2 = n_{0.67} - n_1$ the focal length increases, as shown in Figure 3.4(c), and $K_2 > n_{0.67} - n_1$ results in negative values of F, which can be interpreted as a diverging lens.

3.4 Finite-Difference Time-Domain Calculations

To demonstrate the passive operation of a directional router and lens, FDTD calculations [6] are performed. The devices consist of 3.1 mm thick ensembles of Co and sapphire particles having diameters of $\delta_C = 75$ µm and $\delta_S = 100$ µm, respectively. The index of refraction of each sapphire particle is set to 3.24 [7], while the electromagnetic response of the Co particles is modeled using a Drude permittivity given by $\epsilon(\omega) = 1 - \omega_p^2/(i\nu\omega + \omega^2)$, where $\omega_p = 9.60 \times 10^{14}\text{s}^{-1}$ is the plasma frequency and $\nu = 8.85 \times 10^{12}\text{s}^{-1}$ is the damping frequency [8]. To implement a varying f_m in the x-direction for randomly positioned particles, a random number generator with a linearly sloped probability distribution is utilized. A random number generator with a uniform probability distribution

is utilized to determine the y-coordinates of the particles. Therefore, using this approach a directional router with f_m linearly varying from 1 to 0.67 over a distance of 3 mm is studied, as shown in Figure 3.5(a). A single-cycle, 2 ps long THz pulse polarized along the x-direction is focused onto the sample with a focal spot intensity FWHM of 1.1 mm to prevent the THz electric field from extending outside the gradient region of the device. Starting from a time 10 ps after the THz pulse is incident on the device, Figure 3.5(b-e) depict the transverse electric field, E, in 5 ps intervals as the THz pulse passes through the device. Here, it is seen that the wavefront of the pulse tilts toward the left side of the sample (i.e. tilted toward the side where f_m is lower) as time evolves. As shown in Figure 3.5(f), a clear deflection of the THz pulse propagation direction is evident 50 ps after the THz pulse is incident on the device. The divergence of the wavefront as the transmitted pulse propagates away from the sample is attributed to the relatively small transverse size of the incident THz radiation. To characterize the deflection angle, the angular-dependent average intensity, $I(\theta) \propto \langle E^2 \rangle$, is calculated, where θ is the angle subtended from the y-axis, r is the radial distance, and $\langle \cdots \rangle_r$ denotes averaging over the radial direction, as shown in Figure 3.5(g). If the angle of deflection is estimated as the centroid of the curve, an angular deflection of $\Theta_{FDTD} = 8°$ is observed.

To demonstrate the passive operation of a lens, f_m is varied approximately parabolically by using four equally spaced segments 1.5 mm long that each have a linearly varying f_m, as shown in Figure 3.6(a). The only difference in simulation parameters from the directional router calculations is that the incident THz pulse is collimated with an intensity FWHM of 3.2 mm. Shown in Figure 3.6(b) and (c) is E for the incident THz pulse and E at a time 40 ps after a THz pulse is incident on the device, respectively. It is evident that the pulse is focused by the device, and to more clearly illustrate this the transverse

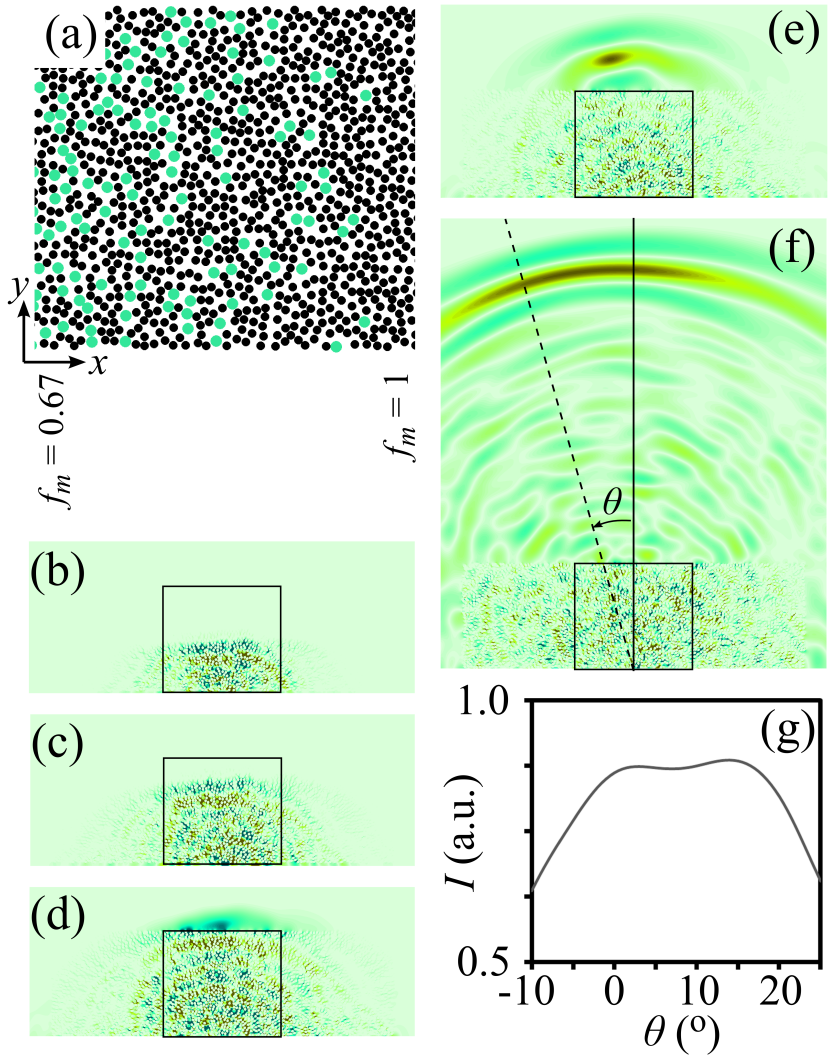

Figure 3.5: (a) Depiction of the sapphire (green) and Co (black) particle distribution for the plasmonic router implemented in the FDTD calculations. Panels (b) - (f) depict snapshots of the electric field amplitude at times of 10 ps, 15 ps, 20 ps, 25 ps, and 50 ps after a THz pulse is incident on the device, respectively. The box in (b) - (f) indicates the location of the particles shown in (a). Panel (g) depicts the intensity, $I(\theta)$, calculated from panel (f) for θ ranging from $-10°$ to $20°$.

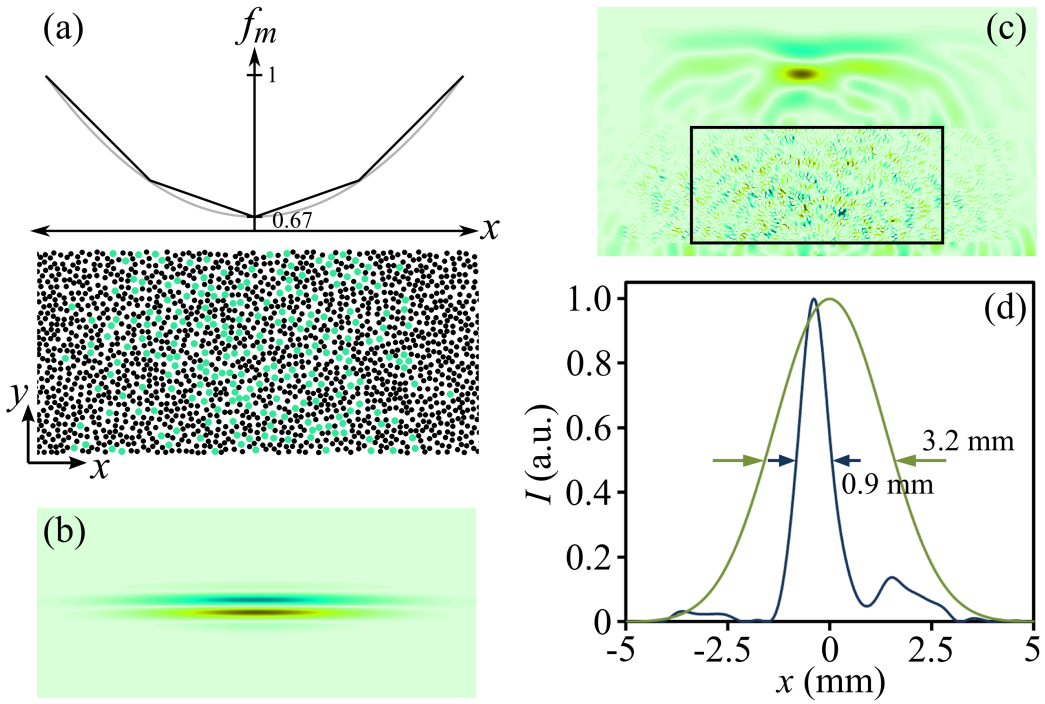

Figure 3.6: (a) Depiction of the sapphire (green) and Co (black) particle orientation for the plasmonic lens implemented in the FDTD calculations. The plot above the depiction of the particles shows how the parabolic f_m (grey) is approximated using 4 equal length sections of linearly varying f_m (black). Panels (b) and (c) depict snapshots of electric field amplitude of the incident THz pulse and the electric field distribution after a collimated THz pulse has passed through the device, respectively. The box in (c) indicates the location of the particles shown in (a). Panel (d) depicts the intensity profile for the dominant lobe of the pulse for transmission through the device (blue) and free space (green).

profiles of the normalized intensity, $I(x) \propto E^2$, at the y-location of maximum intensity is shown in Figure 3.6(d). Accordingly, it is observed that the FWHM of I decreases from 3.2 mm to 0.9 mm with the implementation of the lens. The 0.4 mm deviation of the focal spot from the center axis is attributed to random asymmetry of the concentration of sapphire particles due to the pseudo-random number generation used to specify the particle locations. It is expected that a physical implementation would be less sensitive to non-symmetries since, in the two-dimensional FDTD approach, the THz electric field interacts with fewer particles due to the lack of the third dimension. Consequently, there are fewer particles present to average out local fluctuations in f_m when compared to a physical implementation. Nevertheless, the existence of this deviation highlights that it is important to maintain symmetry in the fabrication of the device.

3.5 Experimental Results

To verify the functionality of this class of active THz devices, a directional router is experimentally investigated. To create the device, Co and sapphire particles having mean sizes of $\delta_C = 74 \pm 23$ µm and $\delta_S = 100 \pm 12$ µm, respectively, are contained in a polystyrene cell. Since a smoothly varying f_m is technically challenging to implement, a linear variation of f_m is approximated by utilizing five 600 µm wide and 3.1 mm thick homogeneous regions having $f_m = 0.67$, 0.73, 0.81, 0.92, and 1, as shown in Figure 3.7(a). For each region the packing fraction (f_p) is measured to be 0.59 ± 0.1, which is attributed to the similar size of the Co and sapphire particles. The device is illuminated with THz pulses polarized in the direction parallel to the f_m variation and are generated and detected using the THz-TDS system described in Chapter 2. Since the THz-TDS system is capable of detecting the transmitted radiation at

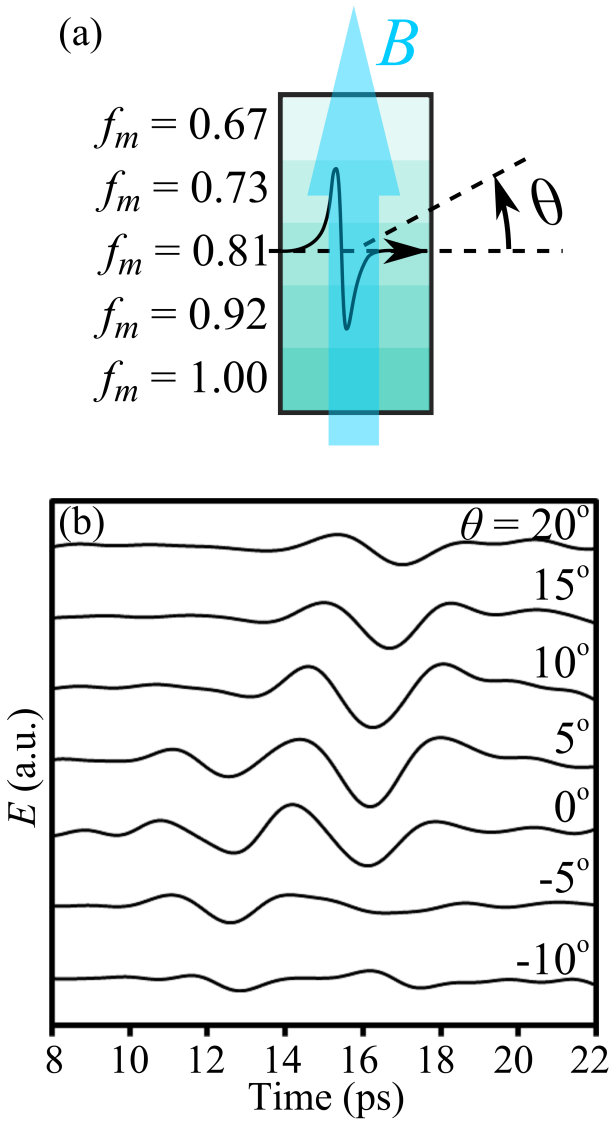

Figure 3.7: (a) Depiction of the experimental device consisting of 5 sections of constant f_m, where B is applied parallel to the THz electric field polarization. Panel (b) depicts the THz pulses transmitted through the plasmonic router for θ ranging from $-10°$ to $20°$.

any angle, θ, around the sample, it is ideal for the study and characterization of a directional router. Also, the wavelength of the THz pulses ($\sim$ 800 µm) is larger than thickness of each region, which results in the effective variation of f_m perceived by the THz pulses to be linear.

Shown in Figure 3.7(b) is the electric field (E) of the THz pulses transmitted through the device for θ ranging from $-10°$ to $20°$ in $5°$ increments, where it is evident that the maximum pulse amplitude is measured for $\theta = 5°$. From these results it can be discerned that the trailing lobes of the pulses have a deflection angle farther from $0°$ compared to the leading lobes, which was also evident in the FDTD calculations. This indicates that the deflection is not instantaneous but, rather, takes time to accumulate. To quantitatively compare the pulses, the average energy flux,

$$P(\theta)_\omega = \langle E(\omega)E^*(\omega)\rangle_\omega \,, \tag{3.16}$$

is calculated for each θ, where $E(\omega)$ is the frequency spectra of the pulses and $\langle\cdots\rangle_\omega$ denotes averaging over the bandwidth of the pulse. This technique is utilized to mitigate the effects of high frequency noise, and the results are shown in Figure 3.8(a). The experimental data is fitted with a Gaussian regression line, and the deflection angle is approximated as the center of the Gaussian fit, yielding $\Theta = 5.7°$. Also shown in Figure 3.8(a) is the normalized P for pulses transmitted through the empty cell containing no particles. The θ dependence of the transmission through two 3.5 mm control samples, S1 and S2, having f_m that does not vary spatially is measured to confirm that the deflection is a result of the varying f_m. For S1 $f_m = 1$ and for S2 $f_m = 0.67$, and as depicted in Figure 3.8(b), there is no deflection of the transmitted pulses for both cases. Interestingly, the 2 ps temporal delay between the THz

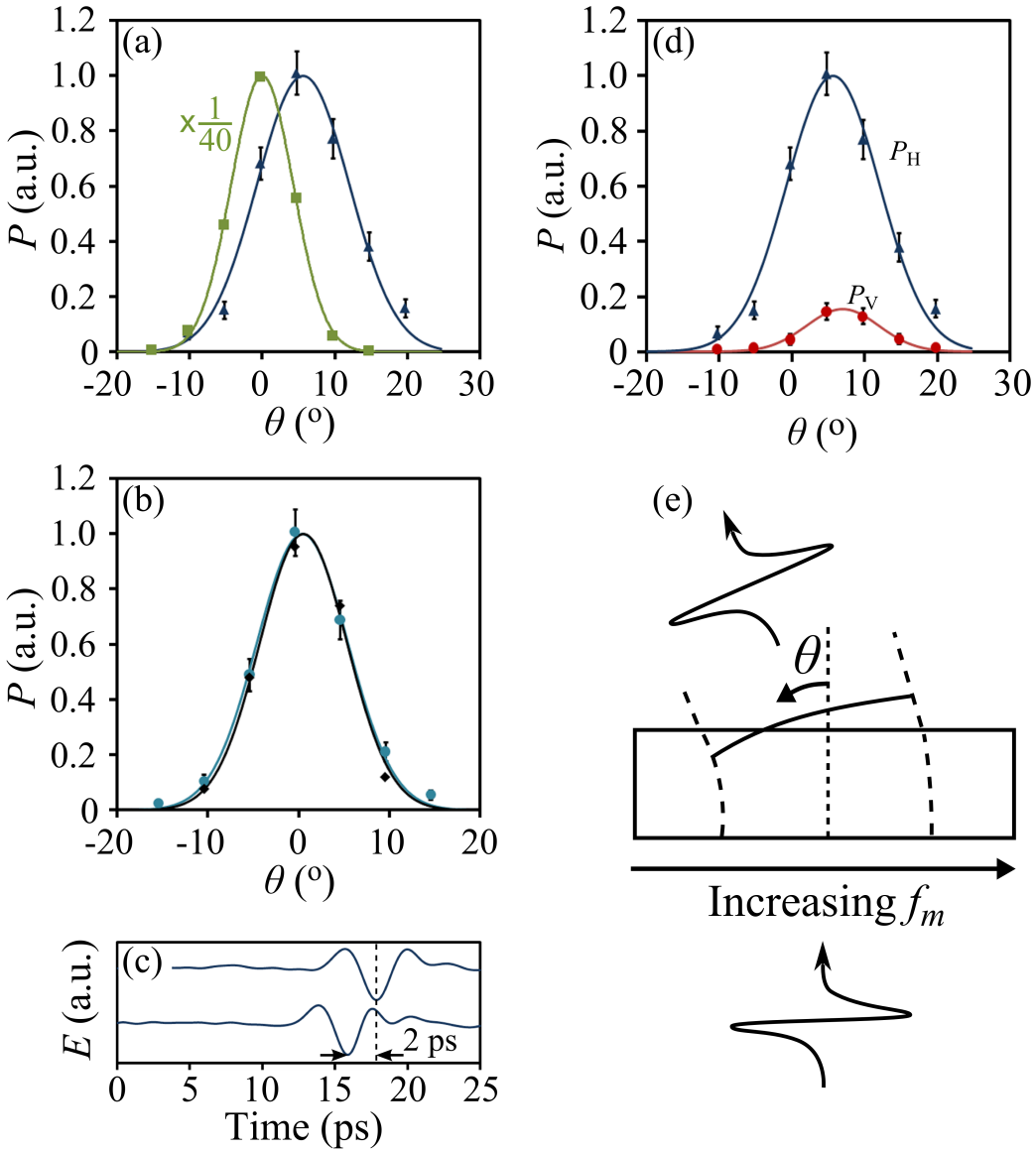

Figure 3.8: (a) The time averaged energy flux of THz pulses transmitted through the plasmonic router (blue) and an empty cell (green). Panel (b) depicts P for samples S1 (light blue) and S2 (black), while panel (c) depicts the on-axis THz signals transmitted through S1 and S2, where a 2 ps relative delay is observed. Panel (d) depicts P for the polarization components aligned parallel (blue, $P_{||}$) and perpendicular (red, $P_{\perp}$) to the incident THz pulses for transmitted through the plasmonic router. The diagram in panel (e) illustrates how portions of the wavefront that pass through regions with low f_m map to values of θ far from 0°. A Gaussian regression line is applied to the data in (a), (b), and (d) using a least-squares estimation.

pulses transmitted through S1 and S2, as depicted in Figure 3.8(c), can be used to determine that $n_{0.67} - n_1 = 0.17$. Inserting this value and the measured $\Theta = 5.7^\circ$ into Equation (3.5) yields $Q_1 = 0.58$.

It may be critical for some applications that the polarization of the pulses to remain linear after transmission through the directional router. To investigate the degree to which the polarization of the incident THz pulse is retained, the electric field with polarization perpendicular to that of the incident pulse is measured by rotating the EO crystal by 30° (Chapter 2). As shown in Figure 3.8(d), P is calculated for the THz pulses measured at various θ for the polarization states parallel ($P_{||}$) and perpendicular ($P_{\perp}$) to the polarization of the incident THz pulses. Here, it can be seen that the polarization is predominantly along the parallel direction, and by defining the polarization purity, η, as

$$\eta = \frac{A_{||} - A_{\perp}}{A_{||} + A_{\perp}} \tag{3.17}$$

where $A_{||}$ and $A_{\perp}$ are the amplitudes of the Gaussian regression lines for the ($P_{||}$) and ($P_{\perp}$) experimental data points, respectively, a value $\eta = 0.73$ is observed. The deviation from unity is attributed to polarization randomizing scattering events in the dielectric particles. This explanation is supported by considering the deflection angles for the parallel and perpendicular polarizations, which are $\Theta_{||} = 5.7^\circ$ and $\Theta_{\perp} = 6.9^\circ$, respectively. As illustrated in Figure 3.8(e), the portions of the THz wavefront that pass through regions with low f_m map to θ-values farther from 0°. As such, the regions of the wavefront that interact with more dielectric particles undergo more polarization randomizing scattering events and, therefore, $\Theta_{\perp} > \Theta_{||}$.

To study the active operation of the directional router, an external magnetic field, B, is applied along the direction parallel to the polarization of the incident THz pulses. As discussed earlier, this orientation is utilized to

maximize the AMR response. As shown in Figure 3.9(a), P is measured for θ ranging from -10° to 20° and B values of 0 mT, 27 mT, 45 mT, 55 mT, 69 mT, and 78 mT. As predicted by Equation (3.10), the application of B results in a reduction of the deflection angle that scales with the B-field magnitude. As shown in Figure 3.9(b), Θ decreases from 5.7° to 0.7° when $B = 78$mT, corresponding to an 88% reduction. Notably, the majority of the reduction (57% of the 5° reduction) occurs after a B-field strength of only 27 mT is applied.

It is possible to calculate $K_2(B)$ in Equation (3.10) using the experimentally obtained Θ. Values of $K_2(B)$ ranging from 0 to 0.15 are obtained for B ranging from 0 to 78 mT, as shown in Figure 3.10(a). To explore the frequency dependence of $K_2(B)$, averaging over ω in Equation (3.16) is not performed, thus enabling the calculation of $K_2(\omega, B)$. It should be noted that the FWHM of the amplitude spectra of the detected pulses span from 0.187 THz to 0.330 THz for $B = 0$ mT. As B is increased to 78 mT, the FWHM decreases to a span of 0.149 THz to 0.240 THz, which is attributed to the band limiting and red shift that is characteristic of photonic AMR [5]. To provide a meaningful spectral range, the spectral region defined by the overlap between the spectral characteristic FWHM's of the measured signals is used in the calculation of $K_2(\omega, B)$, which is shown in Figure 3.10(b). Interestingly, $K_2(\omega, B)$ exhibits negligible frequency dependence over the common spectral range despite the red shift induced by AMR, which validates the use of the frequency averaged Θ values to obtain the K_2 curve shown in Figure 3.10(a).

With the behaviour of K_2 established, it is possible to estimate the B-dependent focal length, $F(B)$, of an active plasmonic lens using Equation (3.15) provided that a suitable value for Q_2 can be predicted. If the lens is fabricated using a process and dimensions that are the same as that used for

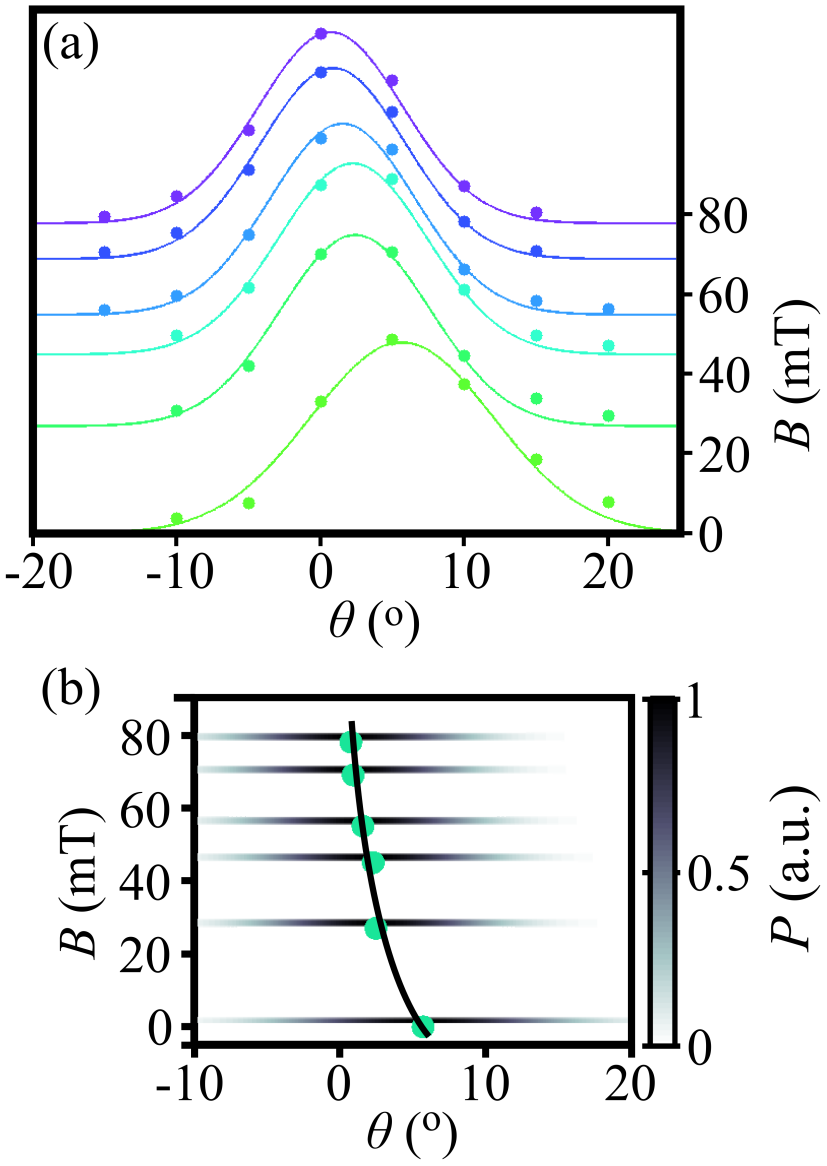

Figure 3.9: Depiction of $P(\theta)$ for THz pulses transmitted through the plasmonic router with external magnetic field strengths of 0 mT, 27 mT, 45 mT, 55 mT, 69 mT, and 78 mT. Panel (c) displays the same data and identifies $\Theta(B)$, which are located at the center of the Gaussian regression lines, for the given magnetic field strengths.

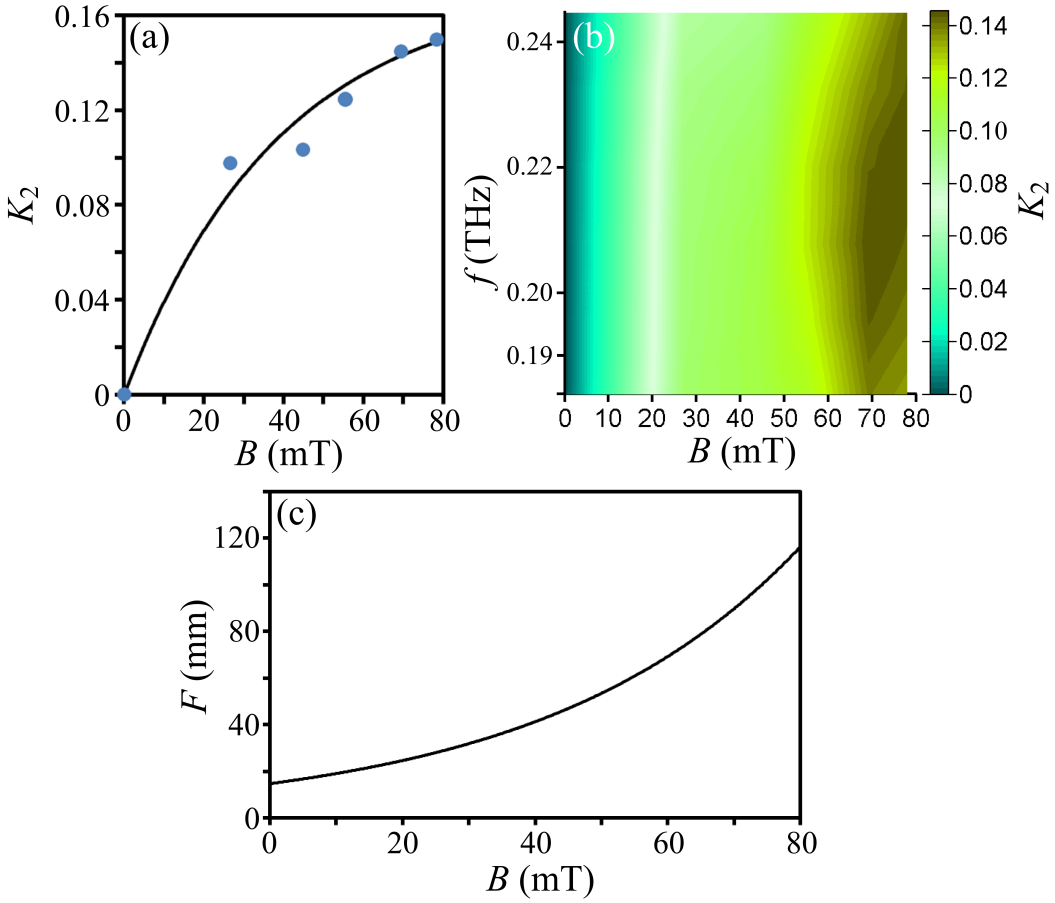

Figure 3.10: (a) Plot of K_2 calculated directly from the measured $\Theta(B)$ using Equation (3.10). Panel (b) depicts the frequency dependence of K_2, while panel (c) depicts the expected magnetic dependence of focal length for a plasmonic lens.

the directional router, it is reasonable to assume $Q_1 \approx Q_2$. Since f_m must vary from 1 to 0.67 twice [Figure 3.4(a)], the width should be twice that of the directional router studied here to ensure that the fabrication parameters would be most similar. By setting $w = 6$ mm and $d = 3.1$ mm, and using the $K_2(B)$ regression line depicted in Figure 3.10(a), the $F(B)$ shown in Figure 3.10(c) is realized. As such, for an active plasmonic lens defined by the given parameters, it is expected that F increases from 15 mm to 121 mm as B is increased from 0 mT to 80 mT. This corresponds to a marked 800% change, which is promising for the practical realization of such devices.

While the goal of this experimental work is to verify the feasibility of this class of active plasmonic artificial materials, it may be beneficial to have the largest Θ possible for practical applications. Therefore, the maximum Θ possible is estimated by looking closely at Equation (3.5). One important distinction when considering this estimation is that it is only applicable for Co and sapphire particles. If other ferromagnetic or dielectric particles are used, the behaviour would most likely differ. Nevertheless, examining Equation (3.5) reveals that minimizing w can increase Θ; however, there are several caveats to consider. First of all, w must be large enough to accommodate several microparticles. Also, w must be large enough to accommodate the width of the transverse THz electric field profile, which is constrained by the diffraction limit. Having too tight of focusing could also be undesirable since the THz radiation exiting the device would strongly diverge. With these limitations in mind, a minimum value of $w = 1$ mm is estimated. It is also apparent from Equation (3.5) that Θ could be increased by increasing d. The primary limitation of this approach is that the total absorption also increases with increased d. Under the present experimental conditions absorption losses become unacceptable for d greater than 3.5 mm. While the maximum acceptable

losses are extremely subjective to the application, this value will be used in the estimation. The final method to increase Θ is to refine the fabrication process, thereby increasing Q_1. However, it is not feasible to estimate the maximum possible Q_1 and the value for the current device ($Q_1 = 0.58$) will be implemented in the estimation. By inserting these values into Equation (3.5), a maximum deflection of $\Theta_{MAX} = 20°$ is estimated. Note that the deflection could also be increased without alteration of the directional router by placing a passive lens after it, as depicted in Figure 3.11.

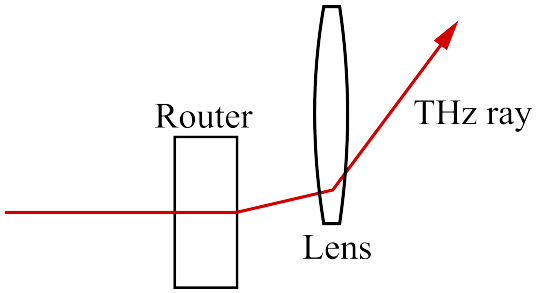

Figure 3.11: Illustration of how a passive lens can be used to increase the deflection induced by the router.

It is possible to estimate the minimum focal length for an active lens using Equation (3.12). Since focusing is only meaningful provided that the input THz pulse is collimated, w should be several wavelengths wide. As such, by inserting $w = 3$ mm, $d = 3.5$ mm and $Q_2 = 0.58$ into Equation (3.12), a minimum focal length of $F_{MIN} = 3.2$ mm is estimated.

It is important to address the amplitude attenuation of THz pulses transmitted through devices of this nature. As shown in Figure 3.8(a), the passage of the THz pulse through the directional router is accompanied by a factor of 40 reduction of transmitted energy flux. While this degree of attenuation may not be acceptable for some applications, for an active device that operates via the application of B, the amount of B-dependent attenuation may be more critical. For example, the absolute intensity at the focal spot of an

active plasmonic lens may not be very critical in comparison to the changes in amplitude associated with actively tuning the focal length. For $B = 78$ mT, the B-dependent attenuation is less than 20% relative to when $B = 0$.

3.6 Conclusion

In this Chapter, a class of active plasmonic devices that can be customized to fulfill various modes of operation has been discussed. The transmission through the devices is enabled by the near-field coupling of non-resonant particle plasmons between ferromagnetic particles, and the position-dependent phase accumulation of the radiation is actively controlled via an interplay between the presence of dielectric inclusions and AMR. As such, applying a uniform external magnetic field remodels the spatial dependence of the effective refractive index, which allows for the active adjustment of device behaviour. To illustrate the concepts, recipes for the creation of an active THz directional router and active THz lens are described in detail via a combination of theoretical discussion, FDTD calculations, and experimental results. In the case of the directional router, the deflection angle of transmitted radiation can be actively adjusted while in the case of the lens the focal length can be actively adjusted. While these two examples demonstrate the versatility of this class of devices, they are not the only possibilities since any arbitrary spatial dependence of the effective refractive index can be realized by controlling the relative amounts of metallic and dielectric particles. For example, an actively adjustable diffraction grating could be created by implementing a periodically varying effective refraction index. In this case, the application of the external magnetic field would decrease the amplitude of the index modulations, thereby decreasing the amount of diffraction. It is also important to note that ultrafast operation of the devices may be possible by using magnetic pulses. The

switching speed would be limited by the time it takes for the spin-states of the electrons in the ferromagnetic metal to orient themselves with the external magnetic field, which depends on the strength and duration of the magnetic pulse [9]. The active control over the propagation of THz radiation that is demonstrated by this work provides a new means of photonic control that may be applicable in active photonic systems.

3.7 Chapter 3 References

[1] K. J. Chau, G. D. Dice, and A. Y. Elezzabi, "Coherent plasmonic enhanced terahertz transmission through random metallic media," *Phys. Rev. Lett.*, vol. 94, no. 173904, 2005.

[2] K. J. Chau and A. Y. Elezzabi, "Terahertz transmission through ensembles of subwavelength-size metallic particles," *Phys. Rev. B*, vol. 72, no. 075110, 2005.

[3] A. Y. Elezzabi, K. J. Chau, C. A. Baron, and P. Maraghechi, "A plasmonic random composite with atypical refractive index," *Opt. Express*, vol. 17, pp. 1016–1022, 2009.

[4] T. R. McGuire and R. I. Potter, "Anisotropic magnetoresistance in ferromagnetic 3d alloys," *IEEE Trans. Magn.*, vol. 11, pp. 1018–1038, 1975.

[5] K. J. Chau and A. Y. Elezzabi, "Photonic anisotropic magnetoresistance in dense co particle ensembles," *Phys. Rev. Lett.*, vol. 96, no. 033903, 2006.

[6] A. Taflove, *Computational Electrodynamics*. Boston: Artech House, 1995.

[7] D. Grischkowsky, S. Keiding, M. van Exter, and C. Fattinger, "Far-infrared time-domain spectroscopy with terahertz beams of dielectrics and semiconductors," *J. Opt. Soc. Am. B*, vol. 7, pp. 2006–2015, 1990.

[8] M. A. Ordal, "Optical properties of fourteen metals in the infrared and far infrared: Al, Co, Cu, Au, Fe, Pb, Mo, Ni, Pd, Pt, Ag, Ti, V, and W." *Appl. Opt.*, vol. 24, pp. 4493–4499, 1985.

[9] I. Tudosa, C. Stamm, A. B. Kashuba, F. King, H. C. Siegmann, J. Stohr, G. Ju, B. Lu, and D. Weller, "The ultimate speed of magnetic switching in granular recording media," *Nature*, vol. 428, pp. 831–833, 2004.

Chapter 4

Exploring Plasmonic Giant Magnetoresistance

4.1 Background

A promising field of study is spintronics, where researchers exploit the quantum spin-state of electrons to offer new capabilities for electronics. A highly successful example of this is spin-induced giant magnetoresistance utilized in modern hard drive read heads. Perhaps the initial inspiration for the field of spintronics was the discovery of AMR [1]. In AMR, when an external magnetic field is aligned parallel to the current direction, the conduction electrons are more strongly scattered compared to when the magnetic field is aligned perpendicular to the current. As discussed in Chapter 1, this is due to spin-orbit interaction. Incidentally, it was this spin-dependent resistance phenomenon that provided the means for first generation computer hard drives [2].

Pioneering work involving spin-dependent transport which set the stage for modern spintronic devices was the discovery of the magnetic tunnel junction by Julliere [3]. In this work, two ferromagnetic layers were separated by a thin, 10 nm Ge tunnel junction and a potential difference was established between the two ferromagnetic layers. When the magnetizations of the magnetic layers were aligned parallel, a low-resistance channel for the up-spin current was realized. However, in the antiparallel configuration, the resistance associated with both current channels was the same and significantly less than the resistance of the up-spin channel in the parallel case. Thus, the resistance in the parallel configuration was observed to be less than the antiparallel configuration by 14%, similarly to in GMR. Although this effect was only seen at low temperature ($\sim 4^\circ$ K), it provided the basic motivation for more recent spin-related discoveries like spin-injection and GMR.

At the time of Julliere's work, the degree to which a spin-polarized current could maintain its polarization after injection into a non-magnetic metal was still not well understood. However, light was shed on the phenomenon with the

first experimental demonstration of spin-injection and detection, performed by Johnson in the 1980's [4–6]. These experiments enabled the direct measurement of the "spin-diffusion length": the characteristic distance an electron will diffuse before it loses memory of its initial polarization. Johnson performed further evidence and characterization of spin-accumulation under the architecture of a thin film geometry in 1994 [7]. After the demonstration that spin-polarized current could be transmitted and detected in a paramagnet, the GMR effect was quickly discovered in ferromagnetic/paramagnetic multilayers, where magnetizations were controlled be utilizing RKKY coupling [8]. Also, the GMR effect was discovered independently by another group using a ferromagnetic/paramagnetic/ferromagnetic trilayer [9]. The device created through this work was essentially the archetype for the modern day spin valve used in magnetic recording, and Fert [8] and Grunberg [9] were eventually awarded the Nobel Prize in Physics in 2007 for their independent discoveries of GMR.

An emerging field with the goal of providing a platform for subwavelength photonic devices is plasmonics. Of particular interest here is the particle plasmon-mediated transparency of dense ensembles of subwavelength-sized metallic particles. As discussed in Chapter 1, a THz electromagnetic pulse incident on the particles induces non-resonant particle plasmon oscillations, which have associated dipolar fields that couple from particle to particle [10, 11]. Since the induced surface currents of the particle plasmons are the root of the electromagnetic energy transport, it was natural to question whether effects traditionally seen in electronic transport could be applied to this unique type of photonic transport. Accordingly, the path to the field of spinplasmonics began similarly to the field of spintronics: with the discovery of an AMR-analogous photonic phenomenon by Chau and Elezzabi [12]. Similar

to the trend of spintronics research, the next discovery was the realization of optically induced spin-injection [13], where the interface resistance resulting from spin-accumulation resulted in a θ-independent attenuation of transmitted THz pulses. From these trends, it is plausible that it may be possible to electromagnetically induce GMR in such ensembles of microparticles. The work presented here represents the first steps toward this goal.

4.2 Experimental Design and Results

Similarly to the observations of spin-accumulation in the plasmonic enhanced propagation of THz radiation through dense ensembles of metallic particles, it may be possible to observe GMR phenomena by fabricating a GMR structure on metallic microparticles. If the plasmonic current densities interact with the GMR structure, as shown in Figure 4.1, the magnetoresistance that occurs due to GMR could potentially be observable in the properties of the transmitted THz pulses. It should be noted that since the plasmonic current passes through

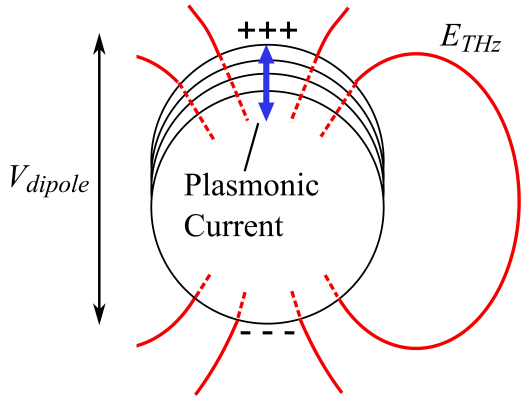

Figure 4.1: Depiction of a metallic microparticle with a GMR structure fabricated on top (the layer thicknesses are exaggerated for clarity), where a plasmonic current is excited such that it passes through the GMR device. The voltage across both the GMR device and particle, V_{dipole}, is modulated through magnetoresistance, and is probed through the measurement of the emitted THz electric field, E_{THz}.

both magnetic layers, a GMR spin valve geometry is realized rather than a non-local spin valve (NLSV). Moreover, since the THz electric field, E_{THz}, depends on the dipolar voltage difference, V_{dipole}, across the particle, the voltage across the entire structure is probed through the measurement of E_{THz}. The probing of voltage across the whole trilayer structure is also akin to a GMR spin valve geometry.

An important issue to consider is the random orientation of the particles. If an exchange biased spin valve with a antiferromagnetically pinned layer was fabricated onto the surface of each particle, the random orientation of the particles would preclude the possibility of aligning the external magnetic field antiparallel to the pinned layer magnetization for all the particles. Rather, only a portion would have the preferred alignment, thus reducing the cumulative effect from all the particles. The pseudo spin valve geometry avoids this limitation, however, since none of the layers are pinned. If one first saturates the magnetic layers in all the particles with a large uniform magnetic field, all the magnetizations in all the particles would be aligned and remain aligned even after the field was removed. Then, applying a magnetic field in the opposite direction would serve to cycle the device to the antiparallel, then parallel state, as described in Chapter 1. It should also be noted that GMR behaviour based on RKKY coupling is not desirable due to the large magnetic field strengths required to induce the parallel state ($\sim$ 1 T [8]).

A schematic of a pseudo spin valve on the surface of a particle is shown in Figure 4.2 (a). A non-magnetic metal is desirable as the host particle to prevent any significant contribution to the magnetic response by AMR and, as such, Cu particles with a mean size of 90 ± 15 µm are chosen [Figure 4.2 (b)]. The spin valve consists of a layer of Ni, a Cu spacer layer, and a layer of Co. Ni and Co are chosen because they have differing coercivities (0.7 Oe

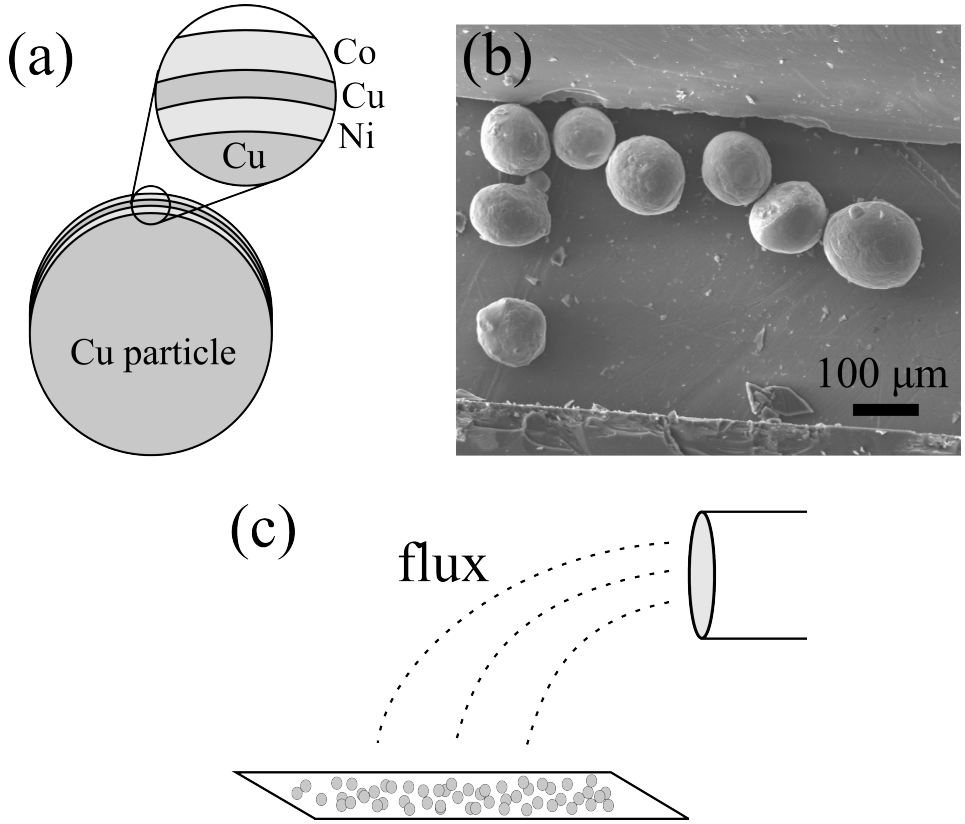

Figure 4.2: (a) Illustration of a Cu microparticle having layers of Ni, Cu, and Co deposited onto one side. Panel (b) depicts and scanning electron microscope (SEM) image of a selection of the Cu particles. Panel (c) depicts an illustration of off-axis sputtering, where the sputtering flux is directed downwards to the particles resting in a tray.

for bulk Ni and 10 Oe for bulk Co [14]) and are readily available. A challenge for the fabrication of the spin valves onto the particles is that it is difficult to mount the particles in a typical deposition system where the depositing flux is directed vertically upwards to the substrate. A mesh could be used to suspend the particles, but it was found that due to the mesh not being completely flat the particles pooled, and only a small portion were exposed to the deposition flux. Moreover, the mesh itself blocks a large portion of the flux. In light of these limitations, *off-axis* radio frequency (RF) sputtering was implemented, where the particles rest in a flat tray and the deposition flux is incident from above, as shown in Figure 4.2 (c). To thoroughly test for the phenomenon, samples with various thicknesses of the spin valve layers are prepared, as shown in Table 4.1. The fabrication of all the samples tested in this Chapter was performed by Mehmet Egilmez (Thin Films, Multilayers and Nanostructures Laboratory, Department of Physics, University of Alberta).

Sample	Layers	thicknesses (nm)
1	Ni/Cu/Co	5/2/5
2	Ni/Cu/Co	5/4/5
3	Ni/Cu/Co	10/4/10
4	Ni/Cu/Co	20/4/20
5	Ni/Cu/Co	10/2/10
6	Ni/Cu/Co/Cu/Ni/Cu/Co	5/2/5/2/5/2/5

Table 4.1: The materials used and layer thicknesses for the pseudo spin valve structures. The order of the elements listed for each entry in the Layers column is representative of the order of deposition, with the layer first deposited onto the particles being the first element listed.

The THz transmission through a 1.9 mm thick, random ensemble of Cu particles with spin valves fabricated on them is studied using the THz-TDS system described in Chapter 2. To search for signatures of GMR in the transmitted pulses an external magnetic field, B, is applied. The orientation of the magnetic field is perpendicular to the THz electric field polarization to miti-

gate any B-dependence that may arise from AMR in the ferromagnetic layers [12]. For samples 1, 2, and 3, B ranging from 0 mT to 35 mT in ~ 0.3 mT increments for $B < 10$ mT and ~ 2 mT increments for $B > 10$ mT is applied. Before incrementing B in the positive direction, a large negative magnetic field is applied to reverse-bias the magnetization of the ferromagnetic layers. Thus, it follows that by positively increasing B the spin valve should enter into the antiparallel state and then the parallel state in succession (Section 1.3). Figure 4.3 shows the THz pulse transmitted through sample 1 for $B = 35$ mT and for $B = 0$. Clearly there is no observable B-dependence that exceeds the noise level, which was the case for all tested B-values for samples 1-3. To test whether the lack of observable B-dependence was not simply due to not applying a strong enough magnetic field, an electromagnetic with a maximum field strength ~ 80 mT was implemented for samples 4, 5, and 6. However, similarly to the first three samples there was no observed B-dependence.

A possible explanation for the lack of magnetic dependence is that the coercivities of Ni and Co are too similar to allow a strong occurrence of the antiparallel state of the spin valve. To explore this possibility Ni is replaced with Permalloy (PA), which has an extremely low coercivity (0.05 Oe for bulk PA [14]), and the samples listed in Table 4.2 are tested. Here, B ranging from

Sample	Layers	thicknesses (nm)
7	PA/Cu/Co	10/2/10
8	PA/Cu/Co/Cu/PA/Cu/Co	5/2/5/2/5/2/5

Table 4.2: The materials used and layer thicknesses for the pseudo spin valve structures containing permalloy (PA) instead of Ni. The order of the elements listed for each entry in the Layers column is representative of the order of deposition, with the layer first deposited onto the particles being the first element listed.

0 mT to 80 mT is applied in 0.5 mT increments for $B < 5$ mT and ~ 3 mT increments for $B > 5$ mT. For these samples there is once again no observable

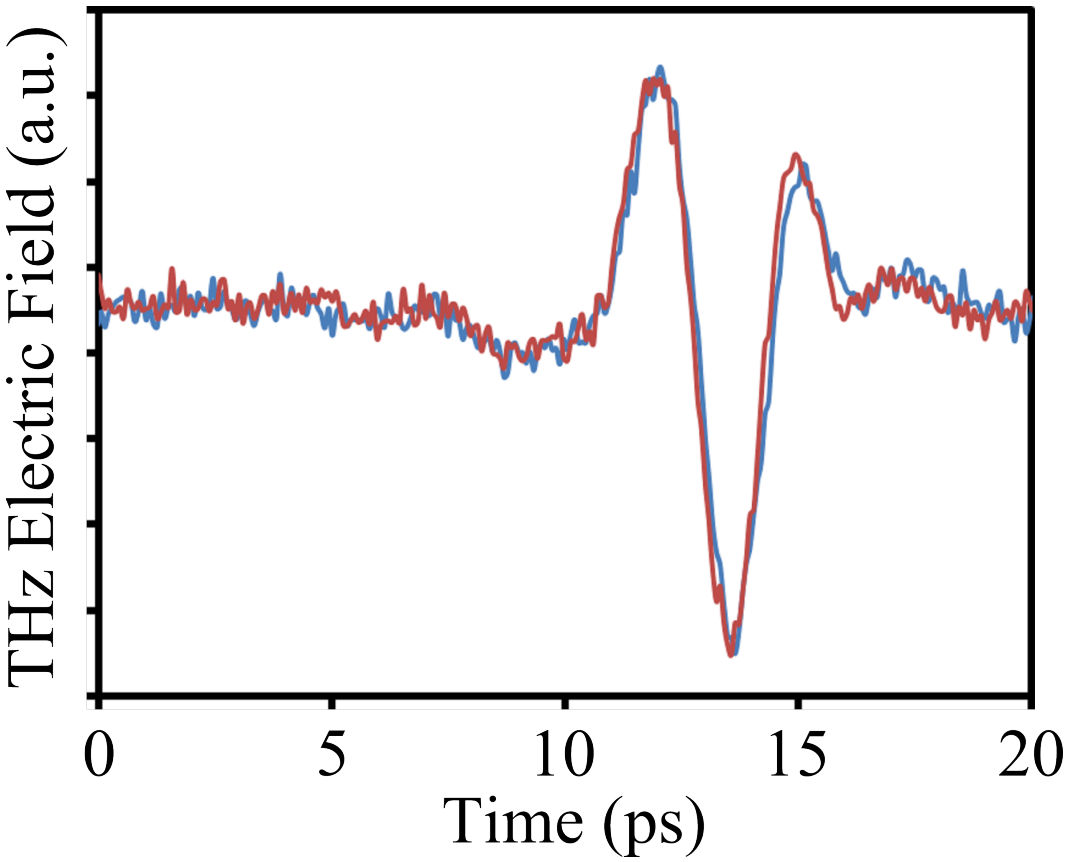

Figure 4.3: Measured THz electric field waveforms for transmission through sample 1 with $B = 0$ and $B = 35$ mT. The noise has not been filtered out to illustrate that any differences between the two signals does not exceed the magnitude of the noise.

B-dependence. As a final trial, the THz pulse transmitted through sample 8 is measured when permanent magnets are used to immerse the sample in a $B = 0.23$ T magnetic field, as shown in Figure 4.4. Once again, there is negligible change in the transmitted pulse.

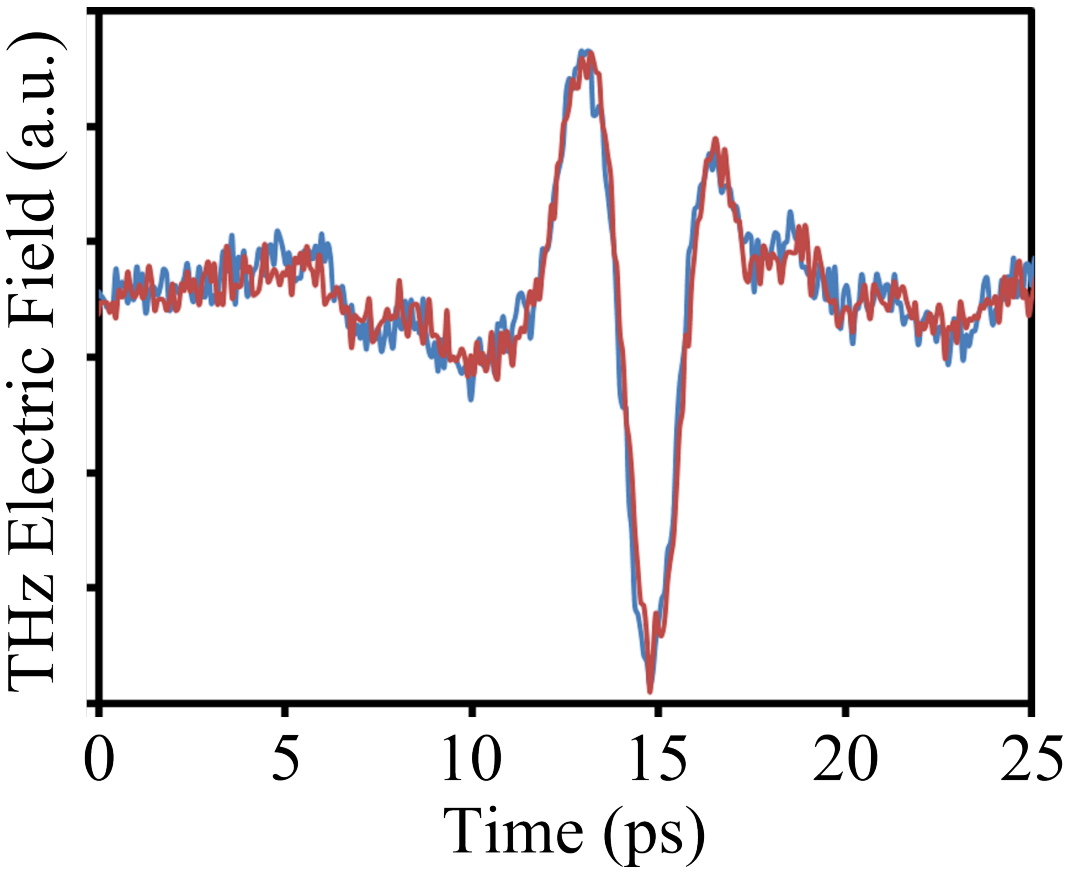

Figure 4.4: Measured THz electric field waveforms for transmission through sample 8 with $B = 0$ and $B = 0.23$ T. The noise has not been filtered out to illustrate that any differences between the two signals does not exceed the magnitude of the noise.

4.3 Discussion

The absence of any detectable B-dependence of the THz transmission may stem from a number of factors. First of all, the microscopic properties of thin metal films are dependent on the quality of the substrate. Rather than being deposited onto a smooth substrate with a well defined crystal plane, the spin valves in this work are deposited onto the comparatively rough Cu particles. Therefore, the thickness of the layers would most likely locally vary across the surface of the particles. Spin valves are extremely sensitive to the layer thicknesses [2] and, accordingly, the non-uniform surface conditions would reduce their performance.

A second possibility can be discerned by considering Figure 4.4, which depicts the transmitted THz pulse for $B = 0.23$ T. Since there is plasmonic current passing from ferromagnetic to non-magnetic metals (and vice-versa), it is reasonable to expect to see traces of spin-accumulation as was observed by Chau [13]. In [13], B-dependent pulse attenuation was observed in the plasmonic enhanced transmission through Au-coated Co microparticles for $B > 100$mT. Since the base particles were ferromagnetic the plasmons consisted of spin polarized current, which was modulated by the interface resistance associated with spin accumulation. For the sample corresponding to Figure 4.4, though, the base particles are non-magnetic and the only sources of spin polarized current are the thin layers of ferromagnetic metal composing the spin valves. The lack of *any* change for the large applied field of 0.23 T indicates that spin-accumulation at the ferromagnetic/non-magnetic interfaces is not affecting the transmitted THz pulse. Thus, it is evident that there is not enough spin polarized current contributing to the plasmonic oscillations for spin-accumulation to manifest in the transmitted THz radiation, which could also explain the lack of observable GMR effects. This explanation is

supported by the fact that the skin depth of metals is typically $\sim$ 100nm at THz frequencies [15], and the $\leq$ 20nm of ferromagnetic material in the spin valves, which were only fabricated on one side of the particles, only constitutes a small percentage of the volume where current densities are generated by the penetrating THz electric fields. Hence, a solution may be to start with a ferromagnetic particle like Co, then deposit a non-magnetic spacer layer followed by second ferromagnetic layer. This method may be limited by the native oxide that would undoubtedly be present on the surface of the Co particles, which could potentially impede current passing from the Co particle to the fabricated metallic layers. However, this could be addressed by removing the oxide layer via ion etch. Moreover, a challenge for implementing this approach is that the ferromagnetic Co particles tend to clump together, thus making it difficult to spread out a single layer of particles for deposition. Due to this limitation, only a small portion of the particles would have spin valves fabricated on them. A second solution may be to implement even higher magnetic field strengths, which would increase the magnetization of the ferromagnetic layers, thereby increasing the amount of spin-polarized current.

4.4 Conclusion

A turning point for electronically driven information technologies was the discovery of spin-dependent transport and GMR. The ability to utilize the spin-states of electrons provided a larger freedom in electronics design, and the greatly enhanced storage capacities introduced by GMR has enabled much of the recent progress in computing technology. Likewise, the newly discovered field of spinplasmonics shows promise, providing a new platform for photonic information technologies in much the same way spintronics did for electronic information technologies. The work presented here takes the works towards

advancing spinplasmonics towards GMR phenomena, however much work still needs to be done. It is interesting to note that after the writing of this thesis, preliminary work by Cameron Straatsma using a newly constructed electromagnet shows evidence of an up to 20% magnetic field dependent reduction in transmitted THz pulse intensity for large magnetic field strengths ($\sim$ 200 mT) using similar samples. The results provide promising evidence of plasmonic giant magnetoresistance.

4.5 Chapter 4 References

[1] W. Thomson, "On the electro-dynamic qualities of metals: Effects of magnetization on the electric conductivity of nickel and of iron," *Proc. R. Soc. London*, vol. 8, pp. 546–550, 1857.

[2] E. Hirota, H. Sakakima, and K. Inomata, *Giant Magneto-Resistance Devices*. Berlin Heidelberg: Springer-Verlag, 2002.

[3] M. Julliere, "Tunneling between ferromagnetic films," *Phys. Lett.*, vol. 54A, pp. 225–226, 1975.

[4] M. Johnson and R. H. Silsbee, "Interfacial charge-spin coupling: Injection and detection of spin magnetization in metals," *Phys. Rev. Lett.*, vol. 55, pp. 1790–1793, 1985.

[5] ——, "Spin-injection experiment," *Phys. Rev. B*, vol. 37, pp. 5326–5335, 1988.

[6] ——, "A thermodynamic analysis of interfacial transport and of the thermomagnetoelectric system," *Phys. Rev. B*, vol. 35, pp. 4959–4972, 1987.

[7] M. Johnson, "Spin polarization of gold films via transported," *J. Appl. Phys.*, vol. 75, pp. 6714–6719, 1994.

[8] M. N. Baibich, J. M. Broto, A. Fert, F. N. V. Dau, F. Petroff, P. Eitenne, G. Creuzet, A. Friederich, and J. Chazelas, "Giant magnetoresistance of (001)Fe/(001)Cr magnetic superlattices," *Phys. Rev. Lett.*, vol. 61, pp. 2472–2475, 1988.

[9] G. Binasch, P. Grunberg, F. Saurenbach, and W. Zinn, "Enhanced magnetoresistance in layered magnetic structures with antiferromagnetic interlayer exchange," *Phys. Rev. B*, vol. 39, pp. 4828–4830, 1989.

[10] K. J. Chau, G. D. Dice, and A. Y. Elezzabi, "Coherent plasmonic enhanced terahertz transmission through random metallic media," *Phys. Rev. Lett.*, vol. 94, no. 173904, 2005.

[11] K. J. Chau and A. Y. Elezzabi, "Terahertz transmission through ensembles of subwavelength-size metallic particles," *Phys. Rev. B*, vol. 72, no. 075110, 2005.

[12] ——, "Photonic anisotropic magnetoresistance in dense co particle ensembles," *Phys. Rev. Lett.*, vol. 96, no. 033903, 2006.

[13] K. J. Chau, M. Johnson, and A. Y. Elezzabi, "Electron-spin-dependent terahertz light transport in spintronic-plasmonic media," *Phys. Rev. Lett.*, vol. 98, no. 133901, 2007.

[14] W. F. Brown, *Handbook of Chemistry and Physics*, Condon and Odishaw, Eds. McGraw-Hill, 1958.

[15] K. J. Chau and A. Y. Elezzabi, "Effect of interface resistance on terahertz pulses in bimetallic microparticles," *Phys. Rev. B*, vol. 73, no. 085419, 2006.

Chapter 5

Evidence of Terahertz Loss Reduction via a Schottky Space-Charge Region

5.1 Background

It is a common phenomenon in research that the pursuit of one research goal may lead to a different discovery entirely. In Chapter 4, Cu particles coated with multilayers of ferromagnetic and nonmagnetic material were investigated, with the goal of observing magnetic dependent THz transmission via GMR. It has been shown that in the context of THz plasmonic enhanced transmission through metallic media, for particles coated with layers of dissimilar metal there is an interface impedance that results in a decrease in transmission amplitude [1, 2]. Hence, the transmission of THz radiation through the particles coated with magnetic multilayers (in zero external magnetic field) was expected to be of lower amplitude than the transmission through the uncoated particles. Unexpectedly, though, an increase of transmission amplitude was observed for most of the samples. To investigate whether this enhancement is manifest due to the ferromagnetic metals present, the situation is simplified by studying Cu particles coated with only a thin layer of Au. In this Chapter the studies performed so far and the future directions of the research are described.

5.2 Experimental Results

To investigate the enhanced transmission effect, Cu particles are partially coated with an Au layer. The relatively large skin depth of Au at THz frequencies ($\sim$ 100 nm [1]) ensures that the external electric field interacts with the interface provided that the Au layer is not too thick. While the physics should be observed in a metallic interface on a single particle, the utilization of many particles (and interfaces) allows any electromagnetic effects arising from the interface to accumulate as the THz pulse is transmitted through the

ensemble of particles.

The Au layer on the Cu particles is formed using off-axis radio frequency (RF) sputtering, and 4 different samples with Au thicknesses, d_{Au}, of 5 nm, 10 nm, 20nm, and 100 nm have been prepared. The fabrication of all the samples tested in this Chapter was performed by Mehmet Egilmez (Thin Films, Multilayers and Nanostructures Laboratory, Department of Physics, University of Alberta). The particles have a mean size of $\delta = 90 \pm 15$ µm, and a scanning electron microscope (SEM) image of a typical particle is shown in Figure 5.1(a). Only the top surface of the particles is exposed to the sputtering flux and, as such, only a portion of the Cu particle surfaces are coated with Au. X-ray photoelectron spectroscopy (XPS) has been used to characterize the average surface composition. The XPS spectra for the samples having $d_{Au} = 5$ nm and $d_{Au} = 100$ nm are shown in Figure 5.2(a). As shown in Figure 5.2(b), the XPS spectra of the two bimetallic samples show no shift of the Au 4f core levels relative to each other. Since the X-ray radiation penetrates several nanometers into the particles, this indicates the absence of Cu/Au alloying near the interface in the $d_{Au} = 5$ nm sample. The percent Au coverage, f_{Au}, is quantified by the relative magnitudes of the characteristic Au 4f and Cu 2p peaks in the XPS spectra where samples with higher Au coverage exhibit larger Au peaks and, correspondingly, smaller Cu peaks. For the bimetallic Cu-core/Au-layer samples, XPS analysis revealed that f_{Au} increases from 21% to 38% as d_{Au} increases from 5 nm to 100 nm. Such a trend is attributed to the nucleation and growth of islands during the thin film deposition process. To characterize the uniformity of the Au coverage, auger electron spectroscopy (AES) is performed, where an image of a region coated with 10 nm of Au is shown in Figure 5.1(b). An SEM image of the same region is shown in Figure 5.1(c). In AES, the sample is exposed to an electron beam and Auger

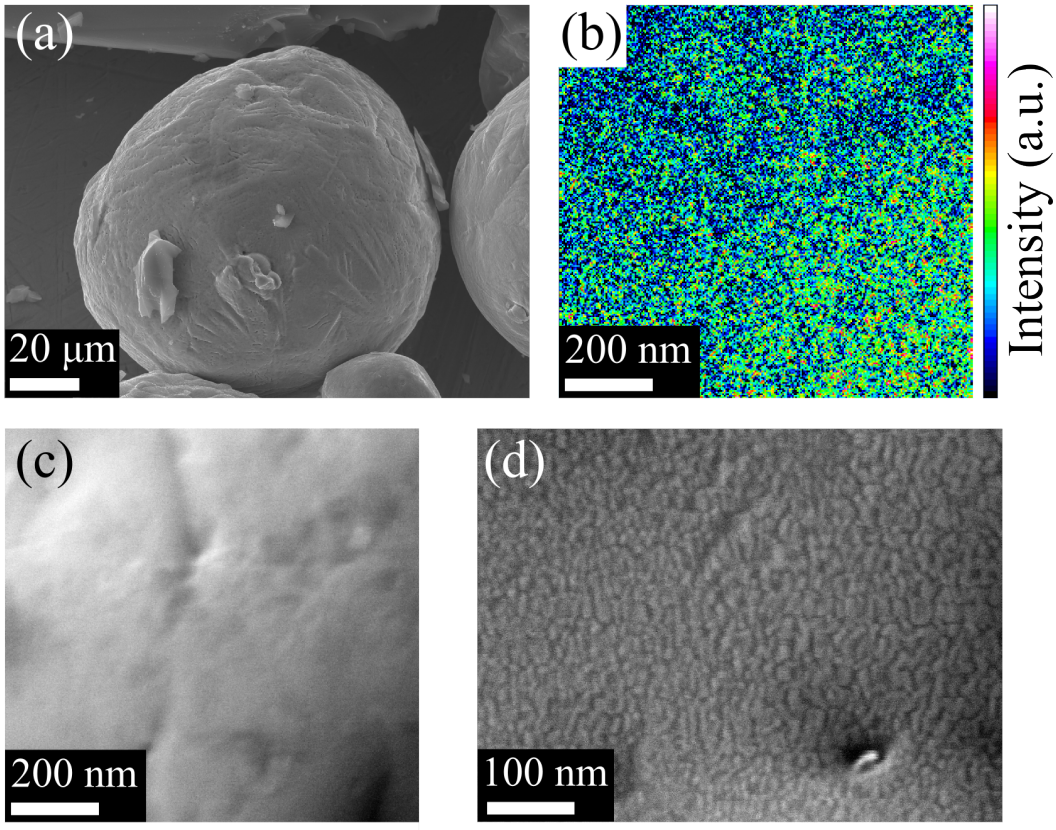

Figure 5.1: Panels (a), (c), and (d) depict a Cu particle coated with 10 nm of Au for various resolutions. Panel (b) depicts the Au coverage of the Cu particle surface via AES, and corresponds to the same region shown in panel (c).

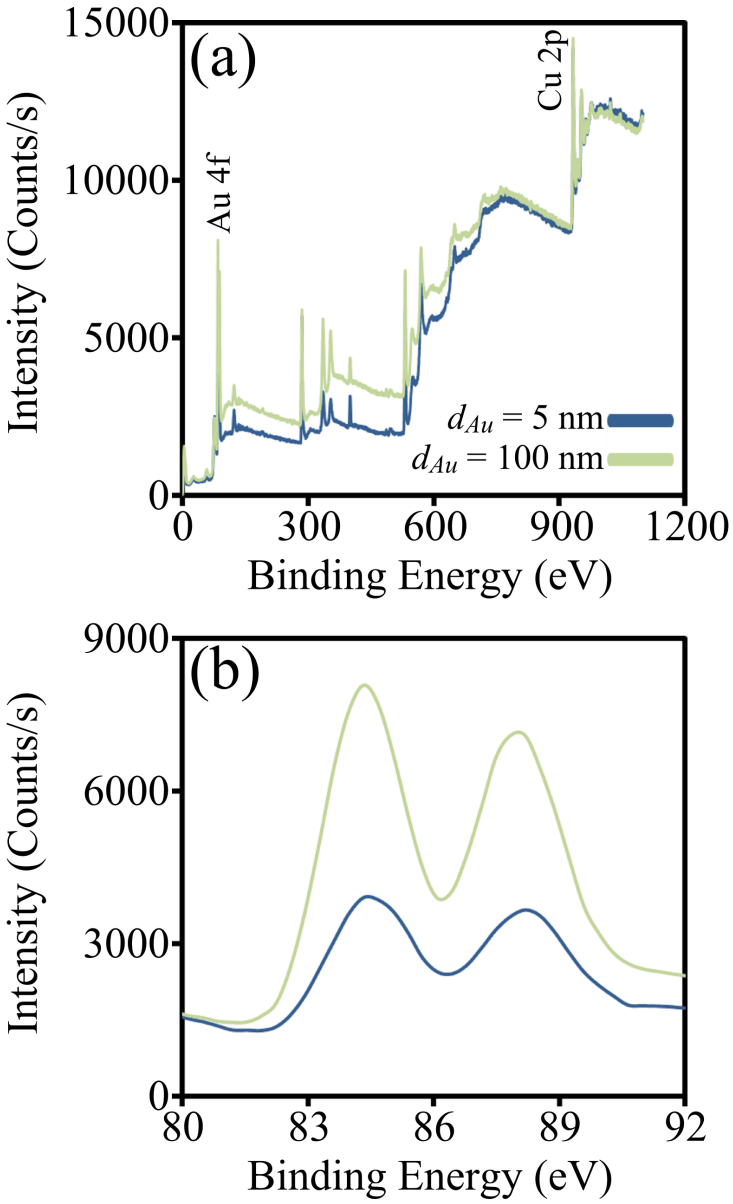

Figure 5.2: (a) XPS spectra of two different Cu particle ensembles having $d_{Au} = 5$ nm and $d_{Au} = 100$ nm, respectively. Panel (b) depicts the XPS spectra for the two samples in the vicinity of the Au 4f emission lines.

electrons are emitted at discrete energies that depend on the element present on the sample surface. In Figure 5.1(c), the intensity is given by $(P - B)/B$, where P is the height of the spectral peak corresponding to Au and B is the background level. Such a definition removes the intensity variation that can be caused by height changes, and thus represents the Au coverage independent of the surface morphology. It is apparent that the surface coverage of the Au is reasonably uniform over the $\sim$ 200 nm resolution of the AES technique. Finally, the topology of the surface is examined using high resolution SEM, as shown in Figure 5.1(d), where it is evident that the Au nucleation forms boundaries $\sim$ 20 nm apart.

The THz transmission through a 1.9 mm thick, random ensemble of Au-coated Cu particles is studied using the system described in Chapter 2. When incident on the ensemble, the THz radiation is transmitted via near-field coupling of non-resonant plasmons [3]. Shown in Figure 5.3(a) is the electric field of the THz pulses transmitted through the particle ensembles. The waveforms are obtained by averaging the transmission for several independent random realizations of each sample, where the sample thickness is held constant. As d_{Au} increases from 5 nm to 100 nm, the transmitted peak-to-peak pulse amplitude markedly decreases by $65 \pm 4\%$. This large reduction in transmission for $d_{Au} = 100$ nm is attributed to interfacial impedance between the Cu and Au regions, which has been shown to drastically decrease THz transmission for f_{Au} 40% [1]. However, the most intriguing aspect in this figure is that with the addition of the 5 nm layer the amplitude of the transmitted pulse *increases* by $12 \pm 4\%$. Interestingly, this enhancement is observed when only 21% of the surfaces are coated with a thickness of gold $d_{Au} << \{\delta, \lambda_{THz}\}$, where $\lambda_{THz} \sim 800$ µm is the center wavelength of the incident THz radiation. Moreover, it is observed that the pulse transmitted through the $d_{Au} = 5$ nm

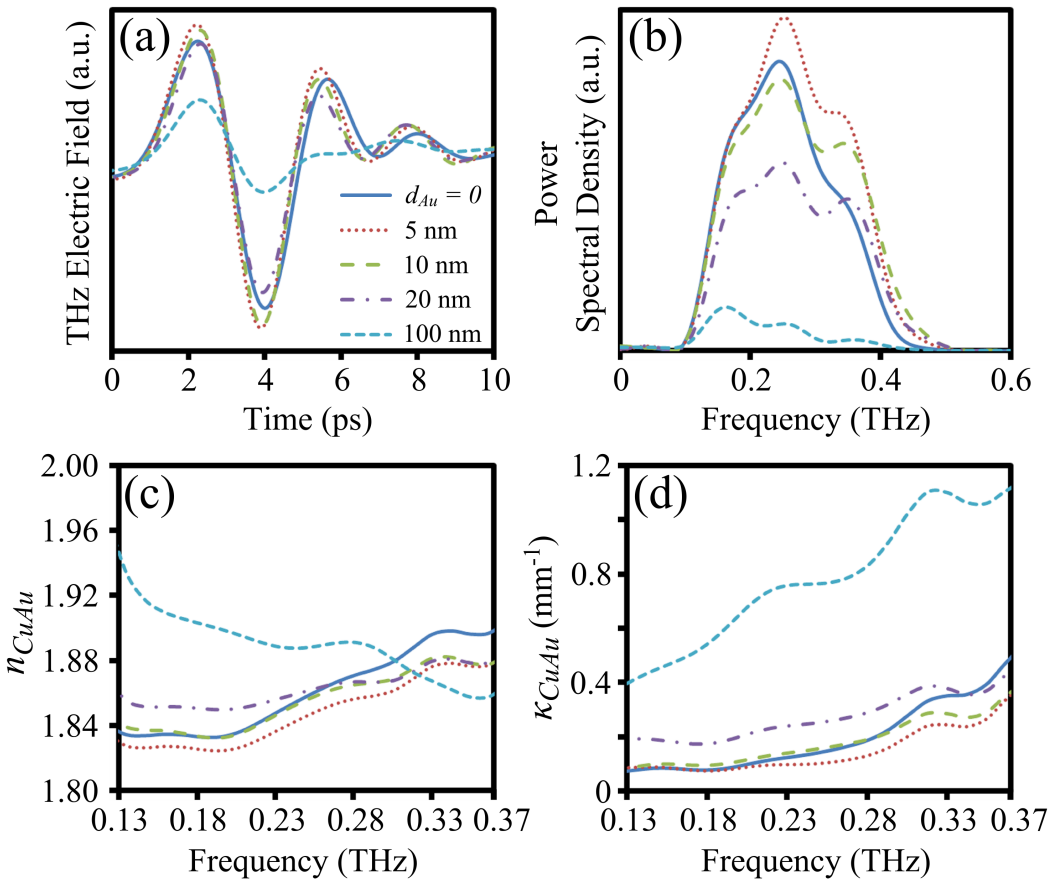

Figure 5.3: The (a) time-domain electric field and (b) power spectral density of THz pulses transmitted through ensembles of Au-coated Cu particles with $d_{Au} = 0$ (solid), 5 nm (dotted), 10 nm (dashed), 20 nm (dash-dotted), and 100 nm (short dash). Panels (c) and (d) depict the effective refractive index, n_{CuAu}, and effective absorption coefficient, κ_{CuAu}, for the same samples, as determined from the pulses shown in (a).

sample has a shorter period (i.e. larger frequency bandwidth) than the pulse transmitted through the non-coated particles. Evidently, the surface conditions of the micro-particles have a profound effect on the plasmonic-enhanced transmission of THz radiation. The spectral characteristics are elucidated by observing the frequency content of the transmitted pulses, as shown in Figure 5.3(b). Here it is revealed that the addition of the 5 nm layer of Au results in a significant enhancement of the high-frequency components, where the enhancement decreases as the frequency decreases. Interestingly, as d_{Au} increases from 5 nm to 20 nm, the amplitude decreases uniformly over the whole bandwidth. For $d_{Au} = 100$ nm, the attenuation is accompanied with a shift of the spectral peak to a lower frequency (0.25 THz for $d_{Au} = 20$ nm compared to 0.16 THz for $d_{Au} = 100$ nm), which is characteristic of attenuation resulting from interface impedance [1]. It should be noted that the spectral modes that are apparent in Figure 5.3(b) arise from the inter-particle geometry [3]. The characteristics of the dominant spectral modes are illustrated by reconstructing the frequency spectra from three Lorentzians using a least squares fit, as depicted in Figure 5.4(a) for $d_{Au} = 5$ nm. The amplitude, width, and center location of each of the Lorentzians is not fixed, but rather, is determined via a least squares approach. The center frequency of the three modes for each sample is shown in Figure 5.4(b), where it is evident that there is no shift in the location of the peaks. This indicates that the packing fraction of the particles is the same for the different samples.

To gain a more thorough understanding of the observed results the effective index of refraction, n_{CuAu}, is calculated, as shown in Figure 5.3(c). Note that the while n_{CuAu} is dielectric-like due to plasmonic coupling between the particles [3, 4], the intrinsic relative permittivity of the individual Cu particles is $\sim -5 \times 10^5 + i10^6$ at 0.4 THz [5]. Nevertheless, it is evident that there is

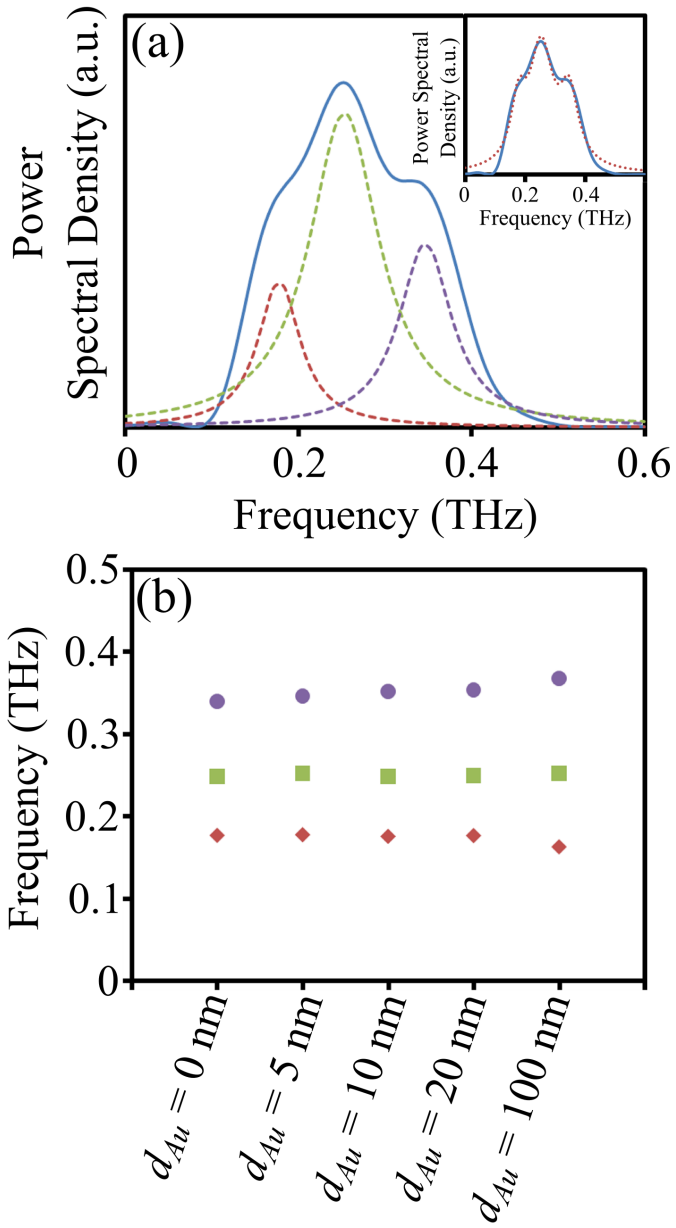

Figure 5.4: (a) The frequency spectrum of the THz pulse transmitted through the sample with $d_{Au} = 5$ nm (solid), and the three Lorentzian curves that can be added together to reconstruct it (dashed). The inset in (a) depicts the experimentally obtained spectrum (solid) together with the sum of the three Lorentzian curves (dotted). Panel (b) depicts the center locations of the Lorentzian curves for the samples with $d_{Au} = 0$, 5 nm, 10 nm, 20 nm, and 100 nm.

little change in n_{CuAu} for $0 \leq d_{Au} \leq 20$ nm ($< 2\%$ change). For $d_{Au} = 100$ nm, n_{CuAu} is increased for frequencies spanning 0.13 THz - 0.30 THz, which agrees with the expected behaviour from the interface impedance between Cu and Au [1]. For the $d_{Au} = 100$ nm sample, a reliable interpretation of n_{CuAu} for frequencies higher than 0.30 THz is precluded since the spectral amplitude of the transmitted pulse is nearly zero for frequencies above 0.30 THz [Figure 5.3(b)]. Figure 5.3(c) depicts the effective absorption coefficient, κ_{CuAu}, of the samples, where the value of κ_{CuAu}^{-1} signifies the e^{-1} decay length of the transmitted electric field. In the calculation of κ_{CuAu} it has been assumed that the reflectivity of the overall ensemble does not change with the addition of the thin layer of Au since the reflectivities of Cu and Au are nearly identical at THz frequencies. Interestingly, at a frequency of 0.37 THz the addition of the 5 nm layer results in a 28% decrease in κ_{CuAu} with respect to the non-coated particles, and the amount of attenuation decreases to zero relative change as the frequency decreases to 0.13 THz. As d_{Au} increases from 5 nm to 20 nm, κ_{CuAu} increases relatively uniformly over the whole bandwidth. For $d_{Au} = 100$ nm, the increasing value of κ_{CuAu} for increasing frequency reflects the shift of the peak frequency of the transmitted pulse spectrum to a lower value. Since the absorption is positive for all d_{Au}, though, the apparent "enhancement" of the the transmitted signal amplitude for $d_{Au} = 5$ nm is more appropriately referred to as a *decrease in loss*.

It is important to address the fact that the observed results are highly dependent on the band structure of the metals forming the interface. As such, a rich dependence on the choice of materials is expected. Interestingly, Au and Pt have particularly similar band structure [6], and accordingly, a similar series of experiments is performed using Pt layers to test whether Pt exhibits a comparable response. The experimental and analytical procedure is analogous

to the Au layer study, and the Pt layer thicknesses explored, d_{Pt}, were 5 nm, 10 nm, 20 nm, 50 nm, and 100 nm. For the bimetallic Cu-core/Pt-layer samples, the percent Pt coverage, f_{Pt}, increases from 37% to 61% as d_{Pt} increases from 5 nm to 100 nm. As shown in Figure 5.5, the results are similar to those obtained for Au, albeit with less loss reduction for $d_{Pt} = 5$ nm.

It is noteworthy to mention that the Cu particles are undoubtedly coated with a thin oxide layer, since Cu readily oxidizes in air. Hence, when the Au layer is deposited on the Cu particles, there is a thin layer of native oxide between the pure Cu and the Au. To investigate the role the native oxide plays on the transmission, a sample is prepared where 200 nm of Cu is first deposited onto the particles, followed by 5 nm Au without breaking vacuum. As a result, the interface between the 200 nm layer of Cu and 5 nm layer of Au does not have a native oxide present. The thick, 200 nm layer of Cu prevents the possibility of any interaction of THz radiation with the interface between the native oxide and the Cu layer, since the skin depth of Cu is $\sim$ 100 nm at THz frequencies [2]. Moreover, it has been shown that with only a 40 nm layer of Cu on native-oxide coated Cu particles, there is negligible change in the transmission of THz radiation through dense ensembles of the particles [1]. Also prepared is a sample with a 100 nm layer of Au deposited onto a 200 nm layer of Cu. The time-domain waveforms and frequency spectra of the THz transmission through uncoated Cu particles and the two aforementioned samples are shown in Figures 5.6(a) and 5.6(b), respectively. Remarkably, it can be seen that the previously observed enhancement is no longer evident in the sample with the 5 nm layer of Au. However, the sample with the 100 nm layer of Au still shows the attenuation characteristic to contact impedance. Thus, the experimental results suggest that the native oxide layer is responsible for the decreased losses for the high frequency components. The fact that the

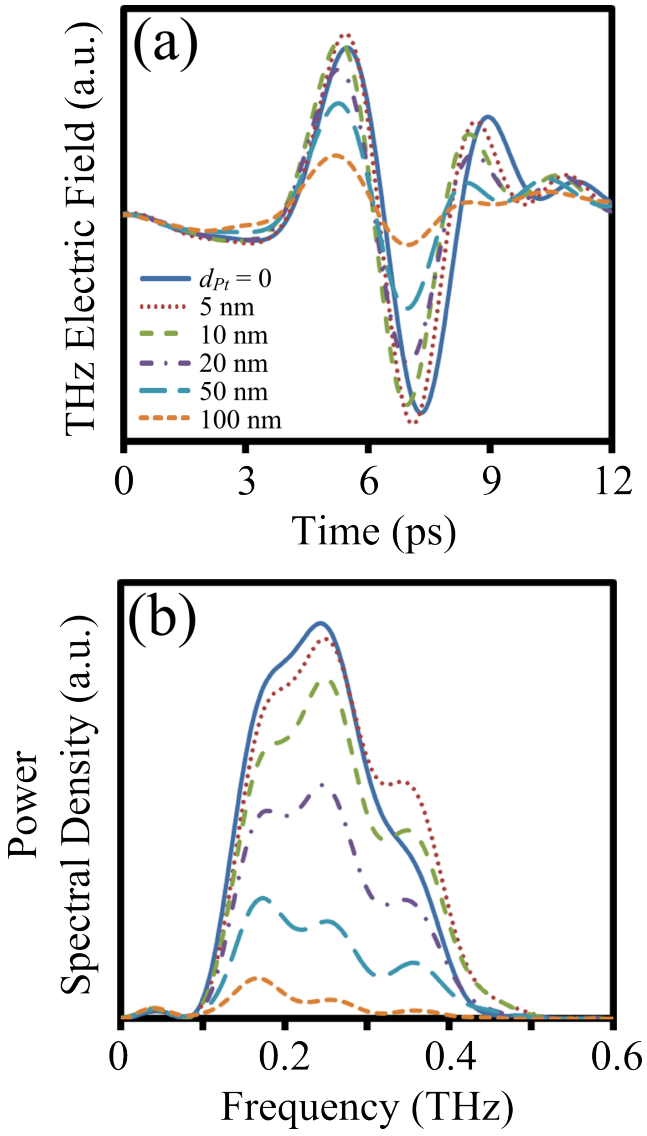

Figure 5.5: The (a) time-domain electric field and (b) power spectral density of THz pulses transmitted through ensembles of Pt-coated Cu particles with $d_{Pt} = 0$ (solid), 5 nm (dotted), 10 nm (dashed), 20 nm (dash-dotted), 50 nm (long dash), and 100 nm (short dash).

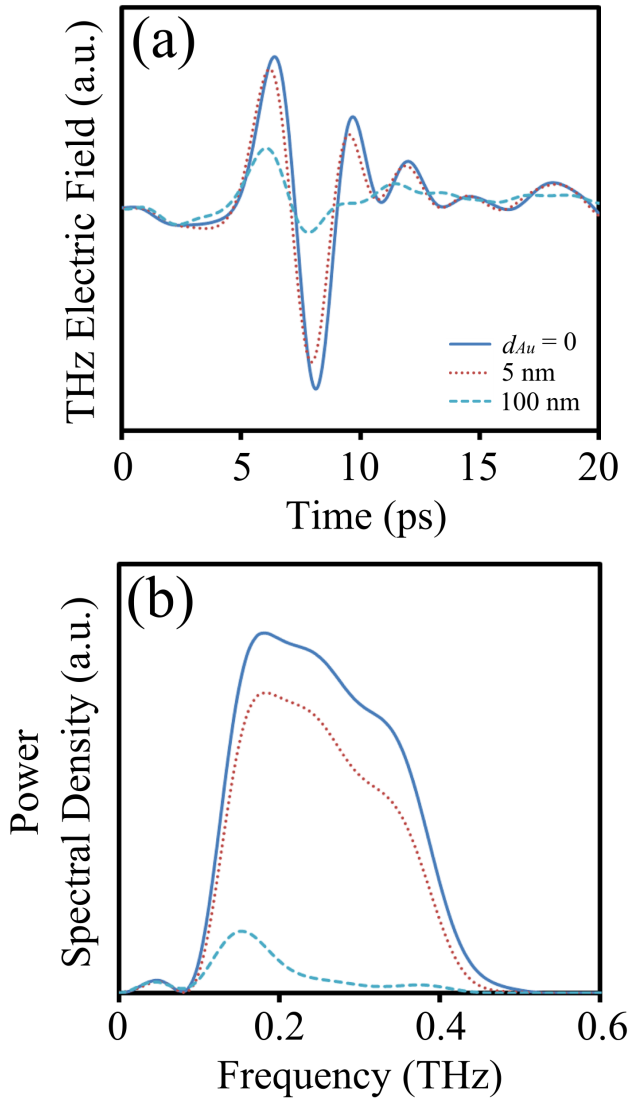

Figure 5.6: The (a) time-domain electric field and (b) power spectral density of THz pulses transmitted through ensembles of uncoated Cu particles (solid) and Cu particles coated with 200 nm of Cu followed by 5 nm of Au (dotted) and 100 nm of Au (dashed).

decrease in loss diminishes as d_{Au} is increased suggests that either the oxide layer is able to drastically alter the optical response of the Au layer when d_{Au} is small, or that the effect strongly depends on the strength of the electric field at the interface. The latter possibility can be considered because as d_{Au} increases the interface is buried deeper in the particle, and the electric field perceived by the interface decreases with a skin depth ~ 100 nm in Au at THz frequencies [1].

To confirm that the high frequency loss reduction occurs due to the oxide layer, a sample of Cu particles is annealed in air for 4 minutes at 300° C to increases the thickness of the oxide layer. Such conditions lead to an oxide thickness of approximately 50 nm. Shown in Figure 5.7(a) is the time-domain THz transmission through a non-annealed sample with $d_{Au} = 0$, an annealed sample with $d_{Au} = 0$, an annealed sample with $d_{Au} = 5$ nm, and an annealed sample with $d_{Au} = 20$ nm. Figure 5.7(b) depicts the corresponding frequency spectra. Interestingly, the addition of the 5 nm layer of Au results in decreased loss for the high frequency components, similarly to the non-annealed Cu particles with a 5 nm layer of Au. The overall decreasing amplitude of the transmission for $d_{Au} = 20$ nm is also consistent with the earlier results. As such, the experimental results provide strong evidence that the high frequency loss-reduction effect stems from an interaction of the native copper oxide layer with the Au layer.

5.3 Discussion

A possible explanation for the observed results may lie in the fact that CuO and Cu_2O are p-type semiconductors with band gaps of 1.4 eV and 2.2 eV, respectively [7]. Bringing a metal into contact with a semiconductor results in the bending of energy bands and the creation of a space charge region in

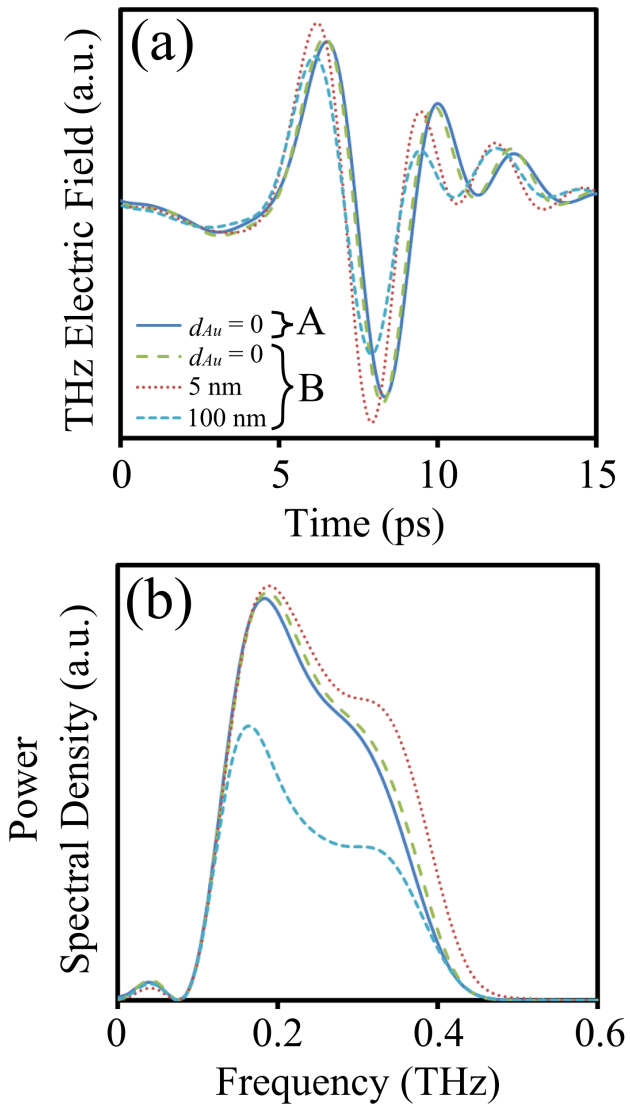

Figure 5.7: The (a) time-domain electric field and (b) power spectral density of THz pulses transmitted through a non-annealed Cu sample with $d_{Au} = 0$ (solid), an annealed sample with $d_{Au} = 0$ (dashed), an annealed sample with $d_{Au} = 5$ nm (dotted), and an annealed sample with $d_{Au} = 20$ nm (tight dashed). The label "A" in the legend refers to non-annealed particles while the label "B" in the legend refers to particles that are annealed before the deposition of Au.

the semiconductor, which is illustrated in a simplified manner that neglects surface states for a p-type semiconductor by Figure 5.8. As depicted in Figure 5.8(a), before contact the Fermi levels in the metal and semiconductor are not aligned. When the work function of the metal, Φ_m, is less than the work function of the semiconductor, Φ_s, a Schottky contact is formed. Upon contact, electrons flow from the metal to the semiconductor and the Fermi levels align to achieve thermal equilibrium. Since the p-type acceptor atoms introduce empty electron states (i.e. holes) near the Fermi level, electrons from the metal are able to occupy these states near the interface (in the semiconductor). It can be determined from Poisson's equation that this space charge region in the semiconductor results in the bending of the energy bands such that a potential barrier of height $\Phi_B = \Phi_s - \Phi_m$, as shown in Figure 5.8(b) [8]. This downward bending of the energy bands represents a barrier to conduction because holes are the majority carriers of current in a p-type semiconductor. In practice, the magnitude of the Schottky barrier is determined by the work functions of the metal and semiconductor as well as their surface states. In fact, it has been shown that despite the fact that the work function of Au is higher than the work function of CuO, an Au-CuO interface can form a Schottky barrier due to the surface states dominating the interfacial interaction when the material dimensions are on the nano-scale [9]. If $\Phi_s < \Phi_m$, as depicted in Figure 5.8(c), an ohmic contact is realized. In this case thermal equilibrium is reached via the transfer of electrons to the metal from the valence band of the semiconductor, and the energy bands bend upwards in the semiconductor near the interface. As shown in Figure 5.8(d), in this scenario there is no potential barrier for the majority carriers in the semiconductor.

It is important to note that the space charge in the semiconductor attracts a surface charge in the metal, which can be represented by an image charge.

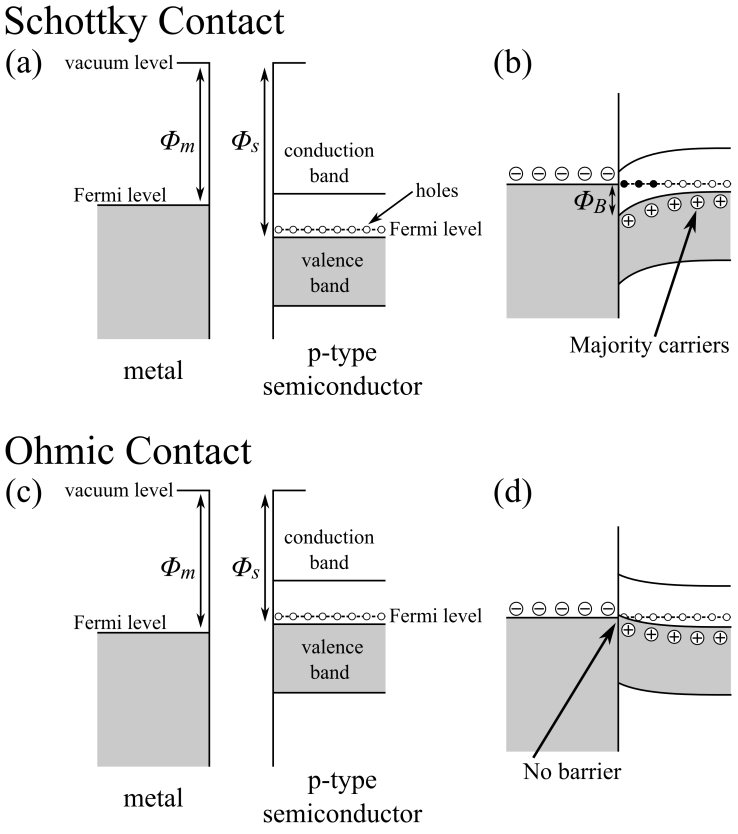

Figure 5.8: Illustration of the band structure of a metal and p-type semiconductor (a) before and (b) after contact. Before contact, the Fermi levels are not aligned. After contact the Fermi levels align, but electrons remain in the holes provided by the acceptor impurities. This results in a depletion region near the interface which in known as the Schottky barrier.

Therefore, a dipolar electric field exists in the semiconductor. Now consider exposing such a system to a transient electric field. An external electric field would upset the equilibrium of the space charge region in the semiconductor since the potential associated with the electric field would cause the energy bands to tilt. As a result, electrons would re-distribute themselves, and the dipolar electric field in the semiconductor would be modified. It is a well known result of Maxwell's equations that an oscillating dipole results in the generation of electromagnetic radiation [10]. Accordingly, it is intuitive to attribute the enhanced THz transmission that is observed for small Au or Pt thicknesses to an upset of the equilibrium of the space charge region at the metal-semiconductor interface followed by a high frequency ringing of the interface collective charge distribution as it settles back into equilibrium. For d_{Au} much less than the skin depth there are low enough dissipative losses for the radiation propagating from the interface to escape. As d_{Au} increases the THz electric field at the interface decreases and the space charge region is not as strongly perturbed. Moreover, as d_{Au} increases the radiation exiting from the interface experiences more loss, thus explaining the diminishing transmission efficiency experimentally observed for increasing d_{Au}. As noted earlier, the substantial decrease in transmission amplitude for $d_{Au} = 100$ nm, which was observed for all samples, is attributed to interface impedance. For the sample with no oxide layer between the Cu and Au, the interface impedance stems from the difference in work functions of the two metals [1]. When two different metals are brought into contact, the difference in their work functions (Φ_1 and Φ_2) results in a flow of electrons from one metal to another, and as charge builds up a "contact potential" is formed at the interface which inhibits the continued transfer of electrons [11], as illustrated by Figure 5.9. This potential difference scatters conduction electrons, giving rise to an interface resistance

[12].

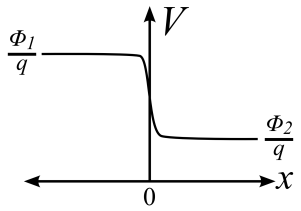

Figure 5.9: Schematic of (a) the potential (V) at an interface between to dissimilar metals. Φ_1 and Φ_2 are the work functions of the two metals, the interface is located at position $x = 0$, and q is the electron charge.

For a metal-semiconductor contact, the Schottky barrier (i.e. Φ_B) results in an interface impedance. Therefore, there is a competition between the transmission enhancement associated with re-emitted radiation from the space-charge oscillations and the transmission attenuation associated with the interface impedance. For $d_{Au} = 5$ nm, enough dipole-generated radiation escapes from the interface escapes to overcome the effects of the interface resistance; however, for $d_{Au} = 100$ nm, the electronic state of the interface is not strongly perturbed and the interface resistance dominates the response.

5.4 Conclusion

While the Schottky space-charge argument provides an appealing explanation to the observed results, additional experiments are required to help provide a more detailed understanding of the mechanisms responsible. Future work that can be done includes removing the oxide layer *in situ* via ion etch before the Au is deposited to confirm that the observed results are indeed due to the native oxide layer. Furthermore, testing various combinations of materials could shed light on the nature of the observed results. In particular, fabricating particles with an interface between a doped semiconductor and metal that are known to form a large Schottky barrier could shed some light on whether the

metal-semiconductor interface is responsible for the loss reduction. Moreover, comparing the results to particles with an interface between a semiconductor and metal that are known to form a small Schottky barrier or ohmic contact could help to confirm whether the metal-semiconductor interface is responsible for the loss reduction.

5.5 Chapter 5 References

[1] K. J. Chau and A. Y. Elezzabi, "Effect of interface resistance on terahertz pulses in bimetallic microparticles," *Phys. Rev. B*, vol. 73, no. 085419, 2006.

[2] K. J. Chau, K. M. Rieckmann, and A. Y. Elezzabi, "Subsurface probing of terahertz particle plasmons," *Appl. Phys. Lett.*, vol. 90, no. 131114, 2007.

[3] K. J. Chau, G. D. Dice, and A. Y. Elezzabi, "Coherent plasmonic enhanced terahertz transmission through random metallic media," *Phys. Rev. Lett.*, vol. 94, no. 173904, 2005.

[4] K. J. Chau and A. Y. Elezzabi, "Terahertz transmission through ensembles of subwavelength-size metallic particles," *Phys. Rev. B*, vol. 72, no. 075110, 2005.

[5] M. A. Ordal, "Optical properties of fourteen metals in the infrared and far infrared: Al, Co, Cu, Au, Fe, Pb, Mo, Ni, Pd, Pt, Ag, Ti, V, and W." *Appl. Opt.*, vol. 24, pp. 4493–4499, 1985.

[6] K. A. Mills, R. F. Davis, S. D. Kevan, G. Thornton, and D. A. Shirley, "Angle-resolved photoemission determination of λ-line valence bands in pt and au using synchrotron radiation," *Phys. Rev. B*, vol. 22, pp. 581–592, 1980.

[7] J. Ghijsen, L. H. Tjeng, J. van Elp, H. Eskes, J. Westerink, G. A. Sawatzky, and M. T. Czyzyk, "Electronic structure of cu_2o and cuo," *Phys. Rev. B*, vol. 38, pp. 1122–1130, 1988.

[8] C. Kittel, *Introduction to Solid State Physics*, 8th ed. Wiley, 2005.

[9] G. Cheng, S. Wang, K. Cheng, X. Jiang, L. Wang, L. Li, Z. Du, and G. Zou, "The current image of a single cuo nanowire studied by conductive atomic force microscopy," *Appl. Phys. Lett.*, vol. 92, no. 223116, 2008.

[10] D. J. Griffiths, *Introduction to Electrodynamics*, 3rd ed. New Jersey: Prentice Hall, 1999.

[11] N. W. Ashcroft and N. D. Mermin, *Solid State Physics*. Philadelphia: Saunders College, 1976.

[12] L. A. Moraga, "Theory of electrical transport and scattering at a metal-metal interface," *J. Phys.: Condens. Matter*, vol. 2, pp. 3777–3795, 1990.

Chapter 6

Conclusion

6.1 Concluding Statements

In Chapter 2 a system capable of angular- and time-resolved, polarization sensitive detection of THz radiation with detection angles spanning 360° was presented. The realization of a pump-probe spectroscopy system capable of time- and polarization-resolved detection at arbitrary angles is challenging, however, since the sampling probe beam must retain its alignment, polarization, and timing for all detection angles. To address these requirements, the detection components are located on a rotatable stage above the THz generation components such that by rotating the stage different angles of detection are realized. A trade-off between angular resolution and SNR is identified, and an adjustable aperture is implemented to allow control over it. The performance of the off-axis system was experimentally validated by measuring the THz pulses scattering from a small metallic sphere, where the results were found to be similar to predictions obtained from FDTD simulations.

In Chapter 3 a class of active artificial materials composed of a random combination of dielectric and ferromagnetic microparticles was discussed. The transmission through the devices is enabled by the near-field coupling of non-resonant plasmons between ferromagnetic particles, and the active behaviour stems from an interplay between engineered position dependent phase accumulation via the relative concentrations of the dielectric and ferromagnetic particles and actively adjustable phase accumulation via photonic anisotropic magnetoresistance. Applying a uniform external magnetic field remodels the spatial dependence of the effective refractive index, which allows for the active adjustment of device behaviour. Recipes to create both an active lens and active router were provided, where in the former case the application of an external magnetic field results in in a tunable focal length, while in the latter case an external magnetic field results in a tunable deflection angle of

transmitted radiation. The passive operation of the devices was investigated via FDTD calculations, and the active operation was verified via the experimental study of an active directional router. In the experimental study, active tuning of the propagation direction of the THz radiation over a range of 5° was demonstrated. Moreover, the experimental results enabled a prediction of a similarly created active lens, where the focal length was estimated to be adjustable from 15 mm to 121 mm. Notably, while these two examples demonstrate the functionality and versatility of this class of devices, they are not the only possibilities since any arbitrary spatial dependence of the effective refractive index can be realized by controlling the relative amounts of metallic and dielectric particles. While the work in this thesis introduces and proves the concept of this type of active THz device, there is still much research potential. An important extension to this work would be to explore ultrafast operation of the devices by implementing magnetic pulses. The minimum pulse duration and strength needs to be explored, which would be an important consideration for applications. Also important for preparing this technology for applications is the optimization of the performance of the devices. It was estimated that the maximum deflection and for a directional router and minimum focal length for a lens were 20° and 3.2 mm, respectively. While these values are encouraging, the use of different materials or fabrication methods could provide superior results that are not embodied in the predictions. Finally, the experimental realization of other specific devices could be explored, such as the active lens or an active diffraction grating.

In Chapter 4, the possibility of modulating the THz transmission through dense ensembles of metallic particles via giant magnetoresistance was explored. Metallic multilayers resembling pseudo-spin valves were fabricating onto copper microparticles, with the goal being that the plasmonic current excited by

the THz radiation would be modulated by GMR. The experimental results suggest that observing such phenomena requires either large magnetic fields or carefully prepared surface conditions. Moreover, electrical GMR has a rich dependence on surface conditions, materials chosen, and fabrication methods. Thus, other sample preparation methods and material types should be explored using a wide range of magnetic field strengths. In particular, the deposition of spin valves onto ferromagnetic particles rather than non-magnetic particles should be investigated.

In Chapter 5, a form of loss reduction for the transmission of THz radiation through ensembles of particles via near-field plasmonic coupling is introduced. For a THz pulse transmitted through a dense ensemble of copper particles that are coated with a nano-layer of gold, it was shown that a gold film only several nanometers thick results in a reduction of the losses for the high frequency components. Interestingly, the experimental results suggest that the effect stems from the existence of a native oxide layer between the copper particle and gold layer. While these results are intriguing, work needs to be done to elucidate the underlying physics responsible for them.

APPENDICES

A. Terahertz Time Domain Spectroscopy Analysis Techniques

Frequency Dependent Optical Parameters

In this section, a method to extract the frequency-dependent wave vector amplitude, $\tilde{k}$, and permittivity, $\tilde{\epsilon}$, from experimental THz-TDS data will be presented. As discussed in Chapter 2, the voltage measured during EO detection is proportional to the time-domain THz electric field, $E(t)$. To extract frequency dependent information, the complex Fourier spectra, $E(f)$, given by

$$E(f) = A(f)e^{i\Phi(f)} \tag{A.1}$$

is first obtained from the Fourier transform of $E(t)$, where $f = \omega/2\pi$ is the frequency, $A(f)$ is the amplitude spectra, and $\Phi(f)$ is the phase spectra. Note that while $E(f)$ is complex-valued, $A(f)$ and $\Phi(f)$ are real-valued.

Now consider the situation where a THz pulse with electric field $E(f) = E_o e^{i(\tilde{k}z - 2\pi ft + \Phi_o)}$ is transmitted through a sample of thickness d_s, where E_o and Φ_o are the amplitude and phase of the pulse when it is first incident on the sample, and $\tilde{k} = k + i\kappa$ is the complex wave vector amplitude. Here it is assumed that there is no variation of the electric field in the x- and y-directions and that the propagation direction is along the z-direction. The behaviour of the pulse as it passes through the sample is dictated by $\tilde{k}$, as discussed in Section 1.3.1. Moreover, at each of the two interfaces between the sample and air, a portion of the pulse is reflected while a portion is transmitted, where the fraction transmitted is given by T. Therefore, the electric field of the pulse as it exits the sample is given by $E(f) = E_o T^2 e^{-\kappa d} e^{i(kd_s - 2\pi ft + \Phi_o)}$. Since k, κ, E_o, Φ_o, and T are all unknown parameters, k and κ can not be

determined from a single measurement. Therefore, the situation depicted in Figure A.1 is implemented, where the THz signals transmitted through two different samples having thicknesses of $d_{s,1}$ and $d_{s,2}$ are measured, respectively, where $d_{s,2} > d_{s,1}$. Accordingly, the electric fields at the detector for the two cases are given by

$$E_1(f) = E_o T^2 e^{-\kappa d_{s,1}} e^{i(kd_{s,1} + k_{air}(d_{s,2} - d_{s,1}) + k_{air} d_m - 2\pi f t + \Phi_o)} \propto A_1(f) e^{i\Phi_1(f)} \tag{A.2a}$$

$$E_2(f) = E_o T^2 e^{-\kappa d_{s,2}} e^{i(kd_{s,2} + k_{air} d_m - 2\pi f t + \Phi_o)} \propto A_2(f) e^{i\Phi_2(f)} \tag{A.2b}$$

where $k_{air} \approx 2\pi f/c$ is the wave vector in air, d_m is the distance to the detector (Figure A.1), and A_1, A_2, Φ_1, and Φ_2 are the experimentally acquired data sets. Hence, k can be isolated by determining the phase difference, $\Phi_2 - \Phi_1$, and κ can be isolated by determining the amplitude ratio, A_2/A_1 which yields

$$k(f) = \frac{\Phi_2(f) - \Phi_1(f)}{d_{s,2} - d_{s,1}} + \frac{2\pi f}{c} \tag{A.3a}$$

$$\kappa(f) = -\frac{1}{d_{s,2} - d_{s,1}} \ln\left(\frac{A_2(f)}{A_1(f)}\right) \tag{A.3b}$$

Notably, with $\tilde{k}(f)$ experimentally determined via Equations (A.3a) and (A.3b), one can determine $\tilde{\epsilon}(f)$ by using the relation $\tilde{k} = \sqrt{2\pi\mu_o\mu\epsilon_o\tilde{\epsilon}f}$. Also, it should be noted that the index of refraction, $n(f)$, can be calculated using $n = kc/2\pi f$.

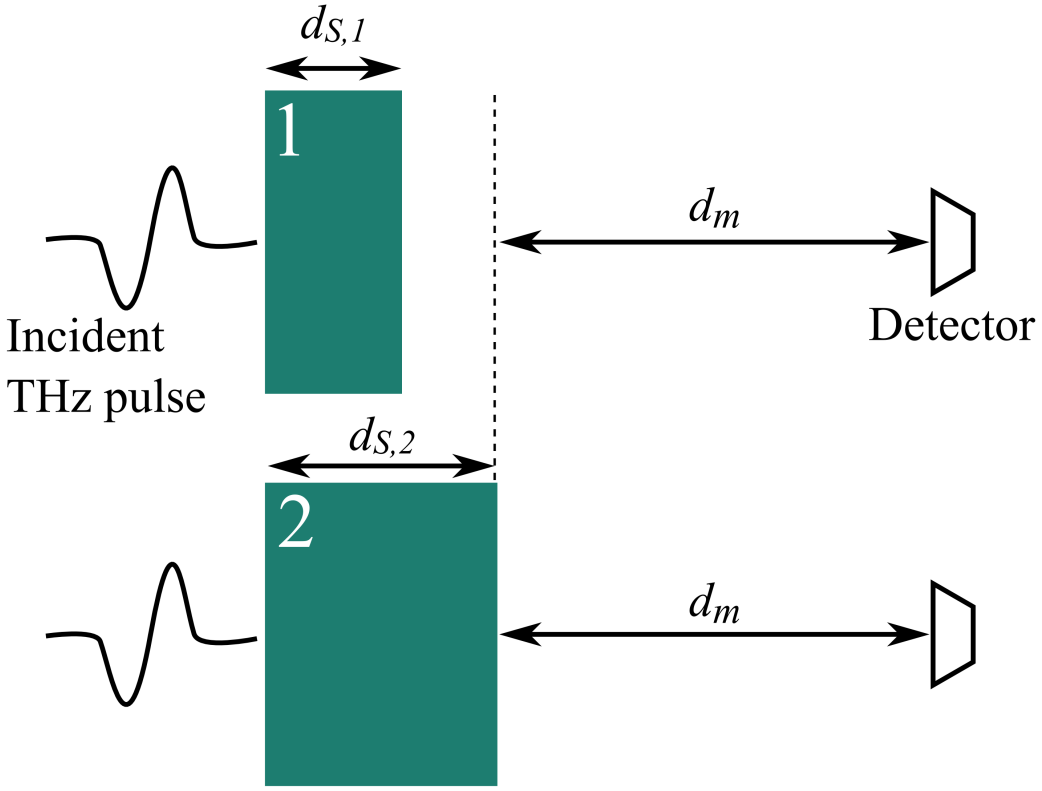

Figure A.1: Schematic of the experimental procedure, where the pulses transmitted through two different samples (1 and 2) having thicknesses of $d_{s,1}$ and $d_{s,2}$, respectively, are measured using THz-TDS. The distance between sample 1 and the detector is $d_m + d_{s,2} - d_{s,1}$ while the distance between sample 2 and the detector is d_m

Error Considerations in the Fast Fourier Transform Algorithm

In the analysis of the time-domain waveforms obtained via THz-TDS, the Fourier transform is routinely used to obtain the spectral characteristics. The discrete signal obtained through the THz-TDS, $f(n)$, is composed of N values, where the corresponding time for each value is $n\Delta t$, and Δt is the time between samples. The discrete Fourier transform of $f(n)$ is given by

$$\begin{aligned} F(k) &= F_R(k) + iF_I(k) \\ &= \sum_{n=0}^{N-1} f(n) \cos \frac{2\pi kn}{N} + i \sum_{n=0}^{N-1} f(n) \sin \frac{2\pi kn}{N} \end{aligned} \tag{A.4}$$

where F_R and F_I are real and imaginary parts of the Fourier transform, respectively. If one considers every element of $f(n)$ to be independent with a variance σ_f^2, then the variance of F_R and F_I are given by

$$\sigma_{F_R}^2 = \sigma_f^2 \left(\frac{\partial F_R}{\partial f} \right)^2 = \sigma_f^2 \sum_{n=0}^{N-1} \cos^2 \frac{2\pi kn}{N} \tag{A.5a}$$

$$\sigma_{F_I}^2 = \sigma_f^2 \left(\frac{\partial F_I}{\partial f} \right)^2 = \sigma_f^2 \sum_{n=0}^{N-1} \sin^2 \frac{2\pi kn}{N} \tag{A.5b}$$

Interestingly, for $0 < k < (N-1)/2$ and $N >> 0$, the summations in Equations (A.5) simplify to $N/2$ [1]. Moreover, for the THz waveforms investigated in this thesis the zero-frequency components and frequency content near the Nyquist frequency (i.e. frequency where $k = (N-1)/2$) are absent, and for simplicity, the error for $k = 0$ and $k = (N-1)/2$ will be ignored. As such, one can simply write

$$\sigma_{F_R}^2 = \sigma_{F_I}^2 = \frac{\sigma_f^2 N}{2} \tag{A.6}$$

[1] This can be easily proven by approximating the summation as an integral, which is valid for $N >> 0$.

Typically the amplitude, $A(k) = \sqrt{F_R^2 + F_I^2}$, and phase, $\phi(k) = \arctan \frac{F_I}{F_R}$, spectra are computed which have variance's given by

$$\sigma_A^2 = \sigma_{F_R}^2 \left(\frac{\partial A}{\partial F_R} \right)^2 + \sigma_{F_I}^2 \left(\frac{\partial A}{\partial F_I} \right)^2 + \sigma_{F_R F_I}^2 \frac{\partial A}{\partial F_R} \frac{\partial A}{\partial F_I} \tag{A.7a}$$

$$\sigma_\phi^2 = \sigma_{F_R}^2 \left(\frac{\partial \phi}{\partial F_R} \right)^2 + \sigma_{F_I}^2 \left(\frac{\partial \phi}{\partial F_I} \right)^2 + \sigma_{F_R F_I}^2 \frac{\partial \phi}{\partial F_R} \frac{\partial \phi}{\partial F_I} \tag{A.7b}$$

respectively, where $\sigma_{F_R F_I}^2$ is the covariance between F_R and F_I. The covariance can be written as

$$\begin{aligned} \sigma_{F_R F_I}^2 &= \sigma_f^2 \frac{\partial F_R}{\partial f} \frac{\partial F_I}{\partial f} \\ &= \sigma_f^2 \sum_{n=0}^{N-1} \cos \frac{2\pi k n}{N} \sin \frac{2\pi k n}{N} \\ &= \frac{\sigma_f^2}{2} \sum_{n=0}^{N-1} \sin \frac{4\pi k n}{N} \end{aligned} \tag{A.8}$$

Fortunately, $\sigma_{F_R F_I}^2$ vanishes because the summation is over an integer multiple of periods of a sine function. As such, the following expressions for the errors can be deduced to be

$$\sigma_A^2 = \frac{\sigma_f^2 N}{2} \tag{A.9}$$

$$\sigma_\phi^2 = \frac{\sigma_f^2 N}{2A^2} \tag{A.10}$$

While these expressions are applicable for the fast Fourier transform algorithm, it is important to note that N is the number of points in the time domain waveform *excluding the points appended for zero padding.* This is because $\sigma^2 = 0$ for the padding zeros and, as such, they do not contribute to the total error.

B. Electromagnet Design

The schematic for a compact electromagnet is shown in Figure A.2. The spools, which have wire coiled around them, have variable separation to allow the accommodation of various sample sizes. The two spools are fabricated from iron to enhance the magnetic field generated, while the rest of the pieces are fabricated from aluminum to avoid distortion of the magnetic field.

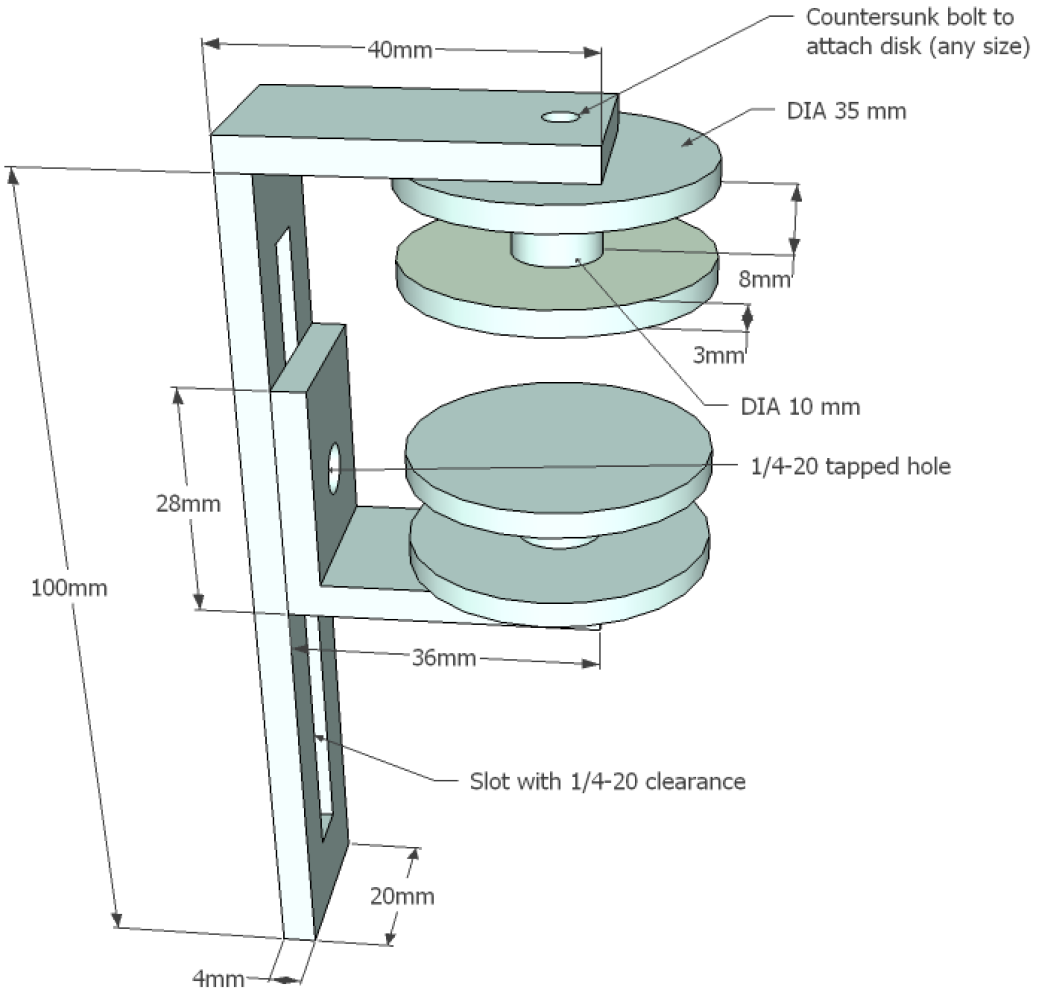

Figure A.2: Schematic for an electromagnet.

C. Finite-Difference Time-Domain Calculations

To numerically solve Maxwell's equations, a commonly used technique is the finite difference time domain (FDTD) method. In this method, the simulation space is composed of a uniform grid of pixels, where the material properties at each pixel are specified. An electromagnetic source is excited by defining a line of electric field at time zero, and as time steps are uniformly increased via the advancement of time-steps the electrodynamics play out. While this technique tends to require more computational resources than others (e.g. finite element method), it is advantageous due to the ability to easily modify the material parameters.

The two-dimensional (2D) FDTD algorithm used in the thesis work will be described. In the 2D assumption, the z-derivatives of all the electric and magnetic fields can be set to zero in Maxwell's equations, which yields two sets of mutually exclusive equations pertaining to the transverse electric (TE) and transverse magnetic (TM) modes. In this thesis, calculations of the TM mode are performed, where only the E_x, E_y, D_x, D_y, and H_z fields are present and are governed by the equations

$$\mu_o \frac{\partial H_z}{\partial t} = \frac{\partial E_y}{\partial x} - \frac{\partial E_x}{\partial y} \tag{A.11a}$$

$$\frac{\partial D_x}{\partial t} = \frac{\partial H_z}{\partial y} \tag{A.11b}$$

$$\frac{\partial D_y}{\partial t} = -\frac{\partial H_z}{\partial x} \tag{A.11c}$$

$$\mathbf{D} = \epsilon_o \epsilon \mathbf{E} \tag{A.11d}$$

where the variables have their usual meanings. If ϵ is frequency-independent, the discretization laid out by Taflove[2] is obtained. To more accurately model

[2] A. Taflove, Computational Electrodynamics (Artech House, Boston, 1995).

metallic materials, an auxiliary equation for $\mathbf{D}$ is defined via the Drude model

$$\mathbf{D} = \epsilon_o \mathbf{E} + \frac{\epsilon_o \omega_p^2}{i\omega\nu - \omega^2} \tag{A.12}$$

where ω_p and ν are the plasma and damping frequencies, respectively. To cast Equation (A.12) into a form that can be discretized, its inverse Fourier transform is taken yielding

$$\nu \frac{\partial \mathbf{D}}{\partial t} + \frac{\partial^2 \mathbf{D}}{\partial t^2} = \omega_p^2 \epsilon_o \mathbf{E} + \epsilon_o \nu \frac{\partial \mathbf{E}}{\partial t} + \epsilon_o \frac{\partial^2 \mathbf{E}}{\partial t^2} \tag{A.13}$$

Therefore, Equations (A.13) and (A.11) are discretized and solved numerically in the FDTD approach used in this thesis.

The computer program created to implement the FDTD algorithm implements a window's based graphical user interface (GUI), as shown in Figure A.3, which allows the simulation parameters to be easily changed without the need to re-compile. An explanation of the fields of the GUI are as follows:

x-grid size - The number of pixels composing the simulation along the x-direction.

y-grid size - The number of pixels composing the simulation along the y-direction.

 # time steps - The number of time steps before the simulation ends.

Resolution (nm) - The side length of each pixel, in nanometers.

Snap-shot - The number of time steps to elapse between each time when the full electric field map is saved.

Period (ps) - The period of the desired electromagnetic pulse source, in picoseconds.

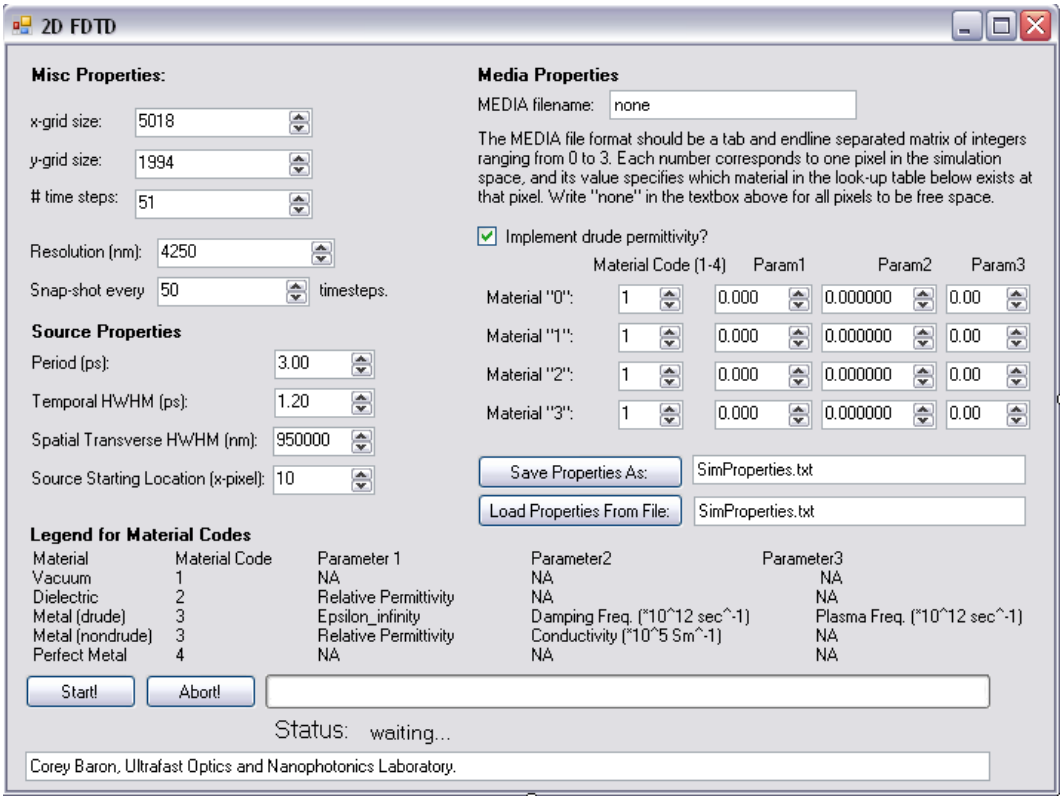

Figure A.3: Screen shot of the GUI for a 2D FDTD program.

Temporal HWHM (ps) - The half-width-half-max of the Gaussian envelope applied to the sinusoid of the above period to obtain the electromagnetic pulse, in ps.

Spatial transverse HWHM (nm) - The half-width-half-max of the Gaussian envelope that defines the transverse spatial profile of the source (i.e. since the pulse is sourced along a line, this is equivalent to the spot size.).

Source Starting Location - The x-pixel location where the source is defined along a line. As such, the source propagates in the x-direction.

MEDIA filename - The filename of a text file located in the same directory as the program that defines the material type at each pixel with a number from 0 to 3. For example, for a 3×3 simulation space consisting of a material specified by "1" at the center and surrounded by free space, the text file would look like:

$$\begin{matrix} 0 & 0 & 0 \\ 0 & 1 & 0 \\ 0 & 0 & 0 \end{matrix}$$

Implement drude permittivity - This check box signifies whether a drude permittivity model should be used or not. If not, all parameters are assumed frequency independent.

Material Codes - A number that signifies the type of material the numbers in the MEDIA text file correspond to, as defined in the table at the bottom of the GUI.

Param - The parameters for the material which have meaning dictated by the material code, as defined in the table at the bottom of the GUI.

Save Properties - This button saves all the above mentioned fields into a text file.

Load Properties - This button loads all the above mentioned fields from a text file.

The C++ code used to create the program is shown on the following pages. The portion of code related to the creation of the GUI is not included since it does not contribute to the FDTD calculations.

```
////////////////////////////////////////////////////////////
// 2D FDTD Simulations

// Corey Baron
// Ultrafast Optics and Nanophotonics Laboratory
// Electrical and Computer Engineering
// University of Alberta

// Selection from Form1.h:
/* This header file contains the main code and is called from
the main program. Shown is the portion that deals with the
calculations, which call functions from the header file
FDTD_2D.h. The code used to create a windows based GUI is not
included. Mur boundary conditions are implemented, and the
source is created using a total field/scattered field approach.
Finally, the Drude model is implemented to enable accurate
modeling of metallic materials.*/
////////////////////////////////////////////////////////////
{
// Load basic parameters from GUI ****************************
Cmesh::setgrid(int(numericUpDown1->Value),
  int(numericUpDown2->Value));
  // setgrid (xgrid size, ygrid size)
Cmesh::setstepsizes(int(numericUpDown4->Value),
  1/sqrt(double(2)));
  // setstepsizes(resolution [nm],c*deltaT/deltaxyz)
Cmesh::setsourcestart(int(numericUpDown25->Value));
```

```
  // setsourcestart(x-location to start source (in pixels))
Cprint::setSnapshotInterval(int(numericUpDown5->Value));
  // Record data every () timesteps.

// Create and allocate memory for the fields ******************
Cfield * pfieldEx = new Cxyfield;
Cfield * pfieldEy = new Cxyfield;
Cfield * pfieldHz = new Czfield;
Cfield * pfieldDx = new Cxyfield;
Cfield * pfieldDy = new Cxyfield;

// Create a source ****************************************
Csource * psource = new Csource;
psource->setsourceparams(double(numericUpDown6->Value),
  double(numericUpDown7->Value),double(numericUpDown8->Value));
  // setsourceparams(period in ps, HWHM in ps, transverse
     spatial HWHM in nm)

Cmedia * pmedia = new Cmedia(); // Free space media
int endsourcetime;
if (int(numericUpDown3->Value) < (2*(psource->ENDt)+1+
(Cmesh::Tkeep)-1)) {
  endsourcetime = int(numericUpDown3->Value)+(Cmesh::Tkeep)-1;
}
else {
  endsourcetime = (2*(psource->ENDt)+1+(Cmesh::Tkeep)-1);
}
```

```
// Create source data
for (int n=(Cmesh::Tkeep-1); n<endsourcetime; n++) {
  pfieldEx->TEmaxwell_nondrude(n, pfieldEx->pfcomponent,
    pfieldEy->pfcomponent,pfieldHz->pfcomponent,pmedia,psource);
  psource->savesourcedata(pfieldEy->pfcomponent,
    pfieldHz->pfcomponent,n);

  // Report percent complete
  int percentComplete = int((double(n)/endsourcetime*100));
  worker->ReportProgress(percentComplete,"building source...");

  // Check for cancellation
  if ( worker->CancellationPending ) {
  e->Cancel = true;
  return 1;
  }
}

// Reset the field data to zero
pfieldEx->resetfields(pfieldEx->pfcomponent,
  pfieldEy->pfcomponent,pfieldHz->pfcomponent);

// Load media information ************************************
/* Load file containing material locations, with 0 representing
   free space and 1, 2, ... identified in order on the
   following lines.*/
```

```
String^ TempString = textBox9->Text;
char* pstr = (char*)System::Runtime::InteropServices::Marshal::
  StringToHGlobalAnsi(TempString).ToPointer();

if (strcmp(pstr,"none")!=0) {pmedia->loadmediafile(pstr);}

// Set material parameters for material 1
if (numericUpDown9->Value == 2) {
  pmedia->add_dielectric(1,double(numericUpDown13->Value));}
else if (numericUpDown9->Value == 3) {
  pmedia->add_metal(1,double(numericUpDown13->Value),
   double(numericUpDown17->Value),
   double(numericUpDown21->Value));}
else if(numericUpDown9->Value == 4){
  pmedia->addperfectmetal(1);}

// Set material parameters for material 2
if (numericUpDown10->Value == 2) {
  pmedia->add_dielectric(2,double(numericUpDown14->Value));}
else if (numericUpDown10->Value == 3) {
  pmedia->add_metal(2,double(numericUpDown14->Value),
   double(numericUpDown18->Value),
   double(numericUpDown22->Value));}
else if(numericUpDown10->Value == 4){
  pmedia->addperfectmetal(2);}
```

```
// Set material parameters for material 3
if (numericUpDown11->Value == 2) {
  pmedia->add_dielectric(3,double(numericUpDown15->Value));}
else if (numericUpDown11->Value == 3) {
  pmedia->add_metal(3,double(numericUpDown15->Value),
   double(numericUpDown19->Value),
   double(numericUpDown23->Value));}
else if (numericUpDown11->Value == 4) {
  pmedia->addperfectmetal(3);}

// Set material parameters for material 4
if (numericUpDown12->Value == 2) {
  pmedia->add_dielectric(4,double(numericUpDown16->Value));}
else if (numericUpDown12->Value == 3) {
  pmedia->add_metal(4,double(numericUpDown16->Value),
   double(numericUpDown20->Value),
   double(numericUpDown24->Value));}
else if (numericUpDown12->Value == 4) {
  pmedia->addperfectmetal(4);}



// Run the simulation ****************************************

// Make the source a total/scattered source:
psource->setsourcetype(1);

// Iterate through time:
```

```
{for (int n=(Cmesh::Tkeep-1); n<int(numericUpDown3->Value); n++) {
  if ( checkBox1->Checked ) {
   pfieldEx->TEmaxwell(n, pfieldEx->pfcomponent,
    pfieldEy->pfcomponent,pfieldDx->pfcomponent,
    pfieldDy->pfcomponent,pfieldHz->pfcomponent,pmedia,psource);
  }
  else {
   pfieldEx->TEmaxwell_nondrude(n, pfieldEx->pfcomponent,
   pfieldEy->pfcomponent,pfieldHz->pfcomponent,pmedia,psource);
  }
  pfieldEx->snapshot(n,pfieldEx->pfcomponent,
   pfieldEy->pfcomponent,pfieldHz->pfcomponent);

  // Report percent complete
  int percentComplete =
    int((double(n)/double(numericUpDown3->Value)*100));
  worker->ReportProgress( percentComplete, "calculating..." );

  // Check for cancellation
  if ( worker->CancellationPending ) {
    e->Cancel = true;
    return 1;
  }
}}

// Clean memory
delete pfieldEx;
```

```
delete pfieldEy;

delete pfieldHz;

delete psource;

delete pmedia;

delete pfieldDx;

delete pfieldDy;



return 0;

}
```

```
////////////////////////////////////////////////////////////
// FDTD_2D.h:
/* This header file contains all the relavent class and
function definitions for the simulation. Mur boundary conditions
are implemented, and a drude model is used. These equations are
for the TM polarization. */
////////////////////////////////////////////////////////////

#include "stdafx.h"
using namespace std;

#define PI 3.141592653589793
#define eps 8.85418782
#define lightspeed 2.99792458

/* Cmesh stores the main variables of the simulation and
related fcns.*/
class Cmesh {
public:
  static int xgrid, ygrid, Tkeep, sourcestart;
  static double ts, deltaT, deltaxyz;
  static void setgrid (int a, int b) {
    xgrid = a;
    ygrid = b;
  }
  static void setstepsizes (double a, double b) {
    deltaxyz = a;         // Units in nanometers
```

```
    ts = b;                // ts = wavespeed*deltaT/deltaxyz.
    deltaT = a/300000*b;  // Units in picoseconds
  }
  static void setsourcestart (int a) {sourcestart = a;}
  void updateprogress (int,int);
};
int Cmesh::xgrid = 0, Cmesh::ygrid=0, Cmesh::sourcestart=10;
double Cmesh::ts=0, Cmesh::deltaT=0, Cmesh::deltaxyz=0;
int Cmesh::Tkeep = 3;
// Tkeep is the number of time steps retained in memory.

// Cprint is for functions related to saving a timestep
class Cprint: public Cmesh {
  char filename[128];
public:
  static int Tsnap;
  static void setSnapshotInterval (int a) {Tsnap = a;}
  void snapshot (int n, double *** data1, double *** data2,
   double *** data3) {
    if (n%Tsnap == 0) {
      sprintf_s(filename, 128, "sim2D_%04d.txt", n);
      ofstream datafile (filename, ios::trunc);
      for (int i=0; i<xgrid; i++) {
        for (int j=0; j<ygrid; j++) {
          if ((i == (xgrid-1)) || (j == (ygrid-1))) {
            datafile << data1[i][j][n%Tkeep] << ' ' <<
              data2[i][j][n%Tkeep] << ' ' << '0' << endl;
```

```
          }
          else {
            datafile << data1[i][j][n%Tkeep] << ' ' <<
              data2[i][j][n%Tkeep] << ' ' <<
              data3[i][j][n%Tkeep] << endl;
          }
        }
      }
    datafile.close ();
    }
  }
};
int Cprint::Tsnap = 100000;
// Take a snapshot every Tsnap timesteps.

// Cmedia involves the MEDIA information and related functions
class Cmedia: public Cmesh {
public:
  int ** MEDIA;
  double pCa[4]; double pCb[4]; double pDa[4]; double pDb[4];
  double pRel_eps[4]; double pMu[4]; double pWp[4];
  //double * pCa, * pCb, * pDa, * pDb, * pRel_eps, * pMu, * pWp;
/* Above: pRel_eps is for relative permattivity, pMu and pWp
  are for damping and plasma freq. in drude model, respectively.
  - pMu should always be in units of 1e12 sec^-1
  - pWp should always be in units of 1e12 sec^-1*/
  void loadmediafile(char[]);
```

```
  Cmedia ();
  ~Cmedia () {
    for (int x=0; x<xgrid; x++) {
      delete MEDIA[x];
    }
    delete MEDIA;
  }
/*To follow are functions to add in material properties to Ca,
Cb, etc, parameters. pCa[0], pCb[0], etc are reserved for free
space parameters.*/
  void addperfectmetal (int);
  void add_dielectric (int, double);
  void add_metal (int, double, double, double);
};
Cmedia::Cmedia () {
  MEDIA = new int* [xgrid];
  for (int x=0; x<xgrid; x++) {
    MEDIA[x] = new int [ygrid];
    for (int y=0; y<ygrid; y++) {
      MEDIA[x][y] = 0;
    }
  }

  for (int count = 0; count<4; count++) {
    pCa[count] = 1;
    pCb[count] = ts*(10*lightspeed)*4*PI;
```

```
    pDa[count] = 1;
    pDb[count] = ts/(10*lightspeed)/4/PI;
    pRel_eps[count] = 1;
    pMu[count] = 0;
    pWp[count] = 0;
  }
}

void Cmedia::loadmediafile (char name[]) {
  ifstream mediafile (name);

  if (mediafile.is_open()) {
    for (int i=0; i<xgrid; i++) {
      for (int j=0; j<ygrid; j++) {
        if (! mediafile.eof()) {
          mediafile >> MEDIA[i][j];
        }
      }
    }
    mediafile.close();
  }
}

void Cmedia::addperfectmetal (int indexnumber) {

  pCa[indexnumber-1]      = -1;
  pCb[indexnumber-1]      = 0;
```

```
  pRel_eps[indexnumber-1] = 1.5e308;
  pMu[indexnumber-1]      = 0;
  pWp[indexnumber-1]      = 0;
  pDa[indexnumber-1]      = 1;
  pDb[indexnumber-1]      = ts/(10*lightspeed)/4/PI;
}

void Cmedia::add_dielectric (int indexnumber,
  double relpermittivity) {

  pCa[indexnumber-1]      = 1;
  pCb[indexnumber-1]      = ts/0.0003/eps/relpermittivity;
  pRel_eps[indexnumber-1] = relpermittivity;
  pMu[indexnumber-1]      = 0;
  pWp[indexnumber-1]      = 0;
  pDa[indexnumber-1]      = 1;
  pDb[indexnumber-1]      = ts/(10*lightspeed)/4/PI;
}

void Cmedia::add_metal (int indexnumber, double relpermittivity,
  double mu, double wp) {

  double sigma = mu*1e5;
  pCa[indexnumber-1]      = (1-sigma*deltaT/2/eps/
    relpermittivity)/(1+sigma*deltaT/2/eps/relpermittivity);
  pCb[indexnumber-1]      = ts*(10*lightspeed)*4*PI/
    relpermittivity/(1+sigma*deltaT/2/eps/relpermittivity);
```

```
  pRel_eps[indexnumber-1] = relpermittivity;
  pMu[indexnumber-1]      = mu;
  pWp[indexnumber-1]      = wp;
  pDa[indexnumber-1]      = 1;
  pDb[indexnumber-1]      = ts/(10*lightspeed)/4/PI;
}

// Csource involves functions related to specifying the source.
class Csource: public Cmesh {
  double ** psourcey;
  double ** psourcez;
  double period;
  double HWHMt;
  double HWHMy;
  int ENDs;
  int sourcetype;
  ofstream sourcefile;//Specify an output stream for the source.
public:
  int ENDt;
  void setsourceparams (double, double, double);
  void implementhardsource (double***, int);
  void savesourcedata(double***, double***, int);
  int requestsourcetype() {return sourcetype;}
  void setsourcetype(int a) {sourcetype = a;}
  double requestsourcevalue_y(int, int);
  double requestsourcevalue_z(int, int);
/* requestsourcevalue is called during the iteration through
```

```
time to implement the source.*/


  Csource () {
    sourcetype = 0;
  }
  ~Csource () {}
};
void Csource::setsourceparams(double a, double b, double c) {
  period = a/deltaT;// Convert from time to number of timesteps.
  HWHMt = b;
  HWHMy = c;
  ENDt = int(HWHMt/deltaT*3);
  ENDs = ygrid/2-2;


  psourcey = new double* [(ygrid-1)];
  for (int x=0; x<(ygrid-1); x++) {
    psourcey[x] = new double [(2*ENDt+1)];
  }
  psourcez = new double* [(ygrid-1)];
  {for (int x=0; x<(ygrid-1); x++) {
    psourcez[x] = new double [(2*ENDt+1)];
  }}
}


void Csource::implementhardsource (double*** pEy, int n) {
  //ofstream sourcefile;
  //sourcefile.open ("2Dsource.txt", ios::app);
```

```
  const double HM = sqrt(2* double(log(double(2))));
// Time where half max occurs for a gaussian when sigma is 1

  double Timestep = HM/(HWHMt/deltaT); // Time increment
  double Spacestep = HM/(HWHMy/deltaxyz); // Space increment

  int fixedn = n-(Tkeep-1);
  double t = (fixedn-ENDt-1)*Timestep;
  if (fixedn<(2*ENDt+1)) {
    for (int index=0; index<(ygrid-1); index++) {
      double y = (index-ENDs-1)*Spacestep;
      pEy[sourcestart][index][n%Tkeep] = exp(-pow(y,2)/2)*
        exp(-pow(t,2)/2)*sin(2*PI/period*(fixedn-ENDt-1));
      sourcefile << pEy[sourcestart][index][n%Tkeep] << endl;
// Save the source data to the file
    }
  }
  //sourcefile.close();
}
void Csource::savesourcedata(double*** pEy,double*** pHz,int n){
  // Save the data
  if (n<(2*ENDt+2)) {
    for (int j=0; j<(ygrid-1); j++) {
      psourcey[j][n-(Tkeep-1)] = pEy[sourcestart][j][n%Tkeep];
      psourcez[j][n-(Tkeep-1)] = pHz[sourcestart][j][n%Tkeep];
    }
```

```
  }
}
double Csource::requestsourcevalue_y(int j, int n) {
  double output = 0;
  if (n<(2*ENDt+2)) {
    output = psourcey[j][n];
  }
  return output;
}
double Csource::requestsourcevalue_z(int j, int n) {
  double output = 0;
  if (n<(2*ENDt+2)) {
    output = psourcez[j][n];
  }
  return output;
}

// This class includes functions related to the E and H fields.
class Cfield: public Cprint {
private:
  void MURx(int, int, int, double***);
  void MURy(int, int, int, double***);
public:
  double *** pfcomponent;
  void TEmaxwell (int, double***, double***, double***,
    double***, double***, Cmedia*, Csource*);
  void TEmaxwell_nondrude (int, double***, double***,
```

```
    double***, Cmedia*, Csource*);
  void resetfields (double***, double***, double***);
};

void Cfield::MURx(int i, int j, int n, double *** px) {
  // Boundary Conditions
  /*"i" and "j" in the "if" conditions are chosen to be either
    the first or last number in the loop here so that the
    boundary condition is formulated for only one pass through
    the index not in the "if" condition, and so that the
    elements in the RHS at the same timestep as the LHS are
    already known.*/

  if (j==1) // Condition for y=0
  {
    px[i][0][n%Tkeep] = -px[i][1][(n-2)%Tkeep]
     +(ts-1)/(ts+1)*(px[i][1][n%Tkeep] + px[i][0][(n-2)%Tkeep])
     +2/(ts+1)*(px[i][0][(n-1)%Tkeep] + px[i][1][(n-1)%Tkeep]);
    if (i!=0 && i!=xgrid-2)//Make it second order when possible
    {
      px[i][0][n%Tkeep] += ts*ts/2/(ts+1)*
       (px[i+1][0][(n-1)%Tkeep]
       -2*px[i][0][(n-1)%Tkeep] + px[i-1][0][(n-1)%Tkeep]
       +px[i+1][1][(n-1)%Tkeep] - 2*px[i][1][(n-1)%Tkeep]
       +px[i-1][1][(n-1)%Tkeep]);
    }
  }
```

```
  if (j==ygrid-2) // Condition for y=h
  {
    px[i][ygrid-1][n%Tkeep] = -px[i][ygrid-2][(n-2)%Tkeep]
     +(ts-1)/(ts+1)*(px[i][ygrid-2][n%Tkeep]
     +px[i][ygrid-1][(n-2)%Tkeep])
     +2/(ts+1)*(px[i][ygrid-1][(n-1)%Tkeep]
     +px[i][ygrid-2][(n-1)%Tkeep]);
    if (i!=0 && i!=xgrid-2)//Make it second order when possible
    {
      px[i][ygrid-1][n%Tkeep] += ts*ts/2/(ts+1)
       *(px[i+1][ygrid-1][(n-1)%Tkeep]
       -2*px[i][ygrid-1][(n-1)%Tkeep]
       +px[i-1][ygrid-1][(n-1)%Tkeep]
       +px[i+1][ygrid-2][(n-1)%Tkeep]
       -2*px[i][ygrid-2][(n-1)%Tkeep]
       +px[i-1][ygrid-2][(n-1)%Tkeep]);
}
}
}

void Cfield::MURy(int i, int j, int n, double *** py) {
  // Boundary Conditions
  /*"i" and "j" in the "if" conditions are chosen to be either
    the first or last number in the loop here so that the
    boundary condition is formulated for only one pass through
    the index not in the "if" condition, and so that the
```

```
  elements in the RHS at the same timestep as the LHS are
  already known.*/

if (i==1) // Condition for x=0
{
  py[0][j][n%Tkeep] = -py[1][j][(n-2)%Tkeep]
   +(ts-1)/(ts+1)*(py[1][j][n%Tkeep]+py[0][j][(n-2)%Tkeep])
   +2/(ts+1)*(py[0][j][(n-1)%Tkeep]+py[1][j][(n-1)%Tkeep]);
  if(j!=0 && j!=ygrid-2)
  {
    py[0][j][n%Tkeep] += ts*ts/2/(ts+1)
     *(py[0][j+1][(n-1)%Tkeep]
     -2*py[0][j][(n-1)%Tkeep] + py[0][j-1][(n-1)%Tkeep]
     +py[1][j+1][(n-1)%Tkeep] - 2*py[1][j][(n-1)%Tkeep]
     +py[1][j-1][(n-1)%Tkeep]);
  }
}

if (i==xgrid-2) // Condition for x=h
{
  py[xgrid-1][j][n%Tkeep] = -py[xgrid-2][j][(n-2)%Tkeep]
   +(ts-1)/(ts+1)*(py[xgrid-2][j][n%Tkeep]
   +py[xgrid-1][j][(n-2)%Tkeep])
   +2/(ts+1)*(py[xgrid-1][j][(n-1)%Tkeep]
   +py[xgrid-2][j][(n-1)%Tkeep]);
  if (j!=0 && j!=ygrid-2)
  {
```

```
      py[xgrid-1][j][n%Tkeep] += ts*ts/2/(ts+1)
       *(py[xgrid-1][j+1][(n-1)%Tkeep]
       -2*py[xgrid-1][j][(n-1)%Tkeep]
       +py[xgrid-1][j-1][(n-1)%Tkeep]
       +py[xgrid-2][j+1][(n-1)%Tkeep]
       -2*py[xgrid-2][j][(n-1)%Tkeep]
       +py[xgrid-2][j-1][(n-1)%Tkeep]);
    }
  }
}

void Cfield::TEmaxwell (int n,double*** pEx,double*** pEy,
 double*** pDx,double*** pDy,double*** pHz,Cmedia * pmedia,
 Csource * psource) {
  for (int i=0; i<xgrid-1; i++) {
    for(int j=1; j<ygrid-1; j++) {
      pDx[i][j][n%Tkeep] = pDx[i][j][(n-1)%Tkeep]
       +(ts/double(300000000))*(pHz[i][j][(n-1)%Tkeep]
       -pHz[i][j-1][(n-1)%Tkeep]);

      MURx(i, j, n, pDx);
    }
  }
  {for (int i=1; i<xgrid-1; i++) {
    for(int j=0; j<ygrid-1; j++) {
      if (psource->requestsourcetype()) {
        if ( ((i == sourcestart)&&(n>(Tkeep-1))) ) {
```

```
          pDy[i][j][n%Tkeep] = pDy[i][j][(n-1)%Tkeep]
           +(ts/double(300000000))*(pHz[i-1][j][(n-1)%Tkeep]
           -pHz[i][j][(n-1)%Tkeep]
           +psource->requestsourcevalue_z(j,n-(Tkeep-1)-1));
        }
        else {
          pDy[i][j][n%Tkeep] = pDy[i][j][(n-1)%Tkeep]
           +(ts/double(300000000))*(pHz[i-1][j][(n-1)%Tkeep]
           -pHz[i][j][(n-1)%Tkeep]);
        }
      }
      else {
        pDy[i][j][n%Tkeep] = pDy[i][j][(n-1)%Tkeep]
         +(ts/double(300000000))*(pHz[i-1][j][(n-1)%Tkeep]
         -pHz[i][j][(n-1)%Tkeep]);
      }

      MURy(i, j, n, pDy);
    }
  }}

  {for (int i=0; i<xgrid-1; i++) {
    for(int j=1; j<ygrid-1; j++) {
      pEx[i][j][n%Tkeep] =
        (double(1e12)/eps*(((pmedia->pMu[pmedia->MEDIA[i][j]])
        *deltaT+2)*pDx[i][j][n%Tkeep]
        +(-(pmedia->pMu[pmedia->MEDIA[i][j]])*deltaT+2)
```

```
      *pDx[i][j][(n-2)%Tkeep] - 4*pDx[i][j][(n-1)%Tkeep])
      -(pow(pmedia->pWp[pmedia->MEDIA[i][j]],2)*deltaT*deltaT
      -(pmedia->pMu[pmedia->MEDIA[i][j]])
      *(pmedia->pRel_eps[pmedia->MEDIA[i][j]])*deltaT
      +2*(pmedia->pRel_eps[pmedia->MEDIA[i][j]]))
      *pEx[i][j][(n-2)%Tkeep]
      +4*(pmedia->pRel_eps[pmedia->MEDIA[i][j]])
      *pEx[i][j][(n-1)%Tkeep] )
      /( pow(pmedia->pWp[pmedia->MEDIA[i][j]],2)*deltaT*deltaT
      +(pmedia->pMu[pmedia->MEDIA[i][j]])
      *(pmedia->pRel_eps[pmedia->MEDIA[i][j]])*deltaT
      + 2*(pmedia->pRel_eps[pmedia->MEDIA[i][j]]) );

    MURx(i, j, n, pEx);
  }
}}

{for (int i=1; i<xgrid-1; i++) {
  for(int j=0; j<ygrid-1; j++) {
    pEy[i][j][n%Tkeep] =
      ( double(1e12)/eps*(((pmedia->pMu[pmedia->MEDIA[i][j]])
      *deltaT+2)*pDy[i][j][n%Tkeep]
      +(-(pmedia->pMu[pmedia->MEDIA[i][j]])*deltaT+2)
      *pDy[i][j][(n-2)%Tkeep] - 4*pDy[i][j][(n-1)%Tkeep])
      -(pow(pmedia->pWp[pmedia->MEDIA[i][j]],2)*deltaT*deltaT
      -(pmedia->pMu[pmedia->MEDIA[i][j]])
      *(pmedia->pRel_eps[pmedia->MEDIA[i][j]])*deltaT
```

```
      + 2*(pmedia->pRel_eps[pmedia->MEDIA[i][j]]))
      *pEy[i][j][(n-2)%Tkeep]
      + 4*(pmedia->pRel_eps[pmedia->MEDIA[i][j]])
      *pEy[i][j][(n-1)%Tkeep] )
      /( pow(pmedia->pWp[pmedia->MEDIA[i][j]],2)*deltaT*deltaT
      + (pmedia->pMu[pmedia->MEDIA[i][j]])
      *(pmedia->pRel_eps[pmedia->MEDIA[i][j]])*deltaT
      + 2*(pmedia->pRel_eps[pmedia->MEDIA[i][j]]) );

    MURy(i, j, n, pEy);
  }
}}

if ( !(psource->requestsourcetype()) ) {
  psource->implementhardsource(pEy, n);
}

{for (int i=0; i<xgrid-1; i++) {
  for(int j=0; j<ygrid-1; j++) {
    if (psource->requestsourcetype()) {
      if ((i == sourcestart) ) {
        pHz[i][j][n%Tkeep] =
         pmedia->pDa[pmedia->MEDIA[i][j]]
         *pHz[i][j][(n-1)%Tkeep]
         + pmedia->pDb[pmedia->MEDIA[i][j]]
         *(pEx[i][j+1][n%Tkeep] - pEx[i][j][n%Tkeep]
         + pEy[i][j][n%Tkeep] - pEy[i+1][j][n%Tkeep]
```

```
            +psource->requestsourcevalue_y(j,n-(Tkeep-1)));
          }
          else {
            pHz[i][j][n%Tkeep] =
             pmedia->pDa[pmedia->MEDIA[i][j]]
             *pHz[i][j][(n-1)%Tkeep]
             + pmedia->pDb[pmedia->MEDIA[i][j]]
             *(pEx[i][j+1][n%Tkeep] - pEx[i][j][n%Tkeep]
             + pEy[i][j][n%Tkeep]- pEy[i+1][j][n%Tkeep]);
          }
        }
        else {
          pHz[i][j][n%Tkeep] =
           pmedia->pDa[pmedia->MEDIA[i][j]]*pHz[i][j][(n-1)%Tkeep]
           + pmedia->pDb[pmedia->MEDIA[i][j]]
           *(pEx[i][j+1][n%Tkeep] - pEx[i][j][n%Tkeep]
           + pEy[i][j][n%Tkeep]- pEy[i+1][j][n%Tkeep]);
        }
      }
    }}
}
void Cfield::TEmaxwell_nondrude (int n,double*** pEx,
 double*** pEy,double*** pHz,Cmedia * pmedia,
 Csource * psource) {
  for (int i=0; i<xgrid-1; i++) {
    for(int j=1; j<ygrid-1; j++) {
      pEx[i][j][n%Tkeep] = (pmedia->pCa[pmedia->MEDIA[i][j]])
```

```
      *pEx[i][j][(n-1)%Tkeep]
      +(pmedia->pCb[pmedia->MEDIA[i][j]])
      *(pHz[i][j][(n-1)%Tkeep]- pHz[i][j-1][(n-1)%Tkeep]);

      MURx(i, j, n, pEx);
    }
  }
  {for (int i=1; i<xgrid-1; i++) {
    for(int j=0; j<ygrid-1; j++) {
      if (psource->requestsourcetype()) {
        if ( ((i == sourcestart)&&(n>(Tkeep-1))) ) {
          pEy[i][j][n%Tkeep] = pmedia->pCa[pmedia->MEDIA[i][j]]
          *pEy[i][j][(n-1)%Tkeep]
          +pmedia->pCb[pmedia->MEDIA[i][j]]
          *(pHz[i-1][j][(n-1)%Tkeep] - pHz[i][j][(n-1)%Tkeep]
          +psource->requestsourcevalue_z(j,n-(Tkeep-1)-1));
        }
        else {
          pEy[i][j][n%Tkeep] =
          pmedia->pCa[pmedia->MEDIA[i][j]]
          *pEy[i][j][(n-1)%Tkeep]
          +pmedia->pCb[pmedia->MEDIA[i][j]]
          *(pHz[i-1][j][(n-1)%Tkeep] - pHz[i][j][(n-1)%Tkeep]);
        }
      }
      else {
        pEy[i][j][n%Tkeep] = pmedia->pCa[pmedia->MEDIA[i][j]]
```

```
        *pEy[i][j][(n-1)%Tkeep]
        + pmedia->pCb[pmedia->MEDIA[i][j]]
        *(pHz[i-1][j][(n-1)%Tkeep]
        - pHz[i][j][(n-1)%Tkeep]);
      }

      MURy(i, j, n, pEy);
    }
  }}

  if ( !(psource->requestsourcetype()) ) {
    psource->implementhardsource(pEy, n);
  }

  {for (int i=0; i<xgrid-1; i++) {
    for(int j=0; j<ygrid-1; j++) {
      if (psource->requestsourcetype()) {
        if ((i == sourcestart) ) {
          pHz[i][j][n%Tkeep] =
          pmedia->pDa[pmedia->MEDIA[i][j]]
          *pHz[i][j][(n-1)%Tkeep]
          + pmedia->pDb[pmedia->MEDIA[i][j]]
          *(pEx[i][j+1][n%Tkeep] - pEx[i][j][n%Tkeep]
          + pEy[i][j][n%Tkeep] - pEy[i+1][j][n%Tkeep]
          +psource->requestsourcevalue_y(j,n-(Tkeep-1)));
        }
        else {
```

```
          pHz[i][j][n%Tkeep] =
          pmedia->pDa[pmedia->MEDIA[i][j]]
          *pHz[i][j][(n-1)%Tkeep]
          + pmedia->pDb[pmedia->MEDIA[i][j]]
          *(pEx[i][j+1][n%Tkeep] - pEx[i][j][n%Tkeep]
          + pEy[i][j][n%Tkeep] - pEy[i+1][j][n%Tkeep]);
        }
      }
      else {
        pHz[i][j][n%Tkeep] = pmedia->pDa[pmedia->MEDIA[i][j]]
        *pHz[i][j][(n-1)%Tkeep]
        + pmedia->pDb[pmedia->MEDIA[i][j]]
        *(pEx[i][j+1][n%Tkeep]-pEx[i][j][n%Tkeep]
        +pEy[i][j][n%Tkeep]- pEy[i+1][j][n%Tkeep]);
      }
    }
  }}
}
void Cfield::resetfields(double*** pEx,double*** pEy,
 double*** pHz) {
  for (int i=0; i<xgrid; i++) {
    for (int j=0; j<ygrid; j++) {
      for (int k=0; k<Tkeep; k++) {
        pEx[i][j][k] = 0;
        pEy[i][j][k] = 0;
        pHz[i][j][k] = 0;
      }
```

```
    }
  }
}

class Cxyfield: public Cfield {
public:
  Cxyfield () {
    pfcomponent = new double** [xgrid];
    for (int x=0; x<xgrid; x++) {
      pfcomponent[x] = new double* [ygrid];
      for (int y=0; y<ygrid; y++) {
        pfcomponent[x][y] = new double [Tkeep];
        for (int z = 0; z<Tkeep; z++) {
          pfcomponent[x][y][z] = 0;
        }
      }
    }
  }
  ~Cxyfield () {
    for (int x=0; x<xgrid; x++) {
      for (int y=0; y<ygrid; y++) {
        delete[] pfcomponent[x][y];
      }
      delete[] pfcomponent[x];
    }
    delete[] pfcomponent;
  }
```

```
};


class Czfield: public Cfield {
public:
  Czfield () {
    pfcomponent = new double** [xgrid];
    for (int x=0; x<xgrid; x++) {
      pfcomponent[x] = new double* [ygrid];
      for (int y=0; y<ygrid; y++) {
        pfcomponent[x][y] = new double [Tkeep];
        for (int z = 0; z<Tkeep; z++) {
          pfcomponent[x][y][z] = 0;
        }
      }
    }
  }
  ~Czfield () {
    for (int x=0; x<xgrid; x++) {
      for (int y=0; y<ygrid; y++) {
        delete[] pfcomponent[x][y];
      }
      delete[] pfcomponent[x];
    }
    delete[] pfcomponent;
  }
};
```